UNIVERSITY OF CALIFORNIA SAN DIEGO

# Numerical and analytical investigations of non-isothermal fluids

A dissertation submitted in partial satisfaction of the
requirements for the degree
Doctor of Philosophy

in

Engineering Sciences (Mechanical Engineering)

by

Prabakaran Rajamanickam

Committee in charge:

Professor Antonio L. Sánchez, Chair
Professor Forman A. Williams, Co-Chair
Professor Pao C. Chau
Professor Stefan G. Llewellyn Smith
Professor Kalyanasundaram Seshadri

2019

The dissertation of Prabakaran Rajamanickam is approved, and it is acceptable in quality and form for publication on microfilm and electronically:

_____

_____

_____

_____
Co-Chair

_____
Chair

University of California San Diego

2019

TABLE OF CONTENTS

LIST OF FIGURES

LIST OF TABLES

ACKNOWLEDGEMENTS

The author wishes special thanks to Professors Antonio L. Sánchez and Forman A. Williams for suggesting the problems encountered in this dissertation and their invaluable help and numerous discussions throughout this work, from both much inspiration has been derived; to Adam D. Weiss for many fruitful discussions and his friendship.

Chapter 1, in part, has been published in *Combustion Theory and Modelling*, "On the two-reactant one-step activation-energy asymptotics for steady, adiabatic, planar flames with Lewis numbers of unity", by P. Rajamanickam (2018) **22**, 913-920. The dissertation author is the primary investigator in this publication.

Chapter 2, in part, has been published in *Proceedings of the Combustion Institute*, "Influences of stoichiometry on steadily propagating triple flames in counterflows", by P. Rajamanickam, W. Coenen, A. L. Sánchez and F. A. Williams (2019) **37**, 1971-1977. The dissertation author is the primary investigator in this publication.

Chapter 3 is in preparation for publication in *Combustion and Flame*, ""Near-limit $H_2$-$O_2$-$N_2$ combustion in nonpremixed counterflow mixing layers", by J. Carpio, P. Rajamanickam, A. L. Sánchez, P. D. Ronney, F. A. Williams. The dissertation author is the primary investigator in this publication.

Chapter 4, in part, has been published in *Journal of Propulsion and Power*, "Thermal explosion characteristics of a gelled hypergolic propellants", by P. Rajamanickam. The dissertation author is the primary investigator in this publication.

Chapter 5, in part, has been published in *International Journal of Heat and Mass Transfer*, "Non-Boussinesq stability analysis of natural-convection gaseous flow in inclined hot plates", by P. Rajamanickam, W. Coenen and A. L. Sánchez (2017) **109**, 914-917. The dissertation author is the primary investigator in this publication.

## VITA

| | |
|---|---|
| 2012 | B. E. in Mechanical Engineering, PSG College of Technology, Coimbatore |
| 2017 | M. S. in Engineering Sciences (Mechanical Engineering), University of California, San Diego |
| 2019 | Ph. D. in Engineering Sciences (Mechanical Engineering), University of California, San Diego |

## PUBLICATIONS

**P. Rajamanickam**, W. Coenen, A. L. Sánchez, "Non-Boussinesq stability analysis of natural-convection gaseous flow on inclined hot plates", *International Journal of Heat and Mass Transfer*, 109, 914-917, 2017.

**P. Rajamanickam**, "On the two-reactant one-step activation-energy asymptotics for steady, adiabatic, planar flames with Lewis numbers of unity", *Combustion Theory and Modelling*, 22(5), 913-920, 2018.

**P. Rajamanickam**, W. Coenen, A. L. Sánchez, F. A. Williams, "Influences of stoichiometry on steadily propagating triple flames in counterflows", *Proceedings of the Combustion Institute*, 37(2), 1971-1977, 2019.

W. Coenen, **P. Rajamanickam**, A. D. Weiss, A. L. Sánchez, F. A. Williams, "Swirling flow induced by jets and plumes", *Acta Mechanica*, 230(6), 2221-2231, 2019.

**P. Rajamanickam**, A. D. Weiss, "A note on viscous flow induced by half-line sources bounded by conical surfaces", *The Quarterly Journal of Mechanics and Applied Mathematics*, (in press), 2020.

**P. Rajamanickam**, "Thermal explosion characteristics of a gelled hypergolic propellants", *Journal of Propulsion and Power*, (in press), 2020.

A. D. Weiss, **P. Rajamanickam**, W. Coenen, A. L. Sánchez, F. A. Williams, "A model for the boundary layer surrounding fire whirls", *Journal of Fluid Mechanics*, (submitted).

J. Carpio, **P. Rajamanickam**, A. L. Sánchez, P. D. Ronney, F. A. Williams, "Near-limit $H_2$-$O_2$-$N_2$ combustion in nonpremixed counterflow mixing layers", *Combustion and Flame*, (in preparation).

ABSTRACT OF THE DISSERTATION

**Numerical and analytical investigations of non-isothermal fluids**

by

Prabakaran Rajamanickam

Doctor of Philosophy in Engineering Sciences (Mechanical Engineering)

University of California San Diego, 2019

Professor Antonio L. Sánchez, Chair
Professor Forman A. Williams, Co-Chair

Theoretical and numerical techniques are used to investigate three different problems involving non-isothermal fluid flow.

The first part of the dissertation investigates flame dynamics in a strained mixing layer established between two-dimensional counterflowing streams of fuel and oxidizer. When a one-step Arrhenius chemistry model is employed for the chemistry description, the numerical computations for small values of the stoichiometric mixture fraction yield a C-shaped premixed front with a trailing diffusion flame attached to one of its ends, a structure that is markedly different to the tri-brachial structure found in previous studies. Analytic predictions from the G

equation are found to agree well with the numerical results. An explanation for these unexpected shapes is obtained by analyzing the variation with dilution of the burning velocity of planar premixed flames. Detailed-chemistry results are presented next for $H_2$-$O_2$-$N_2$ systems with high degrees of $N_2$ dilution, such that the resulting flame temperature lies close to the crossover value. Under these near-critical conditions, the flame dynamics is found to be strongly dependent on the initial conditions. A bifurcation diagram is presented in the stoichiometric mixture-fraction vs. strain-rate plane that identifies six different combustion regimes involving four different flame types, namely, one-dimensional diffusion flames, propagating/retreating edge flames, broken flame tubes, and isolated flame tubes.

Spherically symmetric heterogeneous fuel-oxidizer system is investigated next as an ignition model for hypergolic gelled propellants. Depending on the conditions, the fuel-oxidizer system may approach an explosive mode or it may settle into a steady-state mode. The critical condition defining the transition between these two states is determined analytically and the ignition time for the explosive mode is approximated by solving an integral equation for the interface temperature, employing activation-energy asymptotics.

A non-Boussinesq stability analysis of natural-convection boundary-layer flows over hot inclined surfaces is presented in the last part of the dissertation. Depending on the inclination angle, the disturbances are seen to evolve into either streamwise vortices or spanwise traveling waves. The critical inclination angle at which transition between the two instability modes occurs is calculated as a function of wall-to-ambient temperature ratio. For sufficiently large values of this ratio, wave modes are found to be always predominant, regardless of the inclination angle.

# Part I

# Unstrained and strained flame dynamics

# Brief overview

A brief overview of each chapter of Part I is given in the following three paragraphs, respectively.

Aspects of predictions of activation-energy asymptotics concerning the dependence of the burning velocity on the equivalence ratio are examined in chapter 1 through both asymptotic analyses and numerical computation. In typical hydrocarbon-air flames, the burning velocity achieves its maximum value for fuel-rich mixture, the cause being generally attributed to the effects of detailed chemical kinetics and unequal diffusivities of the reactants. The present results demonstrate the possibility of this attribute of the burning velocity occurring even when these two effects are absent. This is accomplished by parametrically studying the burning-velocity formula valid for all equivalence ratios under the conditions specified in the title of this article, with special attention paid to implications for hydrocarbon-air flames.

Most studies of triple flames in counterflowing streams of fuel and oxidizer have been focused on the symmetric problem in which the stoichiometric mixture fraction is $1/2$. There then exist lean and rich premixed flames of roughly equal strengths, with a diffusion flame trailing behind from the stoichiometric point at which they meet. In the majority of realistic situations, however, the stoichiometric mixture fraction departs appreciably from unity, typically being quite small. With the objective of clarifying the influences of effects of stoichiometry, attention is focused on one of the simplest possible models, including what has commonly been called the thermo-diffusive approximation, addressed in chapter 2 mainly by numerical integration. When the stoichiometric mixture fraction departs appreciably from $1/2$, one of the premixed wings is found to be dominant to such an extent that the diffusion flame and the other premixed flame are very weak by comparison. These curved, partially premixed flames, whose characteristics are explored in chapter 2, are expected to be relevant to flames in realistic counterflow triple-flame configurations. In addition, a simple kinematic balance is shown to predict the shape of the front

and the propagation velocity reasonably well in the limit of low stretch and low curvature.

Numerical computations employing detailed chemistry are used in chapter 3 to characterize the different combustion modes emerging in mixing layers separating nitrogen-diluted counterflowing planar streams of hydrogen and oxygen. Attention is focused on high degrees of dilution, resulting in near-limit flames, with peak temperatures close to the crossover temperature. A bifurcation diagram is presented in a plane, having the stoichiometric mixture fraction and normalized strain rate as coordinates, that identifies six different combustion regimes involving four different flame types, namely, diffusion-flame sheets, advancing and retreating edge flames, multiple flame tubes, and single isolated flame tubes. Multiple-tube flame configurations vary from small, round, widely separated flame strings at high strain rates to wide, flat, densely packed flame strips, with narrow flame-free gaps between them, at lower strain rates, and they are steady and stable in various arrays over a continuum of tube-separation distances. The observed flame behavior exhibits hysteresis in a certain range of parameters, with the structure that is established depending on the ignition mechanism, as it also does at high strain rates, and a continuum of different stable steady-state flame configurations exists, each accessed from a different initial condition.

# Chapter 1

# Activation-energy asymptotics for planar premixed flames

## 1.1 Introduction

Concepts of activation-energy asymptotics (AEA) have played important roles in the description of premixed laminar flame structures ever since the work of Zel'dovich and Frank-Kamenetskii [1]. Resulting asymptotic formulas for burning velocities of two-reactant flames [2], when plotted as functions of the equivalence ratio, possess attributes that depend on how individual factors in the formulas are varied. Study of the dependence of the burning velocity on the equivalence ratio was initiated by Clarke [3], for reactants with unity Lewis number. While he anticipated that the burning velocity would reach a maximum for fuel-rich mixtures depending on how the mixture is formed, he did not quantify that idea. It was Sen and Ludford, who carried out the analysis, in a series of publications [4–8], emphasizing mainly Lewis-number effects and product-dissociation effects, addressing an open question of the late 1970's, namely the extent to which the observed fuel-rich location of the burning-velocity maximum could be attributed to Lewis-number effects rather than to the detailed chemistry. They specifically identified two of

the various conditions (to be mentioned later) under which the equivalence ratio can be varied, a constant fraction of inert (case I) and a constant ratio of inert fraction to oxidizer fraction (case II). Most of the experimental burning-velocity measurements that have been reported are for fuel-air mixtures, which correspond to their case II, and which is the condition to be discussed here.

The works of Sen and Ludford emphasized near-stoichiometric conditions, based on the assumption that the peak burning-velocity occurs for slightly fuel-rich conditions, as has been summarized by Bechtold and Matalon [9]. Although this analysis was completed nearly forty years ago, there has been no more recent discussion of their considerations for equivalence ratios not close to unity. It is the purpose of this study to address all equivalence ratios, without making any reference to Lewis-number effects. For the example of methane-air mixtures, application of leading-order AEA and numerical integration will be shown in this article to demonstrate that, the rich shift predicted by AEA and numerics is large, beyond the range of accuracy of near-stoichiometric AEA, lying instead in the range of the analysis of Clarke, as extended by Mitani [10] and Rogg [11]. Prospects for accurate use of AEA for other hydrocarbon-air mixtures also will be considered.

## 1.2 Formulation and asymptotic solution

Although complicating factors such as variable properties and Stefan-Maxwell transport have been included in previous work [12], the points to be addressed here may be based on simpler formulations [10, 11, 13], for one-step Arrhenius chemistry with arbitrary reaction orders $m$ and $n$ with respect to the fuel and oxidizer, respectively. In addition, all Lewis numbers will be set equal to unity, thereby purposely ruling out influences of differential diffusion. Most of the discussion will pertian to $m = n = 1$, the values assumed in the work of Clarke [3] and of Sen and Ludford [4]. The gas density $\rho$ and the thermal diffusivity $D_T$ are both constant in the formulation and in the numerical integrations to be reported.

Under the given approximations, a temperature-explicit formulation applies. With $T_o$ and $T_\infty$ denoting the fresh-mixture and burnt-gas temperatures, the normalized dependent variable for the temperature $T$ is $\tau = (T - T_o)/(T_\infty - T_o)$, and the parameter $\alpha = (T_\infty - T_o)/T_\infty$ measures the heat release. In terms of the laminar burning velocity $S_L$, the characteristic length $D_T/S_L$ is introduced to define the nondimensional spatial coordinate $x$. The symbol $\phi$ will be employed for the conventional fuel-air equivalence ratio, so that $0 < \phi < \infty$. In terms of the activation energy $E$ and the universal gas constant $R$, the Zel'dovich number, $\beta = \alpha E/(RT_\infty)$, is the large parameter of expansion. Given an appropriate characteristic reciprocal-time pre-factor constant for the reaction rate, $B$, the burning-rate eigenvalue is $\Lambda = (BD_T/S_L^2)\mathrm{e}^{-E/(RT_\infty)}$. The differential equation to be solved, for instance for a lean mixture, then becomes

$$\frac{\mathrm{d}^2\tau}{\mathrm{d}x^2} = \frac{\mathrm{d}\tau}{\mathrm{d}x} - \Lambda(1-\tau)^m(1-\phi\tau)^n \exp\left[-\frac{\beta(1-\tau)}{1-\alpha(1-\tau)}\right], \tag{1.1}$$

subject to $\tau$ approaching zero as $x$ approaches $-\infty$ and $\tau$ approaching unity as $x$ approaches $+\infty$.

As is well known, in the limit of $\beta$ approaching infinity, there is an upstream convective-diffusive zone in which $\tau$ is proportional to $\mathrm{e}^x$, followed by an inner zone, with thickness of order $x/\beta$, that is reactive-diffusive at leading order and within which the order-unity dependent variable $y = \beta(1-\tau)$ must match the convective-diffusive solution as that variable approaches infinity. The problem is independent of $\alpha$ at leading order, when it is of order unity or smaller, and the equation depends on the scaling of $\phi$, the most general choice for fuel-lean mixtures being that $\gamma_l = \beta(1-\phi)/\phi$ is a parameter of order unity. With this selection, matching at leading order produces

$$\frac{\beta^{m+n+1}}{2\Lambda\phi^n} = \int_0^\infty t^m(t+\gamma_l)^n \mathrm{e}^{-t}\mathrm{d}t \equiv \mathcal{G}(m,n,\gamma_l). \tag{1.2}$$

The function $\mathcal{G}(m,n,\gamma_l)$ is a confluent hypergeometric function, expressible in the form $\mathcal{G}(m,n,\gamma_l) = \gamma_l^{m+n+1}\Gamma(m+1)U(m+1,m+n+2,\gamma_l)$, where $\Gamma$ is the gamma function and $U$ is the Kummer's function of the second kind, and it reduces to $\Gamma(m+n+1)$ at the stoichiometric condition $\gamma_l = 0$,

while approaching $\gamma_l^n \Gamma(m+1)$ as $\gamma_l$ approaches infinity. The corresponding result for fuel-rich mixture turns out to be

$$\frac{\beta^{m+n+1}}{2\Lambda\phi^{1-m}} = \mathscr{G}(n,m,\gamma_r), \tag{1.3}$$

where $\gamma_r = \beta(\phi - 1)$. Although the results seem to reduce to the stoichiometric result when $\gamma_l = \gamma_r = 0$, care is required to infer these results for near-stoichiometric conditions.

## 1.3 Variations with equivalence ratio

Although some one-step empirical correlations, especially, for autoignition times [14], but also occasionally for burning velocities [15], exhibit negative reaction orders for the fuel, for the great majority of fuels, as well as in studies directed towards revealing qualitative attributes of flame propagation, both $m$ and $n$ are positive. Under these usual conditions, $\mathscr{G}$ achieves a minimum value at $\phi = 1$, increasing monotonically in moving away from stoichiometry. The fact that $\mathscr{G}$ usually does not exhibit a maximum value at $\phi = 1$ affords the possibility of predicted burning velocities achieving maximum values at conditions far from stoichiometric. The specific form of the function $S_L(\phi)$ for given values of $m$ and $n$ depends on the variations with $\phi$ that are selected for other parameters, such as $B$ and $T_\infty$. The reciprocal time $B$, for example, is proportional to the product of two factors, one being the initial concentration of the oxidizer raised to the power $n$ and the other the initial concentration of the fuel raised to the power $m-1$; at least one of these two factors must be changed to vary $\phi$. In addition, the variation of $T_\infty$ with $\phi$ depends on the specific set of experiments to be addressed.

The adiabatic flame temperature $T_\infty$ may be held fixed as $\phi$ is changed - a selection often made in counterflow flame experiments to remove the large effect of temperature variations on the chemical kinetics [16]. When that is done, the Arrhenius factor does not influence the function $S_L(\phi)$, but achieving a constant value of $T_\infty$ necessitates decreasing the dilution of the mixture in moving away from the stoichiometric condition $\phi = 1$, for typical experiments in which the initial

temperature $T_o$ remains constant. There often is interest in varying the stoichiometry at fixed dilution, in which case the influence of the Arrhenius factor on $S_L$ can be dominant, producing a maximum of the predicted burning velocity very close to $\phi = 1$ when the activation energy $E$ is large. When realistic values of $E$ and of other parameters are employed in the formula, at constant dilution the maximum of $S_L(\phi)$ often occurs away from stoichiometric conditions, which can be advantageous in fitting burning-velocity data for real flames that achieve maxima at fuel-rich conditions.

Graphical presentations of computed laminar burning velocities serve to illustrate these results and to test the accuracies of the predictions of the asymptotic formulas. This is done here for a situation in which $\phi$ is varied by isothermal mixing of a fuel stream with an oxidizer stream, both streams being at the same temperature $T_o$. The variation of the adiabatic flame temperature $T_\infty$ with $\phi$ is chosen to correspond to a constant heat capacity for the mixture, thereby determining the variation of $\beta$ with the equivalence ratio. If the mixture is formed by combining diluted fuel and oxidizer streams, then the predicted variations of burning velocities depend on a stoichiometry parameter, the ratio of the mass of the oxygen required to burn the fuel in the fuel stream completely to the actual mass of the oxygen in the oxidizer stream, which will be denoted by $S$, resulting in,

$$\frac{T_\infty}{T_{\infty,s}} = 1 - \alpha_s + \alpha_s \frac{S+1}{S+\phi} \begin{cases} \phi, & \text{for } \phi \leq 1 \\ 1, & \text{for } \phi \geq 1, \end{cases} \tag{1.4}$$

where the subscript $s$ identifies values evaluated at the stoichiometric condition, $\phi = 1$. For case I of Sen and Ludford [4], $S = \nu$, the stoichiometric mass ratio and for case II, $S = \nu(1+b)$, where $b$ is the inert to oxidizer mass ratio; the curves to be shown here correspond to case II. The stoichiometry parameter $S$ defined here will become the natural choice for non-uniform reactant mixtures, such as in premixed wings of the triple flames, upon which the study is motivated. Through its relationship to the adiabatic flame temperature $T_\infty(\phi)$, the variation of the Zel'dovich

number and the heat-release parameter can be found from,

$$\frac{\beta}{\beta_s} = \left(\frac{T_{\infty,s}}{T_\infty}\right)^2 \begin{cases} \phi(S+1)/(S+\phi), & \text{for } \phi \leq 1 \\ (S+1)/(S+\phi), & \text{for } \phi \geq 1, \end{cases} \tag{1.5}$$

and

$$\frac{\alpha}{\alpha_s} = \frac{\beta}{\beta_s}\frac{T_\infty}{T_{\infty,s}}, \tag{1.6}$$

at constant $E$. The reciprocal-time pre-exponential factor defined before becomes

$$\frac{B}{B_s} = \phi^{m-1}\left(\frac{S+1}{S+\phi}\right)^{m+n-1}. \tag{1.7}$$

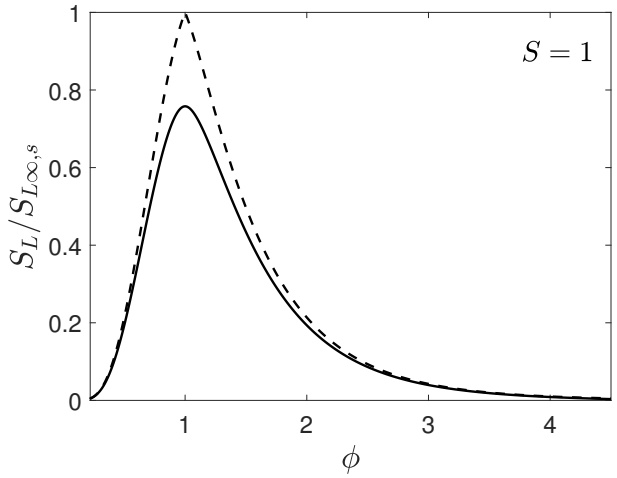


**Figure 1.1**: Numerical (solid curve) and asymptotic (dashed curve) result for $S = 1$ with $\beta_s = 8$, $\alpha_s = 0.85$ and $(m,n) = (1,1)$.

To increase the generality of the results by avoiding the necessity of selecting particular values for other properties, such as $\rho$ and $D_T$, the figures will show the ratio of the calculated burning velocity to the value of the burning velocity obtained from the (leading-order) asymptotic formula at the stoichiometric point ($\phi = 1$), plotted in terms of the equivalence ratio $\phi$. In this

scale, the leading-order asymptotic expression for the burning velocity is given by

$$\phi \le 1: \ \frac{S_L}{S_{L\infty,s}} = \left\{ \left( \frac{\phi(S+1)}{S+\phi} \right)^{m+n-1} \left( \frac{\beta_s}{\beta} \right)^{m+n+1} \frac{\mathscr{G}(m,n,\gamma_l)}{\Gamma(m+n+1)} \, \mathrm{e}^{\beta_s/\alpha_s - \beta/\alpha} \right\}^{1/2}, \qquad (1.8a)$$

$$\phi \ge 1: \ \frac{S_L}{S_{L\infty,s}} = \left\{ \left( \frac{S+1}{S+\phi} \right)^{m+n-1} \left( \frac{\beta_s}{\beta} \right)^{m+n+1} \frac{\mathscr{G}(n,m,\gamma_r)}{\Gamma(m+n+1)} \, \mathrm{e}^{\beta_s/\alpha_s - \beta/\alpha} \right\}^{1/2}, \qquad (1.8b)$$

where the first term in each of the foregoing expressions raised to the power $m+n-1$ is the ratio of upstream concentration of deficient reactant to its stoichiometric value. In the near-stoichiometric limit, only the last two factors in these expressions vary with $\phi$ at leading order, as noted by Sen and Ludford in their analysis [8]. Farther away from stoichiometric conditions, however, these terms vary at leading order, and there are other relevant variations, such as $B(\phi)$ and $\beta(\phi)$ that need to be taken into account. No previous publications have shown results which do that.

## 1.4 Representative results

Figure 1.1 compares the leading-order asymptotic prediction (dashed curve) with the result of the numerical integration (solid curve), for the representative values $\beta_s = 8$ of the Zel'dovich number of the stoichiometric mixture and $\alpha_s = 0.85$ of the heat-release parameter, in the symmetric case $S = 1$. Since the Zel'dovich number increases in moving away from stoichiometry, this is its minimum value, whence the asymptotic formula should be increasingly accurate as the departure from $\phi = 1$ increases. The figure indicates that expectation to be true and shows that the formula overpredicts the burning-velocity by nearly 30% at stoichiometric conditions. There is a discontinuity in the slope of the AEA curve of the formulas given above at $\phi = 1$ that arises from plotting only the leading-order solution and that can be removed by considering distinguished near-stoichiometric limit where $\phi = 1 + c/\beta^{-1}$ (rich) or $\phi = 1 - c/\beta$

(lean) and $c$ is an order unity constant. The burning velocity

$$\phi \le 1: \ \frac{S_L}{S_{L\infty,s}} = \left\{ \frac{\mathscr{G}(m,n,c)}{\Gamma(m+n+1)} \, \mathrm{e}^{-cS/(S+1)} \right\}^{1/2}, \tag{1.9a}$$

$$\phi \ge 1: \ \frac{S_L}{S_{L\infty,s}} = \left\{ \frac{\mathscr{G}(n,m,c)}{\Gamma(m+n+1)} \, \mathrm{e}^{-c/(S+1)} \right\}^{1/2} \tag{1.9b}$$

then exhibits continuous slope at $\phi = 1$. Since emphasis of this work is on fuel-rich conditions, near-stoichiometric limit will not be discussed further here.

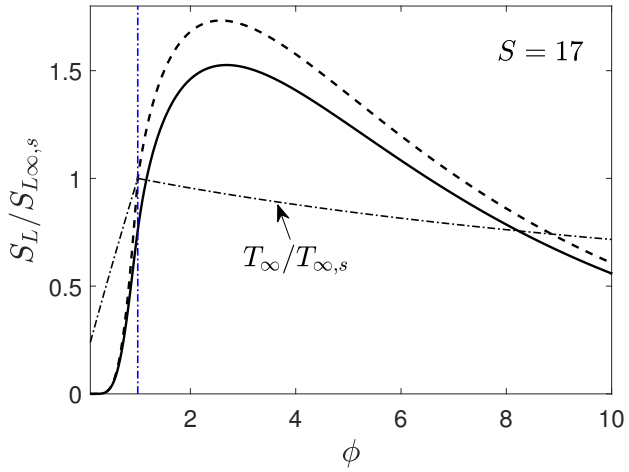


**Figure 1.2**: Numerical (solid curve) and asymptotic (dashed curve) result for $S = 17$ with $\beta_s = 8$, $\alpha_s = 0.85$ and $(m,n) = (1,1)$.

Figure 1.2 shows similar results for $S = 17$, the value applicable when the fuel stream is pure methane and the oxidizer stream is air. The values of $\beta_s$ and $\alpha_s$ have been selected to correspond to reasonable flame temperatures and burning-velocity variations. The results seen here, which are much more representative for the combustion of hydrocarbon fuels (and many others) in air, are quite different from those in Fig. 1.1. The numerical result remains roughly 30% below the asymptotic prediction at the stoichiometric point, $\phi = 1$. This figure illustrates clearly the facts that, not only the result of the numerical integration, but the prediction of the asymptotic formula as well, can give burning velocities that are larger than those for stoichiometric conditions

by a significant amount - the differences being of order unity. For the asymptotic prediction, this behaviour is due entirely to the variation of the function $\mathscr{G}$, the variation of the Arrhenius factor with $T_\infty$ at the fixed value of $E$ opposing this effect but not strong enough to overcome it in rich flames, as may be seen from the $T_\infty$ curve in Fig. 1.2. The dilution does decrease with $\phi$ in this mixing process when $S > 1$, but that decrease is not great enough to produce a decrease in $T_\infty$. This figure also illustrates that, with $\beta_s = 8$ and $m = n = 1$, the equivalence ratio at which the laminar burning velocity is maximum is in close agreement for asymptotic and numerical results, but it exceeds the value that typically would be obtained using the correct detailed chemistry for methane, and it occurs at a value of $\phi$ for which predictions of near-stoichiometric AEA would be highly inaccurate. The predictions shown here are found to differ by approximately 25% from the near-stoichiometric expansion of (8) and (9), a result that is not plotted here. These far-from-stoichiometric results are not addressed in the earlier publications, such as those of Sen and Ludford.

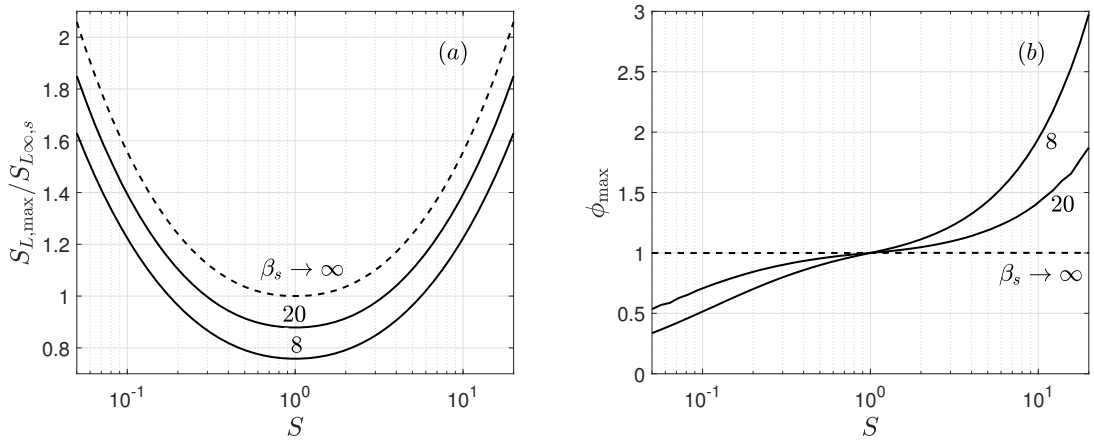


**Figure 1.3**: Maximum burning-velocity and its location as a function of stoichiometric ratio, $S$ with $\alpha_s = 0.85$ and $(m,n) = (1,1)$.

## 1.5 Discussions

A general observation of this study is that influences of the Arrhenius factor decrease compared with influences of $\mathscr{G}$ as departures from $S = 1$ increase. For $m = n$, the magnitudes of departures are the same at the same value of $|\ln S|$, whether $\ln S$ is positive or negative as shown in Fig. 1.3(a), but this symmetry is lost for $m \neq n$. Figure 1.3(b) shows how the equivalence ratio at which the maximum burning velocity is achieved varies increasingly strongly with $S$ as $\beta_s$ decreases. The large increase in the burning velocity in rich flames, above its value at stoichiometric condition, shown in Fig. 1.2, demonstrates how poor this one-step Arrhenius chemistry approximates methane-air flames. In this case the burning-velocity maximum occurs well beyond the range of accuracy of a near-stoichiometric expansion and at much more fuel-rich condition than found experimentally. Although this reaction-rate approximation is poor for methane-air, it may be better for other hydrocarbon-air mixtures, such as ethylene-air, for which the burning-velocity maximum occurs at higher equivalence ratios. For ethylene-air flames, Lewis numbers are close enough to unity for the assumptions of the present formulation to apply, but for flames of propane and higher hydrocarbons, effects of differential diffusions, excluded here, might be expected to become increasingly important, although Fig. 7.7.4, on page 277 of the textbook by Law [17], showing essentially identical burning-velocity curves for higher normal alkanes when plotted against the equivalence ratio, suggests that this effect may not be noticeably large.

## 1.6 Conclusions

The Arrhenius factor is not always dominant in AEA predictions, in that the factors may produce off-stoichiometric burning-rate maxima even without differential diffusion. Formulas of AEA may provide reasonable fits to burning-velocity data for some hydrocarbon-air mixtures, such as ethylene-air systems, but such results are inaccurate for methane-air mixtures. In addition,

reaction orders $m$ and $n$ can be adjusted to fit to burning-velocities of different hydrocarbon-air mixtures, although this is not addressed here.

This chapter, in part, has been published in *Combustion Theory and Modelling*, "On the two-reactant one-step activation-energy asymptotics for steady, adiabatic, planar flames with Lewis numbers of unity", by P. Rajamanickam (2018) **22**, 913-920. The dissertation author is the primary investigator in this publication.

# Bibliography

[1] Y. B. Zel'dovich and D. A. Frank-Kamenetskii. Theory of uniform propagation of flame. *Zhurnal fizicheskoi khimii*, 12(1):100–105, 1938.

[2] F. A. Williams. *Combustion Theory*. 2nd Edn., Benjamin/Cummings., 1985. pp.154-165.

[3] J. F. Clarke. The pre-mixed flame with large activation energy and variable mixture strength: Elementary asymptotic analysis. *Combustion Science and Technology*, 10(5-6):189–194, 1975.

[4] A. K. Sen and G. S. S. Ludford. The near-stoichiometric behavior of combustible mixtures part I: Diffusion of the reactants. *Combustion Science and Technology*, 21(1-2):15–23, 1979.

[5] A. K. Sen and G. S. S. Ludford. The near-stoichiometric behavior of combustible mixtures part II: Dissociation of the products. *Combustion Science and Technology*, 26(5-6):183–191, 1981.

[6] A. K. Sen and G. S. S. Ludford. Effects of mass diffusion on the burning rate of non-dilute mixtures. *Symposium (International) on Combustion*, 18(1):417–424, 1981.

[7] G. S. S. Ludford and A. K. Sen. Burning rate maximum of a plane premixed flame. *Progress in Astronautics and Aeronautics*, 76:427–436, 1981.

[8] A. K. Sen and G. S. S. Ludford. Maximum flame temperature and burning rate of combustible mixtures. *Symposium (International) on Combustion*, 19(1):267–274, 1982.

[9] J. K. Bechtold and M. Matalon. Effects of stoichiometry on stretched premixed flames. *Combustion and Flame*, 119(3):217–232, 1999.

[10] T. Mitani. Propagation velocities of two-reactant flames. *Combustion Science and Technology*, 21(3-4):175–177, 1980.

[11] B. Rogg. On the accuracy of asymptotic flame speed predictions for two-reactant flames. *Combustion Science and Technology*, 45(5-6):317–329, 1986.

[12] H. K. Chelliah and F. A. Williams. Asymptotic analysis of two-reactant flames with variable properties and stefan-maxwell transport. *Combustion Science and Technology*, 51(4-6):129–144, 1987.

[13] F. A. Williams. Overview of asymptotics for methane flames. In *Reduced Kinetic Mechanisms and Asymptotic Approximations for Methane-Air Flames*, pages 68–85. Springer, 1991.

[14] M. B. Colket and L. J. Spadaccini. Scramjet fuels autoignition study. *Journal of Propulsion and Power*, 17(2):315–323, 2001.

[15] C. K. Westbrook and F. L. Dryer. Simplified reaction mechanisms for the oxidation of hydrocarbon fuels in flames. *Combustion Science and Technology*, 27(1-2):31–43, 1981.

[16] R. Seiser, S. Humer, K. Seshadri, and E. Pucher. Experimental investigation of methanol and ethanol flames in nonuniform flows. *Proceedings of the Combustion Institute*, 31(1):1173–1180, 2007.

[17] C. K. Law. *Combustion Physics*. Cambridge university press, 2010.

# Chapter 2

# Influences of stoichiometry on steadily propagating flames in counterflows

## 2.1 Introduction

Triple flames, first identified by Phillips over fifty years ago [1], play a fundamental role in many practical combustion systems. Since they have been observed to move along mixing layers that are strained in laminar and turbulent jet flows, for example, there is interest in investigating their response to the imposed strain rate. The counterflow mixing layer separating two opposed planar jets of fuel and oxidizer, used in previously in theoretical [2, 3] and experimental [4, 5] studies, provides an attractive canonical problem for analyzing these effects. An appreciable literature has now been developed on the subject, as may be seen from a relatively recent publication that contains a thorough review [6].

The present contribution is intended to offer some clarifications concerning such steadily propagating triple flames, by building on a simplification of the formulation of Daou and Liñán [3], who emphasized effects of Lewis numbers by parametrically studying, both numerically and analytically, these triple flames in mixtures with unequal diffusivities. Since underlying influences

of stoichiometry tend to be obscured by varying Lewis numbers, the present considerations are restricted to equi-diffusional systems in which all Lewis numbers are unity. Under that restriction, implications are considered here for systems with stoichiometries that are quite likely to be encountered in practice. The simplifications that will be introduced in the formulation will be identical to those in this previous reference [3], simplifications which also are employed in a number of other publications, thereby facilitating comparisons.

## 2.2 The chemistry and the specific configuration addressed

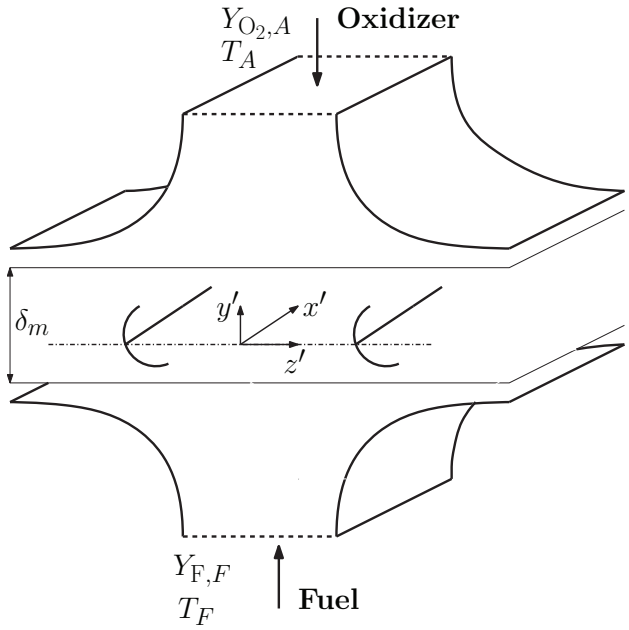


**Figure 2.1**: A Schematic diagram of the counterflow mixing layer considered.

The analysis adopts a one-step irreversible reaction for the chemistry, one unit mass of fuel reacting with $s$ units of mass of oxygen to generate products, according to

$$\text{Fuel} + s\text{O}_2 \rightarrow (1+s)\text{Products} + q, \tag{2.1}$$

where $q$ denotes the amount of energy released in the process per unit mass of fuel consumed.

The number of moles of fuel burned per unit volume per unit time,

$$\omega = B\left(\frac{\rho Y_{\mathrm{F}}}{W_{\mathrm{F}}}\right)\left(\frac{\rho Y_{\mathrm{O}_2}}{W_{\mathrm{O}_2}}\right)\mathrm{e}^{-E_a/RT}, \tag{2.2}$$

is assumed to have a first-order dependence on each reactant concentration and an exponential dependence on the temperature $T$ through an Arrhenius function involving a pre-exponential factor $B$ and an activation energy $E_a$. Here, $\rho$ and $T$ are the density and temperature of the gas mixture, and $R$ is the universal gas constant. Mass fractions and molecular weights of species $i$ are represented by $Y_i$ and $W_i$, respectively. The one-step description with unity reaction orders for fuel and oxidizer considered here has been shown to provide excellent accuracy in computations of methane-air flames under a wide range of conditions [7]. Although for many other fuels empirical fits of detailed chemistry to this one-step approximation usually do not conform to the first-order dependences selected for the reactants [8], this generic choice is made in most previous studies of the present type and therefore is needed here for making comparisons.

Following [3], we investigate triple-flame propagation in a strained mixing layer separating two-dimensional counterflowing streams of fuel and oxidizer, with the front propagating at a constant speed $U$ in the direction perpendicular to the plane of counterflow motion. To render the problem steady, a reference frame moving with the front will be used in the description, as indicated in figure 5.1, with the counterflowing streams approaching from $y' = \pm\infty$ and leaving at $z' = \pm\infty$, and with the front propagating in the negative $x'$ direction. The mixture fraction then will vary from unity in the lower stream to zero in the upper stream, the equivalence ratio correspondingly varying from fuel-rich values greater than unity to fuel-lean values less than unity.

## 2.3 The starting formulation

In the analysis, the thermo-diffusive approximation (i.e. constant density and constant transport properties) is adopted, following the earlier work [2, 3]. The counterflow velocity field then reduces to the familiar stagnation-point solution $(v,w) = (-Ay', Az')$ in terms of the strain rate $A$, which defines, together with the thermal diffusivity $D_T$, the characteristic mixing-layer thickness $\delta_m = (D_T/A)^{1/2}$. Although the velocity varies in the $z'$ direction, the temperature and composition fields are independent of $z'$ in the configuration considered. Studies with variable-density models [9, 10] and other elaborations, such as, propagating flames in counterflow spray mixtures [11] introduce a number of additional interesting phenomena and are available in the literature but are not considered further here because the emphasis is on other aspect of the problem that can be addressed more clearly without introducing these complications.

With the dimensionless variables

$$x = \frac{x'}{\delta_m}, \quad y = \frac{y'}{\delta_m}, \quad \hat{Y}_{\mathrm{F}} = \frac{Y_{\mathrm{F}}}{Y_{\mathrm{F},F}}, \quad \hat{Y}_{\mathrm{O}} = \frac{Y_{\mathrm{O}_2}}{Y_{\mathrm{O}_2,A}}, \quad \hat{T} = \frac{T - T_A}{\gamma T_A}, \tag{2.3}$$

and the dilution-adjusted stoichiometric ratio $S$ (i.e. the amount of oxygen needed to burn the unit mass of the fuel stream completely), the non-dimensional heat release $\gamma$, and the reciprocal-time pre-exponential factor $\hat{B}$, namely

$$S = \frac{sY_{\mathrm{F},F}}{Y_{\mathrm{O}_2,A}}, \quad \gamma = \frac{qY_{\mathrm{F},F}}{c_p T_A (1+S)}, \quad \hat{B} = \frac{\rho B Y_{\mathrm{O}_2,A}}{W_{\mathrm{O}_2}} \tag{2.4}$$

(where $c_p$ is the specific heat at constant pressure), the relevant conservation equations become

$$\frac{U}{(D_T A)^{1/2}}\frac{\partial \hat{Y}_{\mathrm{F}}}{\partial x} - y\frac{\partial \hat{Y}_{\mathrm{F}}}{\partial y} = \frac{\partial^2 \hat{Y}_{\mathrm{F}}}{\partial x^2} + \frac{\partial^2 \hat{Y}_{\mathrm{F}}}{\partial y^2} - \frac{\hat{B}}{A}\hat{Y}_{\mathrm{F}}\hat{Y}_{\mathrm{O}}\mathrm{e}^{-E_a/RT}, \tag{2.5}$$

$$\frac{U}{(D_T A)^{1/2}}\frac{\partial \hat{Y}_{\mathrm{O}}}{\partial x} - y\frac{\partial \hat{Y}_{\mathrm{O}}}{\partial y} = \frac{\partial^2 \hat{Y}_{\mathrm{O}}}{\partial x^2} + \frac{\partial^2 \hat{Y}_{\mathrm{O}}}{\partial y^2} - S\frac{\hat{B}}{A}\hat{Y}_{\mathrm{F}}\hat{Y}_{\mathrm{O}}\mathrm{e}^{-E_a/RT}, \tag{2.6}$$

$$\frac{U}{(D_T A)^{1/2}}\frac{\partial \hat{T}}{\partial x} - y\frac{\partial \hat{T}}{\partial y} = \frac{\partial^2 \hat{T}}{\partial x^2} + \frac{\partial^2 \hat{T}}{\partial y^2} + (1+S)\frac{\hat{B}}{A}\hat{Y}_{\mathrm{F}}\hat{Y}_{\mathrm{O}}\mathrm{e}^{-E_a/RT}. \tag{2.7}$$

The temperatures and compositions of the feed streams provide the boundary conditions

$$\hat{T} - \hat{T}_F = \hat{Y}_{\mathrm{F}} - 1 = \hat{Y}_{\mathrm{O}} = 0 \text{ as } y \to -\infty \quad \text{and} \quad \hat{T} = \hat{Y}_{\mathrm{F}} = \hat{Y}_{\mathrm{O}} - 1 = 0 \text{ as } y \to \infty, \tag{2.8}$$

where $\hat{T}_F = (T_F - T_A)/(\gamma T_A)$ measures the difference in temperature between the fuel and oxidizer streams. Upstream from the flame, the mixture is chemically frozen, corresponding to the boundary distributions

$$\hat{T}/\hat{T}_F = \hat{Y}_{\mathrm{F}} = 1 - \hat{Y}_{\mathrm{O}} = \frac{1}{2}\mathrm{erfc}\left(\frac{y}{\sqrt{2}}\right) \text{ as } x \to -\infty, \tag{2.9}$$

whereas the trailing diffusion flame that emerges downstream leads to the boundary condition

$$\frac{\partial \hat{T}}{\partial x} = \frac{\partial \hat{Y}_{\mathrm{F}}}{\partial x} = \frac{\partial \hat{Y}_{\mathrm{O}}}{\partial x} = 0 \text{ as } x \to \infty. \tag{2.10}$$

The two-dimensional boundary–value problem defined by (2.5)–(2.10) constitutes an eigenvalue problem in that the propagation velocity $U$ must be determined as an eigenvalue.

## 2.4 Simplifications of the formulation

The problem can be simplified by noting that, when Lewis numbers are unity, species mass fractions and the temperature are related to the mixture fraction according to

$$Z = \frac{S\hat{Y}_{\mathrm{F}} - \hat{Y}_{\mathrm{O}} + 1}{S+1} = \frac{\hat{T} + (1+S)\hat{Y}_{\mathrm{F}}}{\hat{T}_F + 1 + S}. \tag{2.11}$$

The mixture fraction $Z$ is unity in the fuel feed stream and zero in the oxidizer feed stream; it also satisfies a convective-diffusive balance, so that, under the present assumptions, its solution is given simply by

$$Z = \frac{1}{2}\mathrm{erfc}\left(\frac{y}{\sqrt{2}}\right). \tag{2.12}$$

Local stoichiometric conditions, defined by the equation $S\hat{Y}_{\mathrm{F}} = \hat{Y}_{\mathrm{O}}$, are reached on the planar surface $y = y_s$, where

$$Z_s = \frac{1}{S+1} = \frac{1}{2}\mathrm{erfc}\left(\frac{y_s}{\sqrt{2}}\right), \tag{2.13}$$

as follows from (2.11) and (2.12). The problem then reduces to that of integrating (2.7) supplemented with (2.11) and (2.12), employing for $\hat{T}$ its boundary conditions given in (2.8), (2.9) and (2.10).

In looking for an appropriate scale for $U$, one may note that, for weakly strained systems, the front becomes thinner than the mixing layer, and its propagation velocity $U$ then may logically be normalized by a relevant planar-deflagration speed. The specific value used below is

$$S_{L\infty,s} = \left[4(1-Z_s)\beta_s^{-3}\hat{B}D_T \mathrm{e}^{-E_a/RT_s}\right]^{1/2}, \tag{2.14}$$

the propagation velocity of the stoichiometric planar deflagration, as obtained at leading order in

the limit of large activation energy. Here

$$T_s = (1+\gamma)T_A + (T_F - T_A)Z_s \tag{2.15}$$

is the adiabatic flame temperature of the stoichiometric mixture and

$$\beta_s = \frac{E_a}{RT_s}\frac{T_s - T_A}{T_s} \tag{2.16}$$

is the stoichiometric Zel'dovich number. The accompanying value of the flame residence time $D_T/S_{L\infty,s}^2$ is selected as scale for the strain rate $\tilde{A}$ (or Karlovitz number). Introduction of these dimensionless variables

$$\tilde{U} = \frac{U}{S_{L\infty,s}} \quad \text{and} \quad \tilde{A} = \frac{D_T A}{S_{L\infty,s}^2}, \tag{2.17}$$

reduces (2.7) to

$$\frac{\tilde{U}}{\sqrt{\tilde{A}}}\frac{\partial \hat{T}}{\partial x} - y\frac{\partial \hat{T}}{\partial y} = \frac{\partial^2 \hat{T}}{\partial x^2} + \frac{\partial^2 \hat{T}}{\partial y^2} + \frac{\hat{\omega}}{Z_s\tilde{A}}, \tag{2.18}$$

where

$$\hat{\omega} = \frac{\beta_s^3 \hat{Y}_{\mathrm{F}}\hat{Y}_{\mathrm{O}}}{4(1-Z_s)}\exp\left[-\frac{\beta_s(\hat{T}_s - \hat{T})}{1-\sigma_s(\hat{T}_s - \hat{T})}\right] \tag{2.19}$$

is the dimensionless reaction rate, with $\sigma_s = \gamma T_A/T_s$ and $\hat{T}_s = (T_s - T_A)/(\gamma T_A) = 1 + \hat{T}_F Z_s$. The problem then finally reduces to that of integrating (2.18) subject to the boundary conditions

$$y \to -\infty: \quad \hat{T} = \hat{T}_F, \quad y \to \infty: \quad \hat{T} = 0, \tag{2.20}$$

$$x \to -\infty: \quad \hat{T} = \hat{T}_F Z, \quad x \to \infty: \quad \frac{\partial \hat{T}}{\partial x} = 0, \tag{2.21}$$

the value of $\tilde{U}$ serving as an eigenvalue that enables (2.21) to be satisfied. The reaction rate (2.19) must be evaluated with use of $\hat{Y}_{\mathrm{F}} = Z\hat{T}_s - Z_s\hat{T}$ and $\hat{Y}_{\mathrm{O}} = (1-Z) + (1-Z_s)(Z\hat{T}_F - \hat{T})$, obtained from (2.11), with $Z(y)$ given in (2.12).

The propagation velocity $U$ varies with the imposed counterflow strain rate $A$, from positive values for advancing triple flames at low values of $A$, to smaller positive values for advancing edge flames at higher values of $A$, where the fuel-rich and fuel-lean premixed flames have been folded back into the trailing diffusion flame, to negative values for retreating edge flames, at still larger values of $A$. Since the extinction strain rate $A_E$ for the one-dimensional diffusion flame that develops behind the triple flame is of order $S_{L\infty,s}^2/D_T$, the solution for the propagating triple flame can be anticipated to exist only for values of $\tilde{A}$ in the range $0 < \tilde{A} < \tilde{A}_E$ with $\tilde{A}_E = A_E/(S_{L\infty,s}^2/D_T) \sim 1$. At higher strain rates than this limiting value, the only steady solutions that exist are those for non-reacting flows. The present work explores characteristics of the solutions over the range of strain rates for which reacting-flow solutions exist, for values of parameters of practical interest.

## 2.5 Numerical methods and principal values of parameters

A pseudo-transient finite-element scheme with adaptive grid is employed in the numerical integration, which is marched in time until a steady solution is reached. The integration domain is a rectangular box chosen to be sufficiently large to satisfy the boundary conditions smoothly. The results shown below correspond to $x_{min} = -20,\ x_{max} = 20,\ y_{min} = -8,\ y_{max} = 8$. Since the problem defined above exhibits invariance under translations in the $x$ direction, to anchor the flame the additional condition $\hat{T} = 0.3$ is imposed at $x = 0$ along the stoichiometric line $y = y_s$. The parametric values $\beta_s = 8$ & $20$, representative of the range of overall activation energies usually encountered, $\sigma_s = 0.85$ (corresponding to typical amounts of heat release in flames) and $\hat{T}_F = 0$ (equal feed temperatures) are used in the integrations for three different values of stoichiometric ratio $S = (1, 4, 17.2)$. Here $S = 4$ and $S = 17.2$ are selected as representative of the conditions found in methane-oxygen and methane-air combustion, respectively.

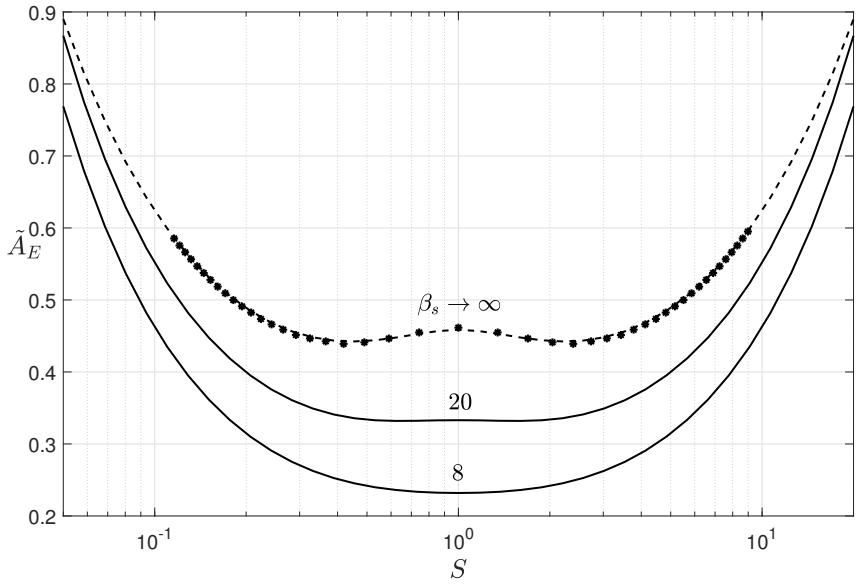


**Figure 2.2**: Extinction strain rate $\tilde{A}_E$ as a function of stoichiometric ratio $S$ for $\beta_s = 8,\ 20,\ \sigma_s = 0.85$ and $\hat{T}_F = 0$. The solid lines are obtained from numerical integration of (2.22). The dashed line is from [12] and the points are from [13].

## 2.6 Extinction strain rates

As previously mentioned, the steady triple flame cannot exist for strain rates above the extinction value $\tilde{A}_E$ of the one-dimensional diffusion flame that emerges for $x \to \infty$, described by integration of

$$\frac{\mathrm{d}^2\hat{T}_d}{\mathrm{d}y^2} + y\frac{\mathrm{d}\hat{T}_d}{\mathrm{d}y} + \frac{\hat{\omega}}{Z_s\tilde{A}} = 0, \quad \hat{T}_d(-\infty) = \hat{T}_F,\ \hat{T}_d(\infty) = 0, \tag{2.22}$$

obtained by neglecting $x$-derivative terms in (2.18). The value of $\tilde{A}_E$, obtained as the maximum value of $\tilde{A}$ for which there exists a solution to (2.22), is shown in figure 2.2 as a function of $S$ for the two values of $\beta_s$ considered here. For completeness, the numerical results are compared with the asymptotic predictions for $\beta_s \gg 1$ [12, 13].

It is interesting to observe that in this figure the results are symmetric about $S = 1$ when plotted on the log scale shown and that in the limit of large Zel'dovich numbers the curves exhibit an inflection point for $S < 1$ and another for $S > 1$. This aspect is present in both the numerical computation and the correlation formula shown by the dashed line, which gives a zero slope at

$S = 1$, and in this limit these results are independent of the value selected for $\sigma_s$, which appears only at the next order in the expansion. The asymptotic analysis for large Zel'dovich numbers involves stretching about the position of peak temperature, with matching to solutions in the outer inert zones. For the asymptotic predictions in the figure, the inner-zone equations are those of the diffusion-flame regime [12], which exhibit a smooth maximum for this curve when expanded about $S = 1$ but a positive (negative) slope when expanded for large (small) $S$, consistent with the existence of the inflection points seen in the figure. The figure shows that these inflection points disappear at realistic values of the Zel'dovich number, the decrease in the temperature sensitivity of the reaction rate reversing the dependence on $S$ found in the diffusion-flame regime.

## 2.7 Numerical Results

The influence of the stoichiometry of the fuel stream on the structure of the propagating flame is investigated in figure 2.3 for $\beta_s = 8$, $\sigma_s = 0.85$, $\hat{T}_F = 0$, and $S = 1, 4, 17$ at different strain rates $\tilde{A}$, by exhibiting contours of reaction rates $\hat{\omega}$ defined in (2.19). The front shapes for $\beta_s = 20$, not shown here, were found to be quite similar to those for $\beta_s = 8$, except for an overall reduction in the spatial extent of the reaction region, consistent with the stronger temperature sensitivity associated with the increase in activation energy.

To better identify the relative position of the flame, the stagnation plane $y = 0$ and the stoichiometric plane $y = y_s$ are represented in each plot by a dot-dashed line and a solid line, respectively. Two values of the strain rate are selected in the figure for each value of $S$, with the smaller value on the left corresponding to an advancing front with $\tilde{U} > 0$ and the higher value on the right corresponding to a retreating front with $\tilde{U} < 0$.

The symmetric solutions for $S = 1$, similar to those reported earlier [2, 3], result in a triple-flame structure for low strain rates and a retreating edge-flame structure for near-extinction strain rates, as is well known. It can be seen, however, that the symmetric character is lost for

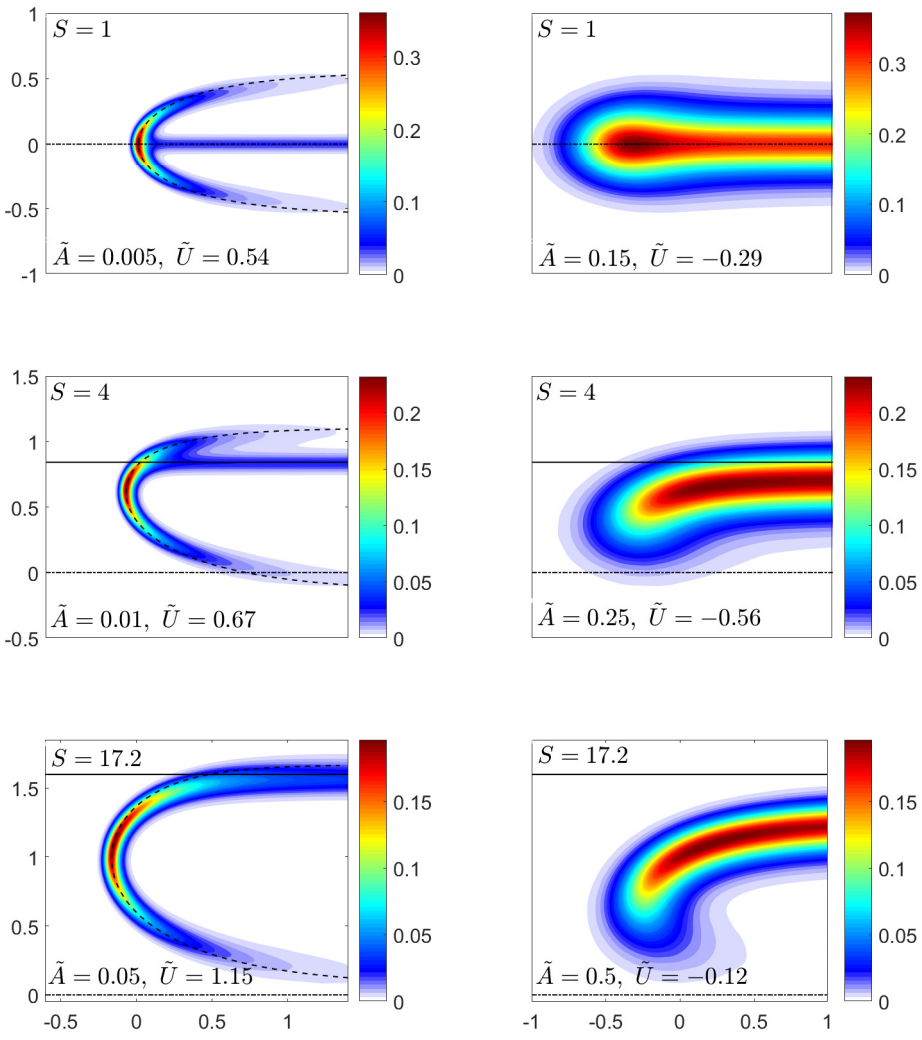


**Figure 2.3**: Left plots correspond to advancing fronts and right plots show retreating fronts. Solid lines represent stoichiometric locations, and the dash-dotted line is the stagnation plane. The dashed curves are flame shapes calculated from the thin-flame analysis.

$S = 4$, with the flame migrating to the oxidizer side of the mixing layer and the associated lean flame that develops for $y > y_s$ becoming very weak. At the higher strain rate for this value of $S$, the retreating edge flame bends away from stoichiometry, towards the stagnation plane, as it broadens.

The fading lean branch disappears altogether for $S = 17.2$, at which value the propagating front takes on a C shape, with one of the wings of the premixed front evolving into the trailing diffusion flame as $x \to \infty$. Also of interest is that at the lower strain rate selected for this figure, the front at $S = 17.2$ is found to propagate at a velocity $\tilde{U} = 1.15 > 1$, that is, higher than its stoichiometric value. This behavior, already reported without explanation for the range $\tilde{A} \ll \beta_s^{-2}$ [3] through asymptotic analysis, is clear from the investigation of composition dependence of one-dimensional planar flames [14], discussed in chapter 1, where it is shown that the peak of the laminar planar burning velocity for these large values of $S$, in general does not lie at the stoichiometric point, but instead is found at fuel-rich conditions. This aspect of earlier predictions of activation energy asymptotics for planar flames is a reflection of the leakage of the reactant in excess diminishing as stoichiometric conditions are approached, thereby tending to make the reaction rate asymptotically smaller.

Although the density decrease across curved flames is well known to increase propagation velocities in configurations such as this, that influence is absent in the present constant-density analysis, leading to the higher speed arising from the effect of the planar burning velocity. While the density-change influence would be largest at stoichiometric conditions, it is seen in the left-hand figure that, on the contrary, this C-shaped flame lies entirely in a fuel-rich region, bounded by the stoichiometric and the stagnation plane. From the right-hand plot, the retreating front is seen in the figure at this value of $S \gg 1$ to become hook-shaped, with the reaction rate of the retreating edge flame actually beginning to increase very far from stoichiometry, near the stagnation plane, where the available residence times are longer, allowing the heating of the mixture by the diffusion flame to have had more time to increase the reaction rate.

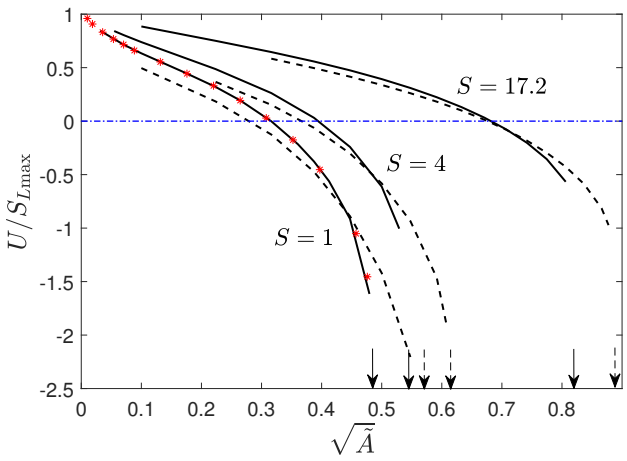


**Figure 2.4**: Triple-flame propagation velocity $U$ as a function of strain rate $\tilde{A}$ for $S = 1,\ 4,\ 17.2$, $\sigma_s = 0.85$ and $\hat{T}_F = 0$. Solid curves correspond to $\beta_s = 8$ and dashed curves to $\beta_s = 20$. The asterisk marks for $S = 1$ are from [3].

The computed dependence of the flame velocity on the strain rate is shown in figure 2.4 for the same three different values of $S$. Since for a given activation energy $\beta_s$, in the thermo-diffusive approximation the two-dimensional flame propagation velocity cannot exceed its one-dimensional planar maximum speed, $S_{L,\max}$, for any strain rate $\tilde{A}$ between ignition and extinction, i.e, $\tilde{U} < \tilde{S}_{L,\max}$, where $\tilde{S}_{L,\max}$ is the maximum value of numerically calculated planar propagation speed, $\tilde{S}_L = S_L/S_{L\infty,s}$, it is appropriate to plot the two-dimensional flame velocity normalized by its one-dimensional maximum velocity calculated in chapter 1. Besides the well-known decrease in $U$ with increasing $\tilde{A}$, the value of $U$ is seen to increase with $S$ at a fixed value of $\tilde{A}$, as a result of the leading point of the flame moving away from the stagnation plane into fluid moving more slowly in the direction of propagation of the triple flame. As can be seen, for each value of $S$ there exists an $\tilde{A}$ at which $\tilde{U} = 0$, thereby defining the boundary between advancing fronts and retreating fronts. The magnitude of the negative value of the propagation velocity of the retreating front goes to infinity as the strain rate approaches the extinction value $\tilde{A}_E$, although the computations have not been carried far into the range $\tilde{U} < 0$, where convergence difficulties become more accute. The limiting strain rate is different for the solid and dashed curves, consistent with the results shown in figure 2.2 for the two different activation energies considered here, the limiting

values being indicated by vertical arrows at the bottom of the figure.

## 2.8 Kinematics of thin fronts

As the strain rate becomes small, the flame becomes thin compared with its radius of curvature, enabling a more general analysis to be developed that is not necessarily restricted to the chemical kinetics selected for the numerical work discussed above. The initial analytical description of flame-front structures and propagation velocities in this limit of thin fronts, corresponding to low-strain feed streams in the present configuration, is due to Dold *et al.* [15–17], later extended to fuels with non-unity Lewis numbers by Daou & Liñán [2, 3], both works invoking activation-energy asymptotics in the description. It is, however, not necessary to adopt that approach in addressing the thin-flame limit, which may be analyzed directly by treating $\varepsilon = \sqrt{\tilde{A}}$ as a small parameter of expansion, thereby admitting reactions with more complex chemistry.

A front propagating at velocity $V_f$ into a fluid whose velocity field is $v$ may be described in a level-set approach by any constant value of a continuous and differentiable field function $G$ that obeys the equation

$$v \cdot \nabla G = V_f |\nabla G|, \tag{2.23}$$

when $n = -\nabla G/|\nabla G|$ is the local unit vector in the direction of propagation. To apply this description to the present problem, the components of $v$ are taken to be $(u,v) = (U, -Ay')$, and the field function is selected to be $G(x,y) = x - f(y)$ with $G = 0$ along the front. The flame shape is then given by $x = f(y)$, conditions along the flame sheet being treated as functions of $y$. A similar type of kinematic balance has been used previously in computing shapes of lifted flames in axisymmetric fuel jets under the additional approximation of negligible front-curvature effects [18].

In terms of the previously defined non-dimensional planar adiabatic laminar burning velocity $\tilde{S}_L(y)$, which can be obtained as an eigenvalue from (2.18), in place of $\tilde{U}/\sqrt{\tilde{A}}$, after

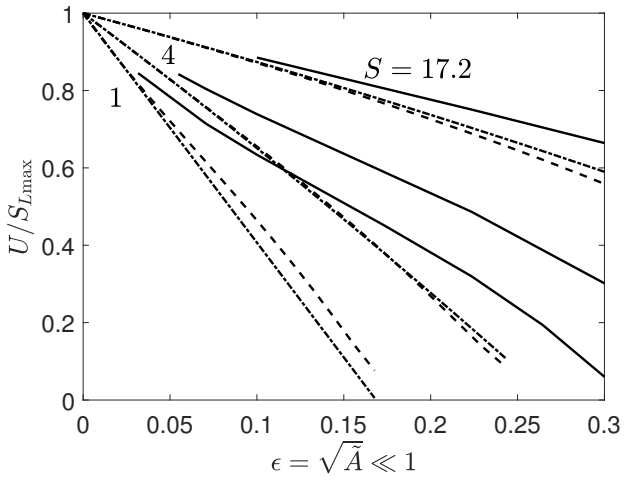


**Figure 2.5**: The dashed lines are obtained from the numerical integration of (2.25) and the dashed-dotted curves are the results of the perturbation analysis given in the final equation in the appendix. All solid curves are the actual two-dimensional computational results.

neglecting transverse gradient terms (irrespective of the functional form of the reaction rate), a non-dimensional laminar-flame thickness for a low strain rate can be defined as $\delta_L(y)/\delta_m = \sqrt{\tilde{A}}/\tilde{S}_L$. Based on this definition, with chemical-kinetic descriptions that result in identical Markstein numbers for curvature and strain, for fronts with small curvature, the local burning velocity can be expressed in dimensional form [19–21] as

$$V_f = S_L - S_L \mathscr{M} \delta_L \kappa + \mathscr{M} \delta_L n \cdot \nabla v \cdot n. \tag{2.24}$$

Here $\mathscr{M}$ is the Markstein number, $n$ is the unit normal pointing towards unburnt gas, and $\kappa = \nabla \cdot n$ is the front curvature, $-n \cdot \nabla v \cdot n$ being the imposed strain rate associated with the velocity gradients.

After non-dimensionalization, for small flame curvature, the curvature term in the preceding equation becomes of order $\varepsilon$, while the strain-rate term becomes of order $\varepsilon^2$. Both of these terms are retained in the analysis given in the appendix, the results of which are employed in the comparisons to be given below, but in order to reveal the character of the problem more simply and clearly, the higher-order strain-rate term is neglected here. Following geometrical resolution

in the $(x,y)$ plane, in terms of the unknown function $g(y) = df/dy$, the equation then simplifies to the nonlinear first-order ordinary differential equation

$$\tilde{U} + \varepsilon y g = \tilde{S}_L \sqrt{1+g^2} - \varepsilon \frac{\mathscr{M}}{1+g^2} \frac{\mathrm{d}g}{\mathrm{d}y}, \tag{2.25}$$

where $\mathscr{M}$ is the Markstein number for curvature, which, in general, varies with $y$ along the front. The solution to this equation for $g$ describes a C-shaped flame when $df/dx$ approaches zero with a positive slope at a higher value of $y$, to be denoted by $y_\infty$, and also approaches zero with a negative slope at a lower value of $y$, to be denoted by $y_{-\infty}$. These requirements translate into the requirements that $g$ approaches positive infinity at $y_\infty$ and negative infinity at $y_{-\infty}$. This then defines a two-point boundary-value problem that possesses a continuous and differentiable solution $g(y)$ only for a particular value of the constant $\tilde{U}$, thus constituting a nonlinear eigenvalue problem. Since the curvature term vanishes in the extreme wings of the C, the boundary conditions are found to be

$$g \to \frac{\tilde{U}}{\pm(\tilde{S}_L) - \varepsilon y}, \tag{2.26}$$

the upper sign applying at $y_\infty$ and the lower sign at $y_{-\infty}$.

Through its relationship to the mixture-fraction function, $Z(y)$, the variation of the planar laminar burning velocity with the equivalence ratio defines the function $\tilde{S}_L(y)$, which will achieve its maximum value $S_m = S_{L,\max}/S_{L\infty,s}$ at a value of $y$ denoted by $y_m$. It is evident from (2.25) that in the limit $\varepsilon = 0$ the constant $\tilde{U}$ cannot be less than $S_m$ since the magnitude of the square root is never less than unity, nor can it be greater than $S_m$, since then the entire pattern would propagate faster than any element of the front. Hence, at leading order in $\varepsilon$, the pattern must propagate in the $x$ direction at the velocity $\tilde{U} = S_m$. The solution for the shape of the front at this leading order then becomes simply

$$g(y) = \pm \left( \frac{S_m^2}{\tilde{S}_L^2} - 1 \right)^{1/2}, \tag{2.27}$$

the upper sign applying for $y > y_m$ and the lower sign for $y < y_m$.

Since $\tilde{U} = S_m$ at leading order, the first correction to $\tilde{U}$ arising from the front curvature is determined by the variation of $\tilde{S}_L(y)$ in the vicinity of the point $y = y_m$. This observation motivates considering an expansion of the burning velocity about $\tilde{S}_L(y) = S_m$. With the normal quadratic variation about the maximum, in the first approximation $\tilde{S}_L(y) = S_m - (a/2)(y-y_m)^2$, where the positive constant $a$ is the negative of the second derivative of the planar burning velocity with respect to $y$ at $y = y_m$. When this expansion is substituted into (2.25) and terms of order $\varepsilon$ are collected, it is found that the perturbation to $g(y)$ diverged in proportion to $1/(y-y_m)$ as $y$ approaches $y_m$ unless $\tilde{U} = S_m - \varepsilon \mathscr{M}(y_m)(a/S_m)^{1/2}$. This determines the first correction to the propagation velocity of the pattern, and further pursuit of the perturbation analysis, summarized in the appendix for the value $\mathscr{M} = 1$, which applies in the thermo-diffusive approximation in the limit of infinite Zel'dovich number, serves to determine subsequent corrections to the location $y = y_m$ of the turning point, $y = y_t$, as well as the front shape.

It may be noted that, in this analysis, the propagation velocity is determined by imposing analyticity of the solution at the turning point, the nose of the pattern, where the front is normal to the $x$ direction. This critical point in the analysis coincides with the leading point only in the symmetric case, $S = 1$; for other values of $S$, this vertical slope does not occur at $y = 0$, so the flow velocity is not normal to the front at that point. From the viewpoint of this development, therefore, conditions at the turning point, rather than at the the leading point, serve to determine the propagation velocity of the pattern.

## 2.9 Comparisons of thin-front predictions

Although limited to a Markstein number of unity, the starting differential equation in the appendix includes the effects of both curvature and strain rate, the latter not having been addressed previously for a problem of this type. That differential equation was integrated numerically,

employing the planar burning-velocity functions associated with our initial formulation, also obtained by numerical integration, for various stoichiometries $S$, with different values of $\varepsilon$. Representative results are shown as dashed curves in the plots on the left in figure 2.3. The dashed curves are seen to coincide well with the contours of maximum reaction rate, irrespective of whether the front lies mainly in the fuel-rich region. While this general agreement would be anticipated at these low counterflow strain rates, it may be noted that even in the lower left-hand graph, where the value of the small parameter is $\varepsilon > 0.2$, the agreement remains quite good. Thin-flame descriptions therefore may be considered to be quite robust for describing the C-shaped curves in these problems. Computations also were made employing the expansion developed in the appendix in place of a numerical integration, and the results were practically indistinguishable from those shown in the figure. Even the simple leading-order result given in equation (2.27) provides fairly reasonable curved premixed-flame shapes.

Predictions of propagation velocities of C-flame patterns are compared in the inner plot of figure 2.4 for a Zel'dovich number of $\beta_s = 8$. As can be seen in this figure, at this value of the Zel'dovich number the thin-flame propagation-velocity predictions begin to depart noticeably from those of the complete numerical integrations at a value of $\varepsilon$ that increases as $S$ increases, reaching $\varepsilon = 0.1$ at $S = 17.2$. The thin-flame propagation-velocity predictions thus are somewhat less robust than the corresponding flame-shape predictions. Although the predicted linear dependence on $\varepsilon$ is seen to be good, the propagation velocities calculated here in the thin-flame limit decrease more rapidly with increasing $\varepsilon$ than is found by the full integration. This is likely a consequence of selecting a Markstein number of unity for the thin-front description; this value of the Zel'dovich number is small enough that the variation with the counterflow strain rate may be expected to be weaker than would occur in the limit of infinite Zel'dovich number, so the departure of the Markstein number from unity may be expected to exert a noticeable influence on the thin-flame behavior. The thin-flame description employing the expansion derived in the appendix is seen in this plot to be in good agreement with results of the numerical integration of the thin-flame

equation over the values of $\varepsilon$ shown, whence the thin-flame formulation is likely to be reasonably accurate over this range, but proper evaluations of Markstein numbers are needed to achieve good accuracy.

## 2.10 Conclusions

The main conclusion to be drawn from this investigation is that not all partially premixed flames in counterflow configurations may be expected to exhibit the classical tribrachial structure of rich and lean premixed flames with a diffusion flame trailing behind. Especially at high values of the dilution-adjusted stoichiometric fuel-air ratio, such as values appropriate for methane-air flames, the diffusion flame may fade into the lean wing, with the triple flame then evolving into a fuel-rich C-shaped premixed flame. Since the analysis leading to this prediction employs the thermo-diffusion approximation, heat release may modify this configuration, bringing the trailing diffusion flame back into visibility, yet the asymmetry in the direction identified here is likely to remain. Totally symmetric triple flames therefore should not be anticipated to be prevalent in practical situations.

A further notable finding is that, although not at all applicable to retreating or even to advancing edge flames, thin-flame approximations enable Markstein numbers to be applied, employing quite general chemical kinetics, to reduce the problem involving ordinary differential equations in place of more complex partial differential equations, to quantify the flame shape and the propagation speed, even though full equations or activation energy asymptotics [3] are needed to resolve the flame structure. Moreover, in the limit of small strain rates, instead of integrating ordinary differential equations, sequential solutions of purely algebraic equations suffice to produce the results that are needed. It could be worthwhile to extend simpliiňĄcations of that type to address the important influences of density changes associated with the heat release. These are known to modify appreciably the velocity field, including an outward deflection of

the incoming streamlines upstream from the triple flame, which in turn results in an order-unity increase of the propagation velocity. Associated changes to the mixture-fraction fields can be expected to modify quantitatively the results presented above, and these should be investigated in future work.

This chapter, in part, has been published in *Proceedings of the Combustion Institute*, "Influences of stoichiometry on steadily propagating triple flames in counterflows", by P. Rajamanickam, W. Coenen, A. L. Sánchez and F. A. Williams (2019) **37**, 1971-1977. The dissertation author is the primary investigator in this publication.

# Appendix

It is convenient to employ the re-scalings $\hat{U} = \tilde{U}/S_m$, $\hat{S}_L = \tilde{S}_L/S_m$ and $\hat{\varepsilon} = \varepsilon/S_m$, whence, with a Markstein number of unity, as in earlier work [3, 22], equation (2.24) becomes

$$\hat{U} + \hat{\varepsilon} y g = \hat{S}_L \sqrt{1+g^2} - \hat{\varepsilon} \frac{\mathrm{d}g/\mathrm{d}y}{1+g^2} - \hat{\varepsilon}^2 \frac{g^2}{\hat{S}_L \sqrt{1+g^2}}. \tag{2.28}$$

After introducing the perturbation series $g = g_o + \hat{\varepsilon} g_1 + \hat{\varepsilon}^2 g_2 + \cdots$ and $\hat{U} = U_o + \hat{\varepsilon} U_1 + \hat{\varepsilon}^2 U_2 + \cdots$ into (2.28), the resulting problem becomes purely algebraic in nature for the unknown quantities at each successive order. A unique choice of the eigenvalue at each order makes the solution uniformly valid in $y$ by eliminating non-analyticity at the turning point. A Taylor's expansion of $\tilde{S}_L(y)$ around the maximum point is needed,

$$\hat{S}_L = 1 + \delta^2 \frac{\hat{S}''_m}{2!} + \delta^3 \frac{\hat{S}'''_m}{3!} + \delta^4 \frac{\hat{S}^{iv}_m}{4!} + \cdots, \tag{2.29}$$

where $\delta = y - y_m$, and $\hat{S}''_m, \hat{S}'''_m, \ldots$ are derivatives of $\hat{S}_L(y)$ evaluated at the maximum location. The turning-point location is also an unknown quantity that can be expanded in series $y_t =$

$y_m + \hat{\varepsilon} y_1 + \hat{\varepsilon}^2 y_2 + \cdots$. The boundary conditions at $y_{\pm\infty}$,

$$g \to \frac{\hat{U}}{\pm(\hat{S}_L - \hat{\varepsilon}^2/\hat{S}_L) - \hat{\varepsilon} y}, \tag{2.30}$$

obtained from equation (2.28) as limiting forms, are satisfied automatically at each order. The domain interval $(y_{-\infty}, y_{\infty})$ itself is obtained by setting the denominator of (2.30) to zero.

The leading-order equation then leads to

$$g_o(y) = \pm(\delta)\left(\frac{U_o^2}{\hat{S}_L^2} - 1\right)^{1/2}. \tag{2.31}$$

The choice $U_o > 1$ will result in a discontinuity for $g_o(y)$ at $\delta = 0$, and the choice $U_o < 1$ gives a complex solution, so the only way that $g_o(y)$ can be made real and continuous at the inner region (i,e., in the vicinity of $\delta = 0$, since, at leading order, the turning point is simply $y_t = y_m$) is to choose $U_o = 1$.

Collecting terms of $O(\hat{\varepsilon})$ and solving for $g_1(y)$ gives

$$g_1(y) = \frac{U_1}{\hat{S}_L^2 g_o} + \frac{y}{\hat{S}_L^2} + \frac{1}{g_o}\frac{\mathrm{d}g_o}{\mathrm{d}y}. \tag{2.32}$$

The behaviour of $g_1(y)$ as it approaches the turning point $y \to y_t = y_m + \hat{\varepsilon} y_1$ is found to be

$$g_1(y) \sim \delta^{-1}\left[\frac{U_1}{\sqrt{-\hat{S}_m''}} + 1\right] + O(1). \tag{2.33}$$

The choice $U_1 = -\sqrt{-\hat{S}_m''}$ is needed to make $g_1(y)$ be bounded as the inner region is approached. Through terms of first order, then,

$$g(y) = \pm|g_o(y) + \hat{\varepsilon} g_1(y)| + O(\hat{\varepsilon}^2). \tag{2.34}$$

from which $y_m + \hat{\varepsilon} y_1$ is obtained as the value of $y$ at which $g_o(y) + \hat{\varepsilon} g_1(y) = 0$.

In the same spirit, the equation for $g_2(y)$ is obtained at the next order from,

$$g_2(y) = \frac{U_2}{\hat{S}_L^2 g_o} + \frac{y g_1}{\hat{S}_L^2 g_o} - \frac{g_1^2}{2 g_o} + \frac{\hat{S}_L^2 g_o g_1^2}{2} + \frac{1}{g_o}\frac{\mathrm{d}g_1}{\mathrm{d}y} - 2\hat{S}_L^2 g_1 \frac{\mathrm{d}g_o}{\mathrm{d}y} + \frac{g_o}{\hat{S}_L^2}, \tag{2.35}$$

its behaviour as $y \to y_m + \hat{\varepsilon} y_1 + \hat{\varepsilon}^2 y_2$ being given by

$$g_2(y) \sim \frac{\delta^{-1}}{\sqrt{-\hat{S}_m''}} \left[ U_2 + y_m \gamma_1 - \frac{\gamma_1^2}{2} + \gamma_2 \right] + O(1), \tag{2.36}$$

where

$$\gamma_1 = y_m - \frac{\hat{S}_m'''}{3(-\hat{S}_m'')},\ \gamma_2 = 1 - \frac{7\hat{S}_m'''^2}{72\hat{S}_m''^2} - \frac{\hat{S}_m^{iv}}{8(-\hat{S}_m'')}, \tag{2.37}$$

and $U_2$ is chosen so as to remove the divergence at $\delta = 0$. The selection of the value of $U_1$ has eliminated a term of order $\delta^{-2}$, which otherwise would appear. The uniform solution at this order is given by

$$g(y) = \pm \left\| \pm |g_o + \hat{\varepsilon} g_1| + \hat{\varepsilon}^2 g_2 \right\| + O(\hat{\varepsilon}^3), \tag{2.38}$$

with the new turning point $y_t = y_m + \hat{\varepsilon} y_1 + \hat{\varepsilon}^2 y_2$ now being determined by requiring the expression inside the outer absolute value signs to vanish there. At this order, the eigenvalue is

$$\hat{U} = 1 - \hat{\varepsilon}\sqrt{-\hat{S}_m''} + \hat{\varepsilon}^2 \left( \frac{\gamma_1^2}{2} - \gamma_2 - y_m \gamma_1 \right) + O(\hat{\varepsilon}^3). \tag{2.39}$$

# Bibliography


[1] P. Phillips. Flame in a buoyant methane layer. *Symposium (International) on Combustion*, 10(1):1277–1283, 1965.

[2] J. Daou and A. Liñán. Triple flames in mixing layers with nonunity lewis numbers. *Symposium (International) on Combustion*, 27(1):667–6743, 1998.

[3] J. Daou and A. Liñán. The role of unequal diffusivities in ignition and extinction fronts in strained mixing layers. *Combustion Theory and Modelling*, 2(4):449–477, 1998.

[4] M. S. Cha and P. D. Ronney. Propagation rates of nonpremixed edge flames. *Combustion and Flame*, 146(1):312–328, 2006.

[5] H. Song, P. Wang, R. S. Boles, D. Matinyan, H. Prahanphap, J. Piotrowicz, and P. D. Ronney. Effects of mixture fraction on edge-flame propagation speeds. *Proceedings of the Combustion Institute*, 36(1):1403–1409, 2017.

[6] A. J. Juanós and W. A. Sirignano. Triple flame: Inherent asymmetries and pentasectional character. *Combustion Theory and Modelling*, 18(3):454–473, 2014.

[7] Eduardo Fernández-Tarrazo, Antonio L Sánchez, Amable Liñán, and Forman A Williams. A simple one-step chemistry model for partially premixed hydrocarbon combustion. *Combustion and Flame*, 147(1):32–38, 2006.

[8] Charles K Westbrook and Frederick L Dryer. Simplified reaction mechanisms for the oxidation of hydrocarbon fuels in flames. *Combustion Science and Techolology*, 27(1-2):31–43, 1981.

[9] B Michaelis and B Rogg. Fem-simulation of laminar flame propagation ii: twin and triple flames in counterflow. *Combustion Science and Technology*, 177(5-6):955–978, 2005.

[10] K. P Liao, M Matalon, and C Pantano. A flow pattern that sustains an edge flame in a straining mixing layer with finite thermal expansion. *Proceedings of the Combustion Institute*, 35(1):1015–1021, 2015.

[11] J Barry Greenberg, Leonid S Kagan, and G. I. Sivashinsky. Effect of a fuel spray on edge flame propagation. *Atomization and Sprays*, 22(4):333–349, 2012.

[12] A. Liñán. The asymptotic structure of counterflow diffusion flames for large activation energies. *Acta Astronautica*, 1(7):1007–1039, 1974.

[13] A. Liñán, D. Martínaz-Ruiz, M. Vera, and A. L. Sánchez. The large-activation-energy analysis of extinction of counterflow diffusion flames with non-unity lewis numbers of the fuels. *Combustion and Flame*, 175:91–106, 2017.

[14] P. Rajamanickam. On the two-reactant one-step activation-energy asymptotics for steady, adiabatic, planar flames with lewis numbers of unity. *Combustion Theory and Modelling*, 22(5):913–920, 2018.

[15] J. W. Dold. Flame propagation in a nonuniform mixture: analysis of a slowly varying triple flame. *Combustion and Flame*, 76(1):71–88, 1989.

[16] L. J. Hartley and J. W. Dold. Flame propagation in a nonuniform mixture: analysis of a propagating triple-flame. *Combustion Science and Technology*, 80(1-3):23–46, 1991.

[17] J. W. Dold, L. J. Hartley, and D. Green. Dynamics of laminar triple-flamelet structures in non-premixed turbulent combustion. In *Dynamical issues in combustion theory*, pages

83–105. Springer, 1991.

[18] A Revuelta, Antonio L Sánchez, and A Liñán. Laminar mixing in diluted and undiluted fuel jets upstream from lifted flames. *Combustion and Flame*, 128(3):199–210, 2002.

[19] N. Peters. *Turbulent combustion*. Cambridge university press, 2000.

[20] P. Clavin and G. Searby. *Combustion Waves and Fronts in Flows: Flames, Shocks, Detonations, Ablation Fronts and Explosion of Stars*. Cambridge University Press, 2016.

[21] A. Liñán and F. A. Williams. *Fundamental Aspects of Combustion*. Oxford University Press, New York, 1993. eqn.(5.14), pp.119-132.

[22] P. Clavin. Dynamic behavior of premixed flame fronts in laminar and turbulent flows. *Progress in Energy and Combustion Science*, 11(1):1–59, 1985.

# Chapter 3

# Near-limit $H_2$-$O_2$-$N_2$ combustion in nonpremixed counterflow mixing layers

## 3.1 Introduction

Criticality conditions in hydrogen-oxygen combustion are fundamentally related to the existence of a chemical-kinetic crossover temperature $T_c$ at which the effective rates of high-temperature chain branching, associated with the shuffle reactions, and chain recombination, mainly controlled by the three-body reaction H+$O_2$+M $\rightarrow$ $HO_2$+M, are equal [1]. Chain branching dominates when the temperature in the reaction region lies above crossover, leading to the existence of a well-populated radical pool that maintains a high fuel oxidation rate, with characteristic times on the order of 1 ms. This branching path is no longer active below crossover, where chain-terminating processes are dominant. In this low-temperature regime, sustained hydrogen combustion relies instead on an extremely slow branching path involving $HO_2$ and $H_2O_2$, resulting in negligibly small oxidation rates. This is known to have a dramatic effect on ignition processes, for example, with associated induction times increasing to very large values (exceeding one second at $p = 1$ atm) when the initial temperature falls below crossover. Because

of this drastic change of reactivity, $H_2$-$O_2$ premixed and nonpremixed flames can exist only when the reaction-layer temperature lies above $T_c$ which thus determines the flammability limit.

Since branching and recombination tend to balance as the peak temperature approaches $T_c$, the effective rate of hydrogen oxidation becomes small in near-limit flames. The resulting weakly reactive solutions are affected by preferential-diffusion interactions that lead to known diffusive-thermal instabilities, which play a central role in the dynamics of near-critical $H_2$-$O_2$ combustion. For instance, they are responsible for the emergence of pulsating planar deflagrations in rich $H_2$-$O_2$ mixtures and for the formation of cellular flames in very lean $H_2$-$O_2$ mixtures [2]. In the latter case, the resulting curved flames, approaching flame-ball structures as limiting solutions [3], display superadiabatic flame temperatures, so that they can exist under conditions where planar deflagrations cannot, thereby extending significantly the lean flammability limit. A wide variety of similar dynamic phenomena has been recently observed [4] in experiments of $H_2$-$O_2$-$N_2$ nonpremixed flames in a slot-jet facility when the conditions of dilution and strain produce peak temperatures approaching $T_c$. These conditions are to be further investigated in the present chapter with the objective of providing a more complete characterization of the dynamical behavior of nonpremixed $H_2$-$O_2$ combustion through additional experiments and numerical computations.

The new results presented below, exploring extended ranges of strain rate, stoichiometry, and dilution, will be related to those of previous numerical analyses of differential-diffusion effects in counterflow nonpremixed systems [5–9]. These previous studies considered reactants with general Lewis numbers undergoing an irreversible reaction with a rate having unity reaction orders and a power-law [6, 8] or Arrhenius [5, 7, 9], temperature dependence. Instead, our computations will focus directly on the specific chemistry and transport properties pertaining to $H_2$-$O_2$-$N_2$ mixtures, as is needed to enable quantitative comparisons with the experimental measurements for given conditions of reactant-feed composition and strain to be made. Exploratory computations using a chemical-kinetic mechanism with 12 elementary reactions, which has been shown to provide excellent accuracy for most combustion conditions [10], revealed that for the

nonpremixed flames investigated here the effects of reactions involving $H_2O_2$ and of the initiation steps $H_2$+$O_2 \overset{6b}{\rightarrow} HO_2$+H and $H_2$+M $\overset{9b}{\rightarrow}$ H+H+M are negligibly small, so that the needed chemistry description reduces to the nine elementary reactions shown in Table 3.1. As shown recently [11], an even simpler chemistry description can be developed sufficiently close to crossover by exploiting the fact that all radicals obey a steady-state approximation, so that hydrogen oxidation can be described with a single overall reaction, whose rate can be expressed in explicit form in terms of the temperature and the reactant concentrations. The present investigation focuses on near-extinction highly strained flames, for which steady-state approximations tend to deteriorate, as demonstrated recently [12]. For this reason, although the one-step reduced mechanism is in principle well-suited for the near-limit flames investigated here, for increased reliability the computations presented below will employ instead the complete short mechanism of Table 3.1.

**Table 3.1**: Rate coefficients in Arrhenius form $k = BT^n \exp(-T_a/T)$ for the skeletal mechanism with rate parameters in mol, s, $cm^3$, kJ, and K.

| | Reaction | | $B$ | $n$ | $T_a$ |
|---|---|---|---|---|---|
| 1f | $H+O_2 \rightarrow OH+O$ | | $3.52\ 10^{16}$ | -0.7 | 8590 |
| 1b | $OH+O \rightarrow H+O_2$ | | $1.05\ 10^{14}$ | -0.313 | 132 |
| 2f | $H_2+O \rightarrow OH+H$ | | $5.06\ 10^{4}$ | 2.67 | 3165 |
| 2b | $OH+H \rightarrow H_2+O$ | | $2.94\ 10^{4}$ | 2.64 | 2430 |
| 3f | $H_2+OH \rightarrow H_2O+H$ | | $1.17\ 10^{9}$ | 1.3 | 1825 |
| 3b | $H_2O+H \rightarrow H_2+OH$ | | $1.42\ 10^{10}$ | 1.18 | 9379 |
| 4f | $H+O_2+M \rightarrow HO_2+M$[a] | $k_0$ | $5.75\ 10^{19}$ | -1.4 | 0.0 |
| | | $k_\infty$ | $4.65\ 10^{12}$ | 0.44 | 0.0 |
| 5f | $HO_2+H \rightarrow OH+OH$ | | $7.08\ 10^{13}$ | 0.0 | 148 |
| 6f | $HO_2+H \rightarrow H_2+O_2$ | | $1.66\ 10^{13}$ | 0.0 | 414 |
| 7f | $HO_2+OH \rightarrow H_2O+O_2$ | | $2.89 \times 10^{13}$ | 0.0 | $-250$ |
| | | | $4.50\ 10^{14}$ | 0.0 | 5500 |
| 8f | $H+OH+M \rightarrow H_2O+M$[b] | | $4.00 \times 10^{22}$ | -2.0 | 0.0 |
| 9f | $H+H+M \rightarrow H_2+M$[c] | | $1.30\ 10^{18}$ | -1.0 | 0.0 |

## 3.2 Formulation

We consider the mixing layer separating two counterflowing slot jets at temperature $T_o = 298$ K. The oxidizer and fuel streams are assumed to be a mixture of $O_2$ and $N_2$ with oxygen mass fraction $Y_{O_2 o}$ and a mixture of $H_2$ and $N_2$ with fuel mass fraction $Y_{H_2 o}$. In nonpremixed combustion the reactants reach the reaction layer in stoichiometric proportions, so there is interest in relating the composition of the feed streams to the composition of the stoichiometric gas mixture obtained by combining one unit mass of the fuel stream with $8Y_{H_2 o}/Y_{O_2 o}$ units of mass of the oxidizer stream, resulting in a mixture with volumetric proportionality that can be written as $H_2$:$O_2$:$N_2$=2:1:$N$. Following [4], we thus choose to characterize the stoichiometry and dilution of the system in terms of the stoichiometric mixture fraction $Z_s = 1/(1+8Y_{H_2 o}/Y_{O_2 o})$ and a parameter $N$, defined as the ratio of the number of moles of inert to the number of moles of oxygen in a mixture formed by combining the fuel and oxidizer streams in stoichiometric proportions. These two quantities determine the boundary values of the reactant mass fractions according to

$$Y_{H_2 o} = \frac{1}{Z_s(9+7N)} \quad \text{and} \quad Y_{O_2 o} = \frac{8}{(1-Z_s)(9+7N)}. \tag{3.1}$$

By modifying the relative dilution of the feed streams while keeping the value of $N$ constant one may vary the stoichiometric mixture fraction in the range

$$\frac{1}{9+7N} \leq Z_s \leq \frac{1+7N}{9+7N}, \tag{3.2}$$

where the lower and upper limiting values correspond to pure fuel ($Y_{H_2 o} = 1$) and pure oxygen ($Y_{O_2 o} = 1$), respectively. When $N$ is large, as it is near critical conditions, this range extends from nearly zero to nearly unity.

In the thermo-diffusive approximation of constant density $\rho$ and constant transport properties, adopted here to simplify the numerical description, the velocity in the mixing layer is given

by the familiar stagnation-point flow solution $(v_x, v_y, v_z) = (0, -Ay', Az')$ in terms of the strain rate $A$, independent of time. As in [6–8] the composition and temperature of the resulting reactive flow will be assumed to be independent of $z'$, thereby reducing the time-dependent conservation equations for the reactive species $i$ and energy to

$$\frac{\partial Y_i}{\partial t} - y\frac{\partial Y_i}{\partial y} - \frac{1}{L_i}\left(\frac{\partial^2 Y_i}{\partial x^2} + \frac{\partial^2 Y_i}{\partial y^2}\right) = \frac{\dot{m}_i}{\rho A} \tag{3.3}$$

$$\frac{\partial T}{\partial t} - y\frac{\partial T}{\partial y} - \left(\frac{\partial^2 T}{\partial x^2} + \frac{\partial^2 T}{\partial y^2}\right) = -\frac{\sum_i h_i^o \dot{m}_i}{\rho A c_p} \tag{3.4}$$

involving the temperature $T$ and the species mass fractions $Y_i$ as dependent variables and the dimensionless time $t = At'$ and the dimensionless coordinates $x = x'/\sqrt{D_T/A}$ and $y = y'/\sqrt{D_T/A}$ as independent variables, with $D_T$ denoting the constant thermal diffusivity. In writing (3.4), the specific heat at constant pressure $c_p$ is assumed to be constant, a reasonably good approximation for highly diluted $H_2$-$O_2$ combustion systems. The expression $c_p = 32 \times 10^{-3}(3+N)/(36+28N)$ J/(kg K), which approximates the specific heat of a stoichiometric mixture $H_2$:$O_2$:$N_2$=2:1:$N$ at $T = 1000$ K, is used in the integrations.

A Fickian description with constant Lewis number $L_i$ is adopted in the transport description, with the values $L_{H_2} = 0.29$, $L_{O_2} = 1.10$, $L_{H_2O} = 0.89$, $L_H = 0.18$, $L_{OH} = 0.71$, $L_O = 0.69$, and $L_{HO_2} = 1.08$ used in the computations shown below, as corresponds to flames diluted with nitrogen, whose mass fraction is determined from those of the reactive species with use of $Y_{N_2} = 1 - \sum_i Y_i$. As anticipated in earlier work [4], differential-diffusion effects will be seen below to be more pronounced in systems with larger stoichiometric mixture fraction $Z_s$, when the hydrogen diffusivity dominates reactant transport. Because of the relatively limited temperature range at near-critical conditions with feed streams at 298 K, which also favors improved accuracy of the thermo-diffusive approximations, in addition Soret diffusion is neglected for simplicity.

The source terms in (3.3) and (3.4) involve the mass production rates per unit volume $\dot{m}_i$ and the enthalpies of formation $h_i^o$. The former is evaluated with use of the nine-step mechanism

shown in Table 3.1. The rate constants shown, including falloff for the reaction H+$O_2$+M $\overset{4f}{\rightarrow}$ $HO_2$+M and a bi-Arrhenius expression for the reaction $HO_2$+OH $\overset{7f}{\rightarrow}$ $H_2O$+$O_2$, are taken from the San Diego mechanism [13]. The species concentrations are calculated without invoking the assumption of constant density by using the expression

$$C_i = \frac{p}{R^o T} \frac{Y_i/M_i}{\sum_i Y_i/M_i}, \tag{3.5}$$

where $R^o = 8.314$ J/(mol K) is the universal gas constant, $M_i$ is the molecular mass of species $i$, and $p = 1$ atm is the pressure.

A rectangular computational domain with boundaries $y = \pm y_{max}$ and $x = \pm x_{max}$ will be considered in the integrations. Associated boundary conditions for the temperature and reactant mass fractions at the upper and lower boundaries are $Y_{\mathrm{H}_2} = Y_{\mathrm{O}_2} - Y_{\mathrm{O}_2 o} = T - T_o = 0$ at $y = +y_{max}$ and $Y_{\mathrm{H}_2} - Y_{\mathrm{H}_2 o} = Y_{\mathrm{O}_2} = T - T_o = 0$ at $y = -y_{max}$, as correspond to the conditions in the feed streams, all other reactive species having a zero mass fraction there. On the other hand, Neumann conditions $\partial T/\partial x = \partial Y_i/\partial x = 0$ are used on the lateral boundaries $x = \pm x_{max}$. This selection allows for the existence of both one-dimensional and two-dimensional flames, with the investigation of the latter requiring consideration of sufficiently large values of $x_{max}$, as needed to guarantee that the solution is independent of the lateral extent of the computational domain.

## 3.3 Preliminary considerations pertaining to near-limit $H_2$-$O_2$ diffusion flames

In hydrogen-oxygen combustion, the main chain-branching path at high temperature is established by the rate-controlling reaction H+$O_2$ $\overset{1f}{\rightarrow}$ OH+O followed by the faster O and OH consumption reactions O+$H_2$ $\overset{2f}{\rightarrow}$ OH+H and (twice) OH+$H_2$ $\overset{3f}{\rightarrow}$ $H_2O$+H, resulting in an overall branching reaction $3H_2$+$O_2$ $\rightarrow$ $2H_2O$+2H with a rate $\omega_B = k_{1f} C_{\mathrm{O}_2} C_{\mathrm{H}}$. On the other hand, the

main recombination path is initiated by $H+O_2+M \xrightarrow{4f} HO_2+M$, with $HO_2$ subsequently consumed through reactions $HO_2+H \xrightarrow{5f} OH+OH$, $HO_2+H \xrightarrow{6f} H_2+O_2$, and $HO_2+OH \xrightarrow{7f} H_2O+O_2$. Since $5f$ is chain-carrying, while $6f$ and $7f$ are chain-terminating, only a fraction

$$\alpha = \frac{k_{6f}C_{\mathrm{H}} + k_{7f}C_{\mathrm{OH}}}{(k_{5f} + k_{6f})C_{\mathrm{H}} + k_{7f}C_{\mathrm{OH}}} \tag{3.6}$$

of the $HO_2$ generated by $H+O_2+M \xrightarrow{4f} HO_2+M$ ends up contributing to the overall recombination reaction $2H \rightarrow H_2$, whose rate correspondingly becomes $\omega_R = \alpha k_{4f} C_{\mathrm{M}_4} C_{\mathrm{O}_2} C_{\mathrm{H}}$. Equating the effective rates of H-atom production and consumption then leads to the equation

$$k_{1f} = \alpha k_{4f} C_{\mathrm{M}_4} \tag{3.7}$$

for computation of the crossover temperature $T_c$. The presence of $\alpha$ introduces a dependence of $T_c$ on composition, additional to that present through the effective third-body concentration $C_{\mathrm{M}_4}$, which incorporates increased chaperon efficiencies for $H_2$ (2.5) and $H_2O$ (16.0), as seen in Table 3.1. In lean premixed flames and on the oxygen side of nonpremixed flames, where OH radicals are abundant, $HO_2$ predominantly reacts through $HO_2+OH \xrightarrow{7f} H_2O+O_2$, so that the recombination efficiency approaches $\alpha = 1$. By way of contrast, in rich premixed flames and on the rich side of nonpremixed flames, where H radicals dominate the radical pool, $HO_2$ removal is controlled by $HO_2+H \xrightarrow{5f} OH+OH$ and $HO_2+H \xrightarrow{6f} H_2+O_2$, resulting in an overall recombination efficiency $\alpha = k_{6f}/(k_{5f} + k_{6f})$. For illustrative purposes, values of $T_c$ evaluated with $\alpha = 1$ ($T_{c_{\mathrm{lean}}}$) and with $\alpha = k_{6f}/(k_{5f} + k_{6f})$ ($T_{c_{\mathrm{rich}}}$) are plotted in figure 3.1. As is appropriate in the reaction layer of the diluted hydrogen-oxygen diffusion flames considered here, the effective third-body concentration for step 4, $C_{\mathrm{M}_4} = (32+N)/(2+N)$, is evaluated in constructing the plot for a mixture of water vapor and nitrogen with mole fractions $2/(2+N)$ and $N/(2+N)$, corresponding to the equilibrium composition of a stoichiometric $H_2$:$O_2$:$N_2$ mixture with molar

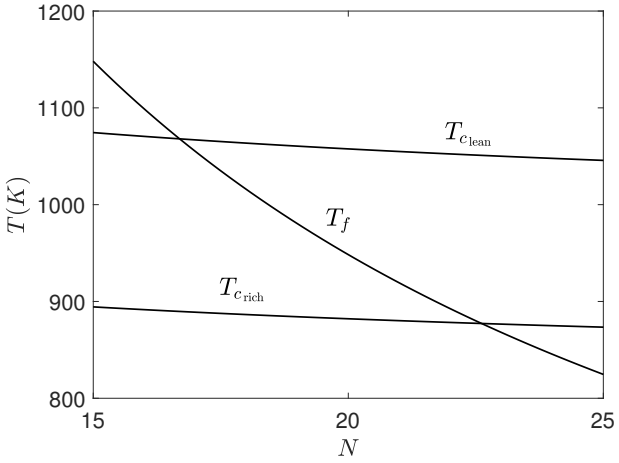


**Figure 3.1**: The variation with the dilution parameter $N$ of the crossover temperature as obtained for $p = 1$ atm from (3.7) with $\alpha = 1$ ($T_{c_{\rm lean}}$) and with $\alpha = k_{6f}/(k_{5f}+k_{6f})$ ($T_{c_{\rm rich}}$) with $C_{\rm M_4} = (32+N)/(2+N)$, and the premixed adiabatic flame temperature $T_f$ for an initial temperature of $T_o = 298$ K.

proportionality $H_2$:$O_2$:$N_2$=2:1:$N$.

As previously mentioned, near-critical flames appear under conditions such that the reaction-layer temperature lies close to the crossover temperature $T_c$, with the overall fuel-oxidation rate following closely a branching-recombination balance. For instance, in premixed combustion the condition that the adiabatic flame temperature must lie above the crossover temperature can be used to define the range of equivalence ratios in which a planar steady flame may exist for a given dilution. The computation of the corresponding lean and rich flammability limits must account for the existence of two distinct crossover temperatures in the two limits [11]. Similarly, in nonpremixed combustion a quick characterization of the reactant-feed conditions that lead to near-critical flames can be achieved by comparing $T_c$ to the peak temperature $T_p$ reached in the Burke-Schumann limit of infinitely fast reaction. In particular, a necessary condition for the existence of the diffusion flame is that $T_p > T_{c_{\rm rich}}$, whereas for $T_p$ much larger than $T_{c_{\rm lean}}$ near-critical phenomena can be expected to be of lesser importance.

## 3.4 The planar diffusion-flame structure for an infinitely fast reaction

In the Burke-Schumann limit, the flame appears as an infinitesimally thin flat surface, $y = y_f$ separating two equilibrium regions. Integrating the steady one-dimensional transport equations with boundary conditions $Y_{O_2} - Y_{O_{2_o}} = Y_{H_2} = T - T_o = 0$ as $y \to \infty$, $Y_{O_2} = Y_{H_2} - Y_{H_{2_o}} = T - T_o = 0$ as $y \to -\infty$, and $Y_{O_2} = Y_{H_2} = T - T_p = 0$ at $y = y_f$ provides the reactant and temperature profiles

$$Y_{H_2} = 0, \quad \frac{Y_{O_2}}{Y_{O_{2_o}}} = 1 - \frac{1 - \mathrm{erf}(y\sqrt{L_{O_2}/2})}{1 - \mathrm{erf}(y_f\sqrt{L_{O_2}/2})}, \quad \frac{T - T_o}{T_p - T_o} = \frac{1 - \mathrm{erf}(y/\sqrt{2})}{1 - \mathrm{erf}(y_f/\sqrt{2})} \tag{3.8}$$

for $y > y_f$ and

$$\frac{Y_{H_2}}{Y_{H_{2_o}}} = 1 - \frac{1 + \mathrm{erf}(y\sqrt{L_{H_2}/2})}{1 + \mathrm{erf}(y_f\sqrt{L_{H_2}/2})}, \quad Y_{O_2} = 0, \quad \frac{T - T_o}{T_p - T_o} = \frac{1 + \mathrm{erf}(y/\sqrt{2})}{1 + \mathrm{erf}(y_f/\sqrt{2})} \tag{3.9}$$

for $y < y_f$. The gradients on the oxidizer (superscript +) and fuel (superscript -) sides of the flame sheet are related by the jump conditions

$$\frac{(Y'_{O_2})^+}{32L_{O_2}} = -\frac{(Y'_{H_2})^-}{4L_{H_2}} = \frac{(T')^+ - (T')^-}{36(h^o_{H_2O}/c_p)} \tag{3.10}$$

obtained by integration of chemistry-free linear combinations of the steady one-dimensional conservation equations, with $h^o_{H_2O} = -13.44 \times 10^6$ J/kg denoting the enthalpy of formation of water vapor. The first equation in (3.10), stating that the reactants reach the flame sheet by diffusion with fluxes in stoichiometric proportions, can be evaluated with use made of (3.8) and (3.9) to give

$$\frac{1 - \mathrm{erf}(y_f\sqrt{L_{O_2}/2})}{1 + \mathrm{erf}(y_f\sqrt{L_{H_2}/2})} = \sqrt{\frac{L_{H_2}}{L_{O_2}}}\frac{Z_s}{1 - Z_s}\exp[(L_{H_2} - L_{O_2})y_f^2/2], \tag{3.11}$$

as an implicit equation for the flame location $y_f$. A similar evaluation of the second equation in (3.10), with use made of (3.1), yields

$$\frac{T_p - T_o}{T_f - T_o} = \frac{\exp[(1 - L_{\mathrm{H}_2}) y_f^2/2]}{2\sqrt{L_{\mathrm{H}_2}} Z_s} \frac{1 - \mathrm{erf}^2(y_f/\sqrt{2})}{1 + \mathrm{erf}(y_f \sqrt{L_{\mathrm{H}_2}/2})} \tag{3.12}$$

for the peak temperature $T_p$, where

$$T_f = T_o + \frac{9}{9 + 7N} \frac{h^o_{\mathrm{H_2O}}}{c_p}, \tag{3.13}$$

is the stoichiometric adiabatic temperature, whose variation with $N$ is plotted in Fig. 3.1.

As can be seen from (3.11), in the equidiffusional case $L_{\mathrm{H}_2} = L_{\mathrm{O}_2} = 1$ the flame location is given by $\mathrm{erf}(y_f/\sqrt{2}) = 1 - 2Z_s$, which can be used in (3.12) to yield the familiar result $T_p = T_f$, independent of $Z_s$. Numerical evaluation of (3.11) and (3.12) is in general needed to compute $y_f$ and $T_p$ for the realistic values $L_{\mathrm{H}_2} = 0.29$ and $L_{\mathrm{O}_2} = 1.10$, with results shown in Fig. 3.2. From this plot it can be seen that the temperature increase associated with differential-diffusion effects is more pronounced for intermediate values of $Z_s$, skewed towards larger values, enabling the existence of planar diffusion flames with levels of feed-stream dilution well above the value $N = 23$ predicted from the simple adiabatic-flame criterion $T_f = T_{c_{\mathrm{rich}}}$. Additional differential-diffusion effects induced by curvature are to be investigated below in the following two-dimensional computations.

## 3.5 Extinction strain rates of planar diffusion flames

In general, in studies focusing on edge-flame propagation, one may, logically speaking, use the laminar planar premixed flame speed as the characteristic velocity scale for the edge-flame speed, provided that the effects of thermal expansion are ignored as hsa been done in chapter 2, since the classical tri-brachial structure approaches the planar flame as the strain rate becomes

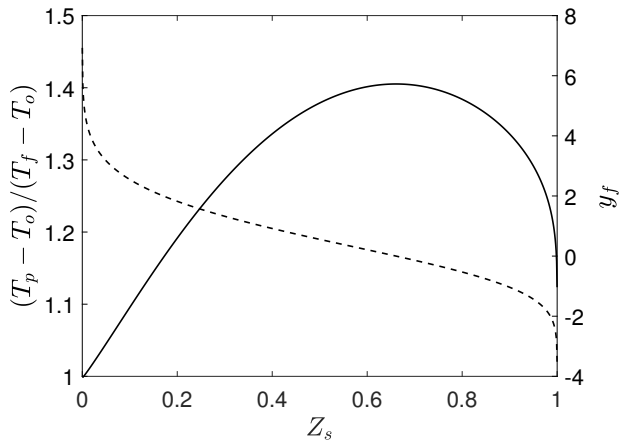


**Figure 3.2**: The variation with $Z_s$ of the peak Burke-Schumann temperature (solid curve) and the reaction-sheet loctaion (dashed curve) of a counterflow diffusion flame as obtained from (3.11) and (3.12) with $L_{\mathrm{H}_2} = 0.29$ with $L_{\mathrm{O}_2} = 1.10$.

small compared with the extinction strain rate of the one-dimensional diffusion flame. Although this is also true for the current problem, the strain rate that is needed to achieve the triple flame is so small that it can never be realized in actual experiments; in the slot-jet apparatus, heat loss to the jet walls and other body-force effects, not considered in our formulation, will prevent the occurrence of these low-strain triple flames. Moreover, since interesting flame dynamics occurs near the extinction point for the near-critical limits, it is natural to use the one-dimensional extinction strain rate as the representative inverse time scale, as has been done previously [4]; that is, instead of normalizing predictions in terms of a characteristic velocity, it becomes better to normalize them in terms of a characteristic strain rate.

The extinction values of the strain rate are obtained from the maximum value of the product $\rho A$ for which equations (3.3) and (3.4), after neglecting $t$ and $x$ derivatives, have a solution. These values, denoted by $(\rho A)_{ext}$ and calculated as functions of $Z_s$ for three different values of $N$, are shown in figure 3.3. Measuring the species-production rate $\dot{m}_i$, and the heat-generation rate $-\sum_i h_i^o \dot{m}_i$, in units of $(\rho A)_{ext}$ and $c_p T_o (\rho A)_{ext}$, the only parameter that appears in equations (3.3) and (3.4) becomes $\varepsilon = (\rho A)/(\rho A)_{ext} = A/A_{ext}$, the non-dimensional strain rate. In this manner, it is unnecessary to select any particular value for $\rho$ in presenting results of

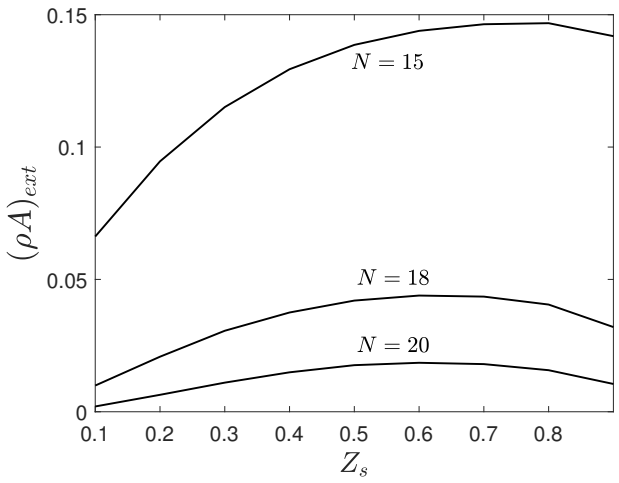


**Figure 3.3**: The extinction value of the product $\rho A$ for the diffusion flame as a function of the mixture fraction $Z_s$ for three different values of $N$.

computations.

## 3.6 Computational procedures

Equations (3.3) and (3.4) were integrated numerically, subject to the previously stated boundary conditions, marching forward in time. The numerical method is based on a code developed for transient combustion applications [14]. Integrations were performed for different selections of initial conditions, including a single hot spot or multiple hot spots (actually hot tubes because of the absence of a $z$ dependence[1]), or a hot layer either extending to all $x$ or only from a chosen value of $x$ to the boundary of the domain, at a selected value of $y$. The evolution of the resulting structures with time was then computed with the strain-rate parameter $\varepsilon$ held fixed, or else with that parameter varied slowly with time, to see whether hysteresis may occur as the system moves from one regime to another. In addition, to explore the range of possible steady solutions, the differential equations with the time-derivative terms removed were integrated in $-1 \leq x/x_{max} \leq 1$ with the independent variable $x$ replaced by $x/x_{max}$, so that $x_{max}$ appears as a

[1]Flame tubes (which are not hollow) might instead be termed strips, strings, or rods, etc., but the selected term "tube" is most prevalent in the literature [6].

parameter in the equations, and the range of values of $x_{max}$ for which such solutions exist was determined, the resulting flame configuration then becoming periodic in $x$ the length of the period being $2x_{max}$.

All of these computations were performed for the representative near-limit dilution value $N = 18$, for which experimental results are available, since that is sufficient for exhibiting the full range of results, but the stoichiometric mixture fraction was varied over the complete range possible for this value of $N\,(0.007\,\text{to}\,0.941)$ because the different regimes that are encountered depend strongly on the value of this mixture-fraction parameter.

## 3.7 Flame configurations and structures

The flames that develop from different initial conditions differ for low and high values of $Z_s$. Representative computational results for low $Z_s$, when initially a flame extends over a half-plane, are those found at $Z_s = 0.4$. Figure 3.4 shows the advancing (a) and retreating (b) edge flames encountered at lower strain rates ($\varepsilon = 0.45$) and higher strain rates ($\varepsilon = 0.85$), respectively, at that value of the stoichiometric mixture fraction. The OH mass fraction is selected as a representative measure of the flame structure. The region over which OH builds up is known to be broader on the oxygen side of the diffusion flame than on the hydrogen side for chemical-kinetic reasons, and that this is true can be inferred from the shading in the figure, especially at the flame edge, where downward bending of the initial buildup is discernible. At this value of $Z_s$, ignition always fails when $\varepsilon > 1$, extinction occurring irrespective of initial conditions.

At higher values of $Z_s$, however, the same half-plane initial condition results in continued combustion for some values of $\varepsilon > 1$, as can be seen for $Z_s = 0.9$ in Fig. 3.5. This figure shows that, at $\varepsilon = 1.25$, most of the half-plane extinguishes, but its end remains burning and develops into a flame tube, which subsequently splits in two, forming two flame tubes which, in turn, split again, finally leading to the array of tubes seen in the last panel of Fig. 3.5(a). This splitting

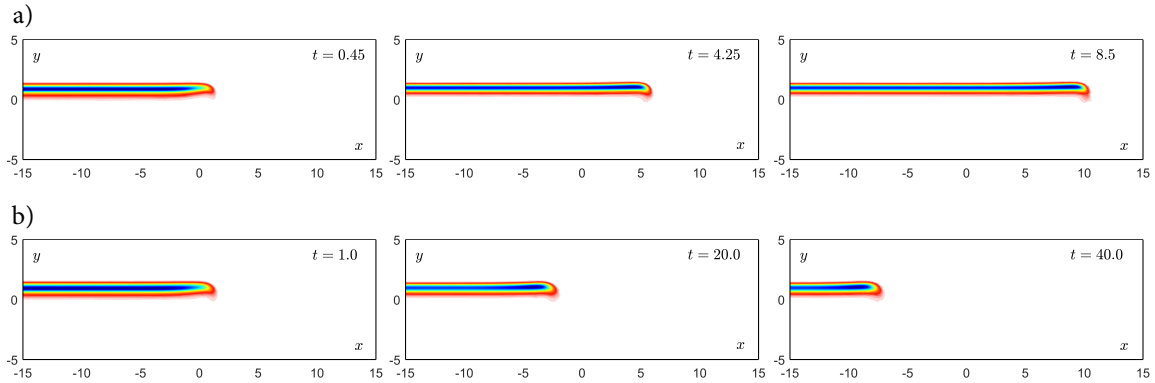


**Figure 3.4**: Snapshots showing the evolution of the solution for $Z_s = 0.4$ with $\varepsilon = 0.45$ (a) and $\varepsilon = 0.85$ (b) when the integration is started with the flame extending only over a half-plane; flame shapes are visualized by color coding, red to blue with increasing computed OH mass fractions.

occurs because the relatively high chemical activity at the ends depletes the fuel concentration in the center, so that extinction occurs there. At the higher strain rate, $\varepsilon = 2.25$, however, the single flame tube formed by flame-sheet extinguishment fails to bifurcate and instead remains isolated, but nevertheless active, as seen in Fig. 3.5(b). At this value of $Z_s$, combustion can be initiated for strain rates all the way up to $\varepsilon \simeq 3.5$, the sequence with increasing $\varepsilon$ being similar to that in Fig. 3.5(b), but with the final flame tube shrinking and becoming more round as $\varepsilon$ increases.

Flame-tube dynamics and final flame-tube configurations can be sensitive to the initial conditions, especially at higher stoichiometric mixture fractions. Figure 3.6 shows the evolution predicted for $Z_s = 0.9$, with ignition produced by two or three hot spots, at four different values of $\varepsilon$. At the lowest value shown, $\varepsilon = 0.45$, the complete planar diffusion flame is the only stable configuration, and the flame strips generated from the two hot spots are seen in Fig. 3.6(a) to merge and to form that planar flame. At the next higher value in the figure, $\varepsilon = 0.70$, the edges of the strips are unable to merge as a result of the opposing edges attracting hydrogen through preferential diffusion to a very large extent, thereby producing an insufficiently high hydrogen concentration in the region between them for combustion to occur there. Flame-free gaps thus persist between the burning regions, the widths of the gaps being determined by the strength of

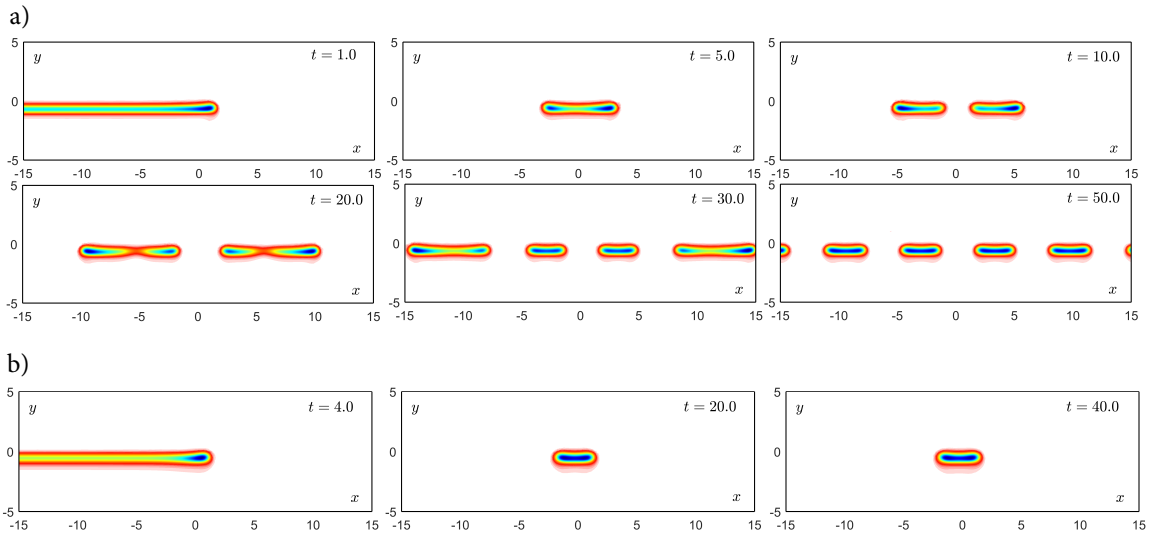


**Figure 3.5**: Snapshots showing the evolution of the solution for $Z_s = 0.9$ with $\varepsilon = 1.25$ (a) and $\varepsilon = 2.25$ (b) when the integration is started with the flame extending only over a half-plane; flame shapes are visualized by color coding, red to blue with increasing computed OH mass fractions.

the preferential diffusion. That it is the gap width that is determined by the diffusion processes occurring may be inferred by comparing the sequences (b) and (c), the latter at the same condition but with three rather than two hot spots; the configuration evolves until the gaps that are present achieve the same width. This reactant-depletion effect of flame edges at low Lewis numbers does not appear to have been recognized clearly in the previously cited publications.

The last two sequences in Fig. 3.6 may be compared with Fig. 3.5 to see the differences between the evolutions that follow half-plane and multiple-hot-spot initial conditions. At $\varepsilon = 1.25$, instead of half-plane extinguishment, the hot spots grow into flame tubes, which subsequently continue to split, in the same manner as was observed for the tubes that resulted from half-plane ignition. The final sequence shows that, while a single flame tube was generated by half-plane ignition, two result from ignition by two hot spots. This is a requirement of the aforementioned inability of edge flames to merge above a critical value of $\varepsilon$; it would be impossible for flame strips generated by two different hot spots to merge into a single flame tube. In the sequence (e) in the figure, the hot spots are far enough apart that they do not interact but instead independently

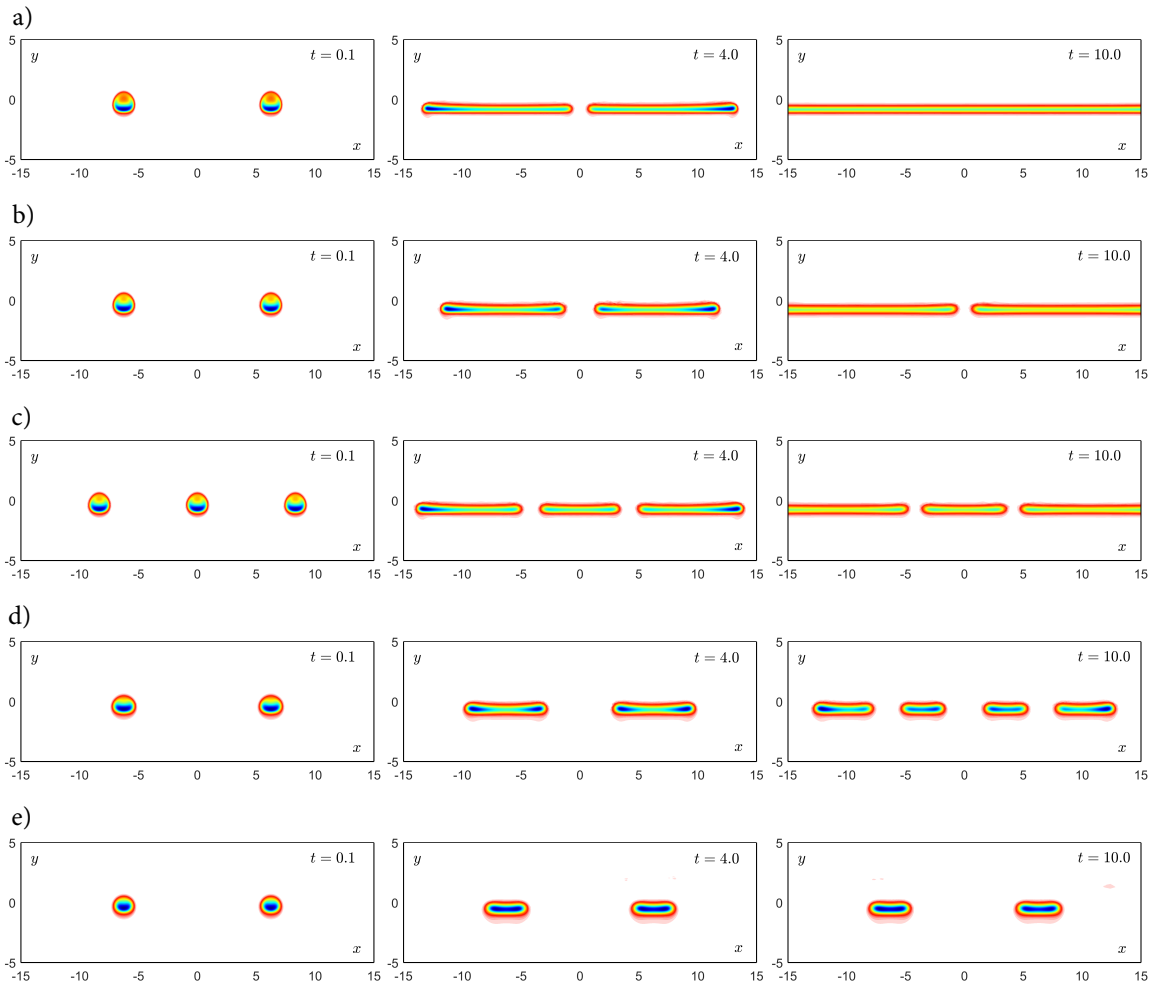


**Figure 3.6**: Snapshots showing the evolution of the solution for $Z_s = 0.9$ with $\varepsilon = 0.45$ (a), $\varepsilon = 0.70$ (b and c), $\varepsilon = 1.25$ (d), and $\varepsilon = 2.25$ (e) when the integration is started with two or three hot spots; flame shapes are visualized by color coding, red to blue with increasing computed OH mass fractions.

develop into stable flame tubes; the number of flame tubes, in general, would be the same as the number of initial hot spots under these conditions.

These figures reveal various additional aspects of structures of the flame tubes. They appear to exhibit a continuous variety of shapes and structures. As extinction conditions are approached, they become almost entirely round strings, with the maximum reaction rate located at the center. Away from extinction, as conditions begin to admit more robust burning, they begin to flatten and develop reaction-rate peaks near their ends, those peaks having moved off from the central rate maximum. These aspects are reflected in the figures by the higher OH mass fractions near the ends. With increasing robustness, the tubes widen more, finally elongating into broad flame strips, before reaching a boundary at which they are transformed into edge flames that evolve to steady configurations controlled by the flame-free gaps between them. The peak temperatures in the flame tubes, which tend to exceed those in the strips, will be indicated below to decrease as conditions evolve towards boundaries at which flame extinction occurs. Flame-tube structures thus can be quite varied, depending on the strain rate and the stoichiometric mixture fraction. The broad range of flame-tube structures that are possible is remarkable.

## 3.8 Additional flame-structure aspects, and the hysteresis phenomenon

Figure 3.7 summarized additional aspects of possible flame structures and configurations by showing the computed variation of the peak flame temperature with the strain rate at $Z_s = 0.9$, along with representative flame structures found in different regimes, for stable, steady-state combustion. This figure documents the existence of a much wider range of steady, stable flame configurations than might initially be anticipated. They arise through the strong effects of preferential diffusion of hydrogen as the stoichiometric mixture fraction approaches unity at high dilution.

Beginning at low strain rates at the far left, the decrease in the peak temperature with increasing strain rate up to $\varepsilon = 1$, seen in the square symbols, is associated with the infinite planar diffusion-flame structure illustrated by the color-coded image in the lower left-hand part of the figure. This is consistent with the well-known decrease of flame temperature with increasing strain rate along the upper branch of the familiar S-shape curve of nonpremixed combustion [15]. When $\varepsilon$ passes through unity, the planar flame might be expected to extinguish, resulting in only cold-flow mixing, but instead the planar flame was found to bifurcate, as is indicated in the figure by a vertical dashed line, into regularly spaced flame tubes, with structures similar to those which are illustrated in the last panel of sequence (a) in Fig. 3.5. Clearly, therefore, for values of $\varepsilon$ somewhat above unity, a stable steady combustion solution continues to exist, namely, a multiple-flame-tube solution. As $\varepsilon$ increases further, the flame tubes become smaller and rounder, but, if instead, $\varepsilon$ is decreased after the bifurcation, stable steady multiple-tube solutions are found to continue to exist almost until $\varepsilon = 0.6$, at which there is a discontinuous jump to the planar solution, indicated by another vertical dashed line, the depletion of fuel in the gaps between the end preventing merging of the flames from occurring until the strain rate is decreased to the value at the left-most vertical dashed line There thus is a region of hysteresis, the planar flames being accessible only by increasing $\varepsilon$ and the multiple flame tubes accessible only by decreasing $\varepsilon$ in the region between the two vertical lines.

Some time-dependent solutions just before $\varepsilon$ reached unity showed the planar flame to be developing slight striations, as if it were going to break up into flame tubes, implying that the planar flame actually may become unstable to two-dimensional disturbances slightly prior to reaching planar extinction conditions. The corresponding difference in $\varepsilon$, however, is so small that this effect, if it exists, is negligible. This finding, pertaining to hydrogen-oxygen chemistry, seems to be in agreement with previous diffusion-flame stability results corresponding to model chemistry [7, 8], for which the stability threshold is extremely close to the turning point of the S-shape curve. The principal conclusion to be extracted from these considerations is that the

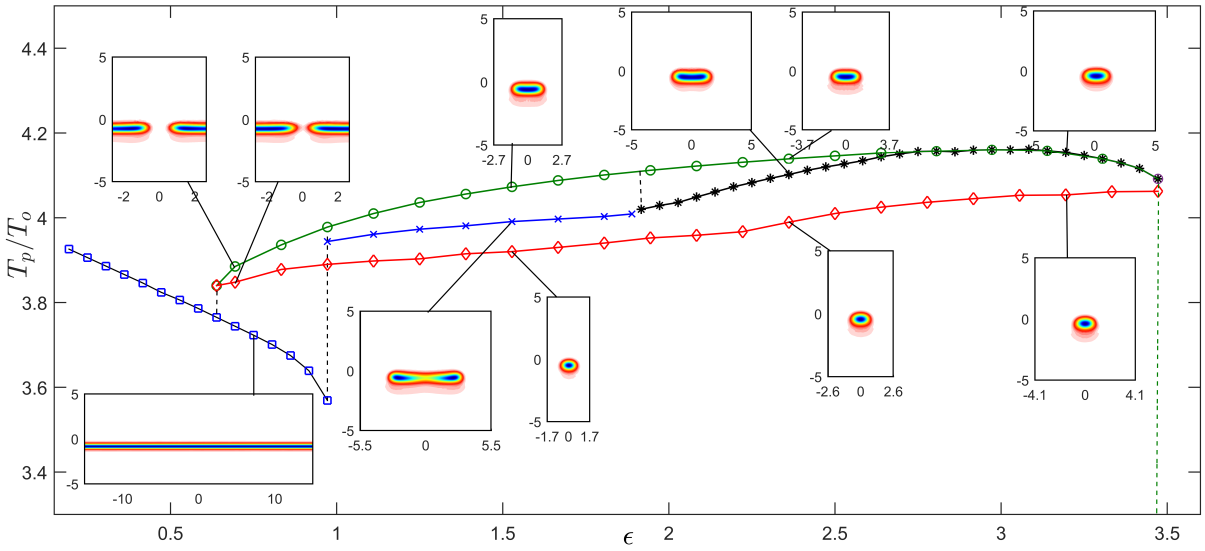


**Figure 3.7**: Peak temperature as a function of $\varepsilon$ for $Z_s = 0.9$, with resulting sample flame shapes visualized by color coding, red to blue with increasing computed OH mass fractions.

transition from the planar flame to the flame tubes for steady-state conditions is abrupt, resulting in a discontinuous increase of the peak temperature, indicated by the vertical dashed line in the figure.

To understand the rest of the extensive information in this figure it is best to begin at the opposite (right-hand) side. The black curve, marked by asterisk points that ends near $\varepsilon = 3.5$, pertains to a single flame tube in an infinite $x$ domain. This single-tube solution is the only one that exists in the limit as this maximum strain rate is approached, there being no steady flame-structure solutions of any kind for values of $\varepsilon$ greater than that marked by the right-hand vertical dashed line; the true extinction strain rate at $Z_s = 0.9$ thus is about 3.5 times that of the planar flame. The single tube is almost perfectly round at the limit but elongates as $\varepsilon$ is decreased, as is indicated by the flame-structure inset in the upper right-hand corner. The single-tube peak temperature increases as the residence time available for reaction increases with decreasing $\varepsilon$, but it reaches a maximum and thereafter decreases as the temperature reduction associated with tube broadening to approach a flame strip begins to become dominant. Eventually, near $\varepsilon = 1.9$, the single-tube solution ceases to exist; splitting into a multiple-tube solution, by the mechanism

described in connection with part (a) of Fig. 3.5, occurs at the short vertical dashed line. Splitting through gradual changes of $\varepsilon$ is possible only between the two central-most dashed lines, with the sheet splitting on the left and the single tube splitting on the right.

The computations treating $x_{max}$ as a parameter show further that, near the maximum value of $\varepsilon$, steady stable solutions exist for uniform arrays of equally spaced multiple flame tubes with spacings ranging continuously from infinity to a minimum value. The inset in the lower right-hand corner of the figure is shown to compare the flame-tube structure at the minimum separation pacing with that at infinite spacing in the upper corner, for the same value of $\varepsilon = 3.2$. That comparison shows that the neighbors have reduced the broadening of the tube by depriving it from the fuel it would need to expand; its local atmosphere effectively is more dilute. A result is that its peak temperature also is lower. Such multiple-tube solutions with a continuous range of spacings exhibiting a minimum value continue to exist with decreasing $\varepsilon$, all the way down to the farthest left vertical dashed line, where flame merging finally becomes possible, and the abrupt transition to the planar flame sheet occurs. The peak flame-tube temperature at this minimum separation decreases practically linearly with decreasing $\varepsilon$, the lower strain rate allowing the round tube to survive to a lower peak temperature by reducing the rate of heat loss from the hot tube. To provide additional information about gap widths, the edges of the lower-right inset are selected to be lines of symmetry in the solution, so that its width is the distance $2x_{max}$ between adjacent tubes; this same convention applies to all but one of the remaining insets.

With decreasing $\varepsilon$, beginning around $\varepsilon = 2.7$, multiple-tube solutions exhibit peak temperatures above that of the single tube. This occurs when the shape-change effect begins to be dominant. The broadening of the single tube has reduced its peak temperature, so, by decreasing the broadening, adjacent tubes achieve higher peak temperatures than the single tube. But, as the spacing decreases further, the influence of adjacent tubes depriving the tube from its fuel begins to dominate, and the tube peak temperature then decreases, eventually below that of the single tube. This non-monotonicity is a complicating factor. The associated flame-tube shapes are shown by

three insets at a value of $\varepsilon$ somewhat less than 2.5; the single tube is the broadest and the tube with the minimum spacing is the smallest and roundest, but a tube with an intermediate spacing and shape is the hottest. The upper curve in the figure, marked by the round points, shows how this maximum value of the peak temperature decreases with decreasing $\varepsilon$ all the way down to the bifurcation at the left-most vertical dashed line. Computations with $\varepsilon$ increasing gradually typically show that, at the bifurcation that occurs as $\varepsilon$ passes through unity, the solution jumps to a regular multi-tube array with a spacing a little less than that having the maximum peak temperature and evolves thereafter with continuously decreasing spacing, exhibiting a peak temperature that increases to a maximum and then decreases, crossing the single-tube peak-temperature curve and eventually reaching the minimum-spacing limit, extinguishing there at a value of $\varepsilon$ well below 3.5.

Since the single-tube solution is the solution in the limit of infinite wave length of the periodic multiple-tube solutions, its vanishing when $\varepsilon$ is decreased below about 1.9 means that, at that value of $\varepsilon$, a maximum flame-tube separation distance must begin to exist, in addition to the minimum distance. The curve marked by x symbols, between the two central vertical dashed lines, ending at the end of the single-tube curve, gives the peak temperatures of steady, stable tubes with this maximum separation. The three flame-structure insets at $\varepsilon = 1.5$ show how the steady-state shape changes with tube spacing in that region. At the minimum spacing the tubes are practically round, as the spacing increases and reaches that needed to achieve the highest possible peak temperature there, the tube becomes more elongated, and, as the spacing reaches its maximum possible value, the tubes are extremely elongated and are about to split, as they can and do in this region. The entire possible range of steady flame-tube shapes thus is accessible in this region, the variations being achieved by varying the spacing in the regular array.

As $\varepsilon$ is further decreased into the region of hysteresis, the maximum limit on the separation distance suddenly disappears, splitting no longer being possible, so the elongation becomes unbounded, with edges expanding until they encounter another edge. Since merging of edges,

prevented by fuel depletion in the gap, is not possible until transition to the infinite planar flame sets in at the left-most vertical dashed line, the flame-free gap reaches a limiting width, and it is the gap width that controls the peak temperature (which occurs near the edge of the flame strip). The extent of fuel depletion in the gap will reach a maximum at the minimum separation distance because the depletion is enhanced by fuel diffusion to edges of adjacent gaps, so that, the closer gaps are to each other, the greater will be the depletion. The left-most inset for the minimum separation distance, shown in a domain of width equal to the separation distance, is centered on the gap rather than on the flame because it is the gap that is controlling in this region. As the separation distance increases, the associated decrease in the fuel-depletion influences of adjacent gaps allows the gap width to increase. The maximum extent of increase of gap size, which would correspond to the maximum value of the peak temperature, would occur in the limit of infinite separation distance. The flame-structure inset in the figure for the maximum peak flame temperature in this region shows this maximum gap width in the same scale as that employed for the minimum separation distance, so that the flames at the sides of this inset would extend outward for very large distances.

As the strain rate decreases past $\varepsilon = 1$ and the maximum separation distance disappears, the maximum value of the peak temperature remains continuous, but, instead of occurring at a definite finite value of the separation distance, it occurs (and remains from there on) at infinite separation. Actually, as the separation distance increases, it soon becomes large enough that further increases have negligible influences on the peak temperature, so it is practically independent of separation beyond the limiting separation that exhibits the maximum peak temperature for $\varepsilon > 1$. More dramatic is the discontinuous flame shape for the minimum separation distance as the strain rate decreases past $\varepsilon = 1$; because of the onset of the absence of any possibility for splitting, instead of the nearly round strings seen in the other insets, this limiting flame tube becomes a fairly wide strip, much like that which can be inferred from the inset at the far left. Discontinuities of flame shapes also occur at this value of $\varepsilon$ for separation distances greater than

the minimum, further emphasizing that the importance of $\varepsilon = 1$ extends beyond the fact that the planar flame extinguishes there. A further relevant observation is that, in this hysteresis region, there exist infinitely many more steady, stable“flame-tube" configurations than exist at higher strain rates. In particular, arrays need not be regular; any initial arrangement of ignition spots or flame-sheet gaps will experience edge propagation to an ultimate gap size dictated by locations of adjacent gaps. In irregular arrays, the maximum peak flame temperature will be controlled by the pair of adjacent gaps having the greatest separation distance between them. The range of values over which the peak temperature varies as the gap size is changed decreases as $\varepsilon$ decreases, approaching a single value just before bifurcation, so that the jump in the peak temperature is the same, irrespective of which of the infinite number of possible stable configurations the bifurcation originates from. The bifurcation of the flame sheet at $\varepsilon = 1$, on the other hand, could occur only to a regular array of structures, but with any one of a continuously infinite number of spacings, between a maximum and minimum value, depending on the manner in which $\varepsilon$ is increased; near-maximum spacings would be favored because their higher peak temperatures make them more robust.

## 3.9 The regime diagram

Computations were made for four different types of initial conditions, namely, combustion extending over a full plane, combustion extending only over a half plane, multiple isolated hot spots, as could be provided by multiple sparks, and a single isolated hot spot. Depending on the values of $Z_s$ and $\varepsilon$, the combustion ultimately either quenched or evolved into one of four different types of configurations, namely, a full burning diffusion-flame plane, a burning half-plane, corresponding to either an advancing or retreating edge flame (in regions divided by a curve along which the edge flame remains stationary), multiple flame tubes that were either moving or stationary, or a single stationary flame tube. This variety of outcomes served to divide the $Z_s$ -

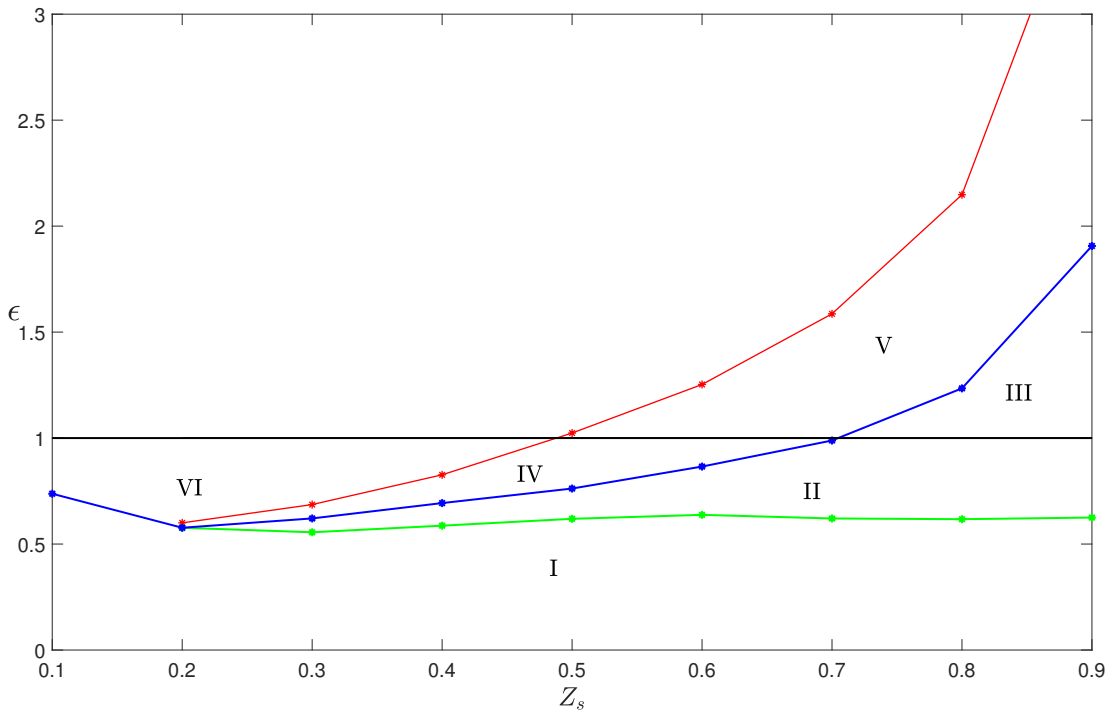


**Figure 3.8**: The regime diagram

$\varepsilon$ plane into seven different regions, one without combustion at the end of the computation and six exhibiting continued combustion having different combinations of possible ultimate burning behaviors, with the boundaries between them separating the different flame configurations. This regime diagram is shown in Fig. 3.8, where the six combustion regimes are labeled by Roman numerals.

The simplest boundary in the diagram is the horizontal line $\varepsilon = 1$, below which full planar steady-state diffusion-flame sheets exist, and above which they do not. The next most significant boundary is composed of three curves in the diagram, namely, the boundary between regions I and VI, followed by the boundary between regions VI and IV, followed by the upper boundary of region V; flame tubes cannot exist above this boundary, where the only burning solutions are full stable planar diffusion flames or retreating edge flames, but they can exist below the part of it that begins at the left-most end of region IV. It is noteworthy that, for large enough values of $Z_s$, this boundary extends combustion into regions where all planar flames would extinguish,

thereby widening the range of combustion through effects of preferential diffusion. A third notable boundary sequence is that between regions IV and II, followed by the boundary between regions V and III; below that boundary edge flames are advancing (when they exist) and flame tubes are splitting and advancing, while above it edge flames are retreating and flame tubes are stationary, so that, for example, stationary edge flames exist only along this boundary (the lower part of it). The last significant boundary sequence is that between regions I and VI, followed by that between regions I and II; edges of flame sheets or tubes can merge below this boundary, but merging cannot occur above it, the strain rate and preferential diffusion being too large to permit two edges to combine, even though the planar flame that could develop after merging may be stable.

It is of interest to enumerate the flame configurations than can exist in each of the six different combustion regimes identified in the $Z_s$- $\varepsilon$ plane, labeled by the Roman numerals in Fig. 3.8. Region I, which is approximately given by the condition $\varepsilon < 1/2$, is where a unique, stable, reacting equilibrium solution covering a complete plane eventually develops from any ignition event, irrespective of its type. A hot-spot ignition, or a semi-infinite hot-layer ignition (not extending to all values of $x$) leads to edge-flame propagation, leaving the diffusion flame behind as the steady-state solution. Multiple hot spots also result in edge propagation with the edges of adjacent hot spots merging together, forming a steady diffusion flame.

In region II, both infinite, planar, diffusion-flame and broken-flame solution are allowable. In this region, a semi-infinite hot-layer ignition results in an advancing edge flame that eventually reaches the full, planar diffusion-flame solution, as does a single hot-spot ignition, but with more than one hot-spot ignition, perhaps surprisingly, this does not occur because the edges of the hot spots are unable to merge. With two hot spots, the result, instead, is two edge flames facing each other and extending to the boundary of the numerical domain, and with more than two hot spots the final configuration is an array of three or more complete elongated flame strips, the outermost two extending to a domain boundary. These developments occur basically because, in this regime,

flame edges are unable to merge as a result of the opposing edges attracting hydrogen through preferential diffusion to a very large extent, thereby producing an insufficiently high hydrogen concentration in the region between them for combustion to occur there. Flame-free gaps thus persist between the flame tubes, the widths of the gaps being determined by the strength of the preferential diffusion. With multiple hot-spot ignitions, at separation distances large enough that adjacent hot spots do not interact, in this region flame tubes (or edge flames) are generated from each ignition spot and remain stable, without extinguishing. The line between region I and II is the smallest value of $\varepsilon$ for which flame tubes can be realized as a final configuration.

By definition, in region III, steady, infinite, planar diffusion flames do not exist, since this region is bounded from below by the condition $\varepsilon = 1$. In this region both single hot-spot and semi-infinite hot-layer ignitions lead to oscillatory propagation of leading flame edges, behind which flame sheets break and leave flame tubes behind; sheets must break, since edge flames also cannot exist here. The oscillation develops because the edge advancement speeds up after breaking, then slows as the next break prepares to occur. As $Z_s$ increases, the number of flame tubes for a given length increases in region III. Flame tubes can elongate and split in this region as a consequence of the advancing of their edges in opposite directions, eventually leaving insufficient fuel adjacent to their mid-sections to maintain combustion there. Multiple-point ignitions in this region exhibit the flame-free-gap phenomena described for region II, for the same reason. Flame-tube dynamics in this region thus appears to be more complex than in any other region.

The lower limit of region IV is the boundary at which an edge flame stops propagating and starts retreating as $\varepsilon$ is increased. It also is the boundary curve at which the leading flame tube, generated by splitting of a flame sheet having an advancing flame edge (initiated by a central ignition spot) stops propagating, so that the flame tubes become stationary in region IV. Isolated flame tubes, in addition to flame-tube arrays, also can be observed in this region, which thus permits a number of different steady flame-tube configurations, in addition to the planar diffusion flame.

Region V has the same characteristics as region IV, except that in this region there are no retreating edge flames and no planar diffusion flames, there being only flame tubes, which ultimately remain stationary in this region. In addition, the continued existence of single isolated flame tubes is possible only in regions IV and V. It is perhaps curious that, while flame tubes can exist only in regions II, III, IV, and V, those in region II are stable only because flame-free gaps are stable there, unlike those in the other three of these regions.

There are no flame tubes in region VI; the only steady solution there is the infinite planar diffusion flame. The curve that separates region I and VI is associated purely with the distinction between advancing and retreating edge flames. Thus, there exists no flame-tube dynamics for small $Z_s$. Flame-tube dynamical phenomena are confined to the range $\varepsilon < 1$ if $Z_s < 1/2$; they are then present only in a narrow band at these low stoichiometric mixture fractions. On the contrary, for $Z_s > 1/2$, flame-tube dynamics can be realized for both $\varepsilon < 1$ and $\varepsilon > 1$ with their region of existence growing larger as the value of $Z_s$ is increased.

The range of conditions investigated numerically in Fig. 3.8 corresponds to the experimental results of flame propagation reported in Fig. 5b of [4]. Partial correspondence of regimes and parametric boundaries between both diagrams can be found for intermediate values of $\varepsilon$, for which the experimental flow remains laminar with negligible heat losses. Thus, the solutions found in regions I, III, V, and VI in Fig. 3.8 correspond, respectively, to modes I (advancing continuous flames), III (advancing broken flames), IV (stationary broken flames), and II (retreating continuous flames) in Fig. 5b of [4]. More work is needed to delineate a complete correspondence between the numerical and experimental diagrams. Specifically, experimental characterization of regions IV and II in Fig. 3.8, not identified in the previous flame-propagation experiments, would require consideration of spark-ignition events for intermediate values of $Z_s$ and moderate strain rates in the range $0 < 1 - \varepsilon \ll 1$. On the other hand, modification of the energy equation (3.4) by addition of a heat-loss term would be needed to model flame extinction by heat losses to the combustor wall, found in [4] for sufficiently small values of $\varepsilon \ll 1$.

It is also of interest to relate the present results to those of previous edge-flame modeling efforts pertaining to reactants with equal diffusivity undergoing an irreversible reaction [6, 8]. In these previous works, the reactants Lewis number $Le < 1$ and the Damköhler number $\delta$ (the ratio of the characteristic reaction rate to the strain rate) were varied to investigate the conditions for existence of different edge-flame phenomena, including advancing and retreating fronts, as well as diffusion-flame breakup into multiple tubes, or isolated flame tubes. The resulting map of solutions, plotted in the $Le$-$\delta$ plane in Fig. 4 of [6] (or in Fig. 6 of [8]), is fundamentally equivalent to the $Z_s$-$\varepsilon$ regime diagram shown in Fig. 3.8, the only exception being region II (non-merging tubes) in Fig. 3.8, which was not identified in the previous work. To relate the parametric maps it is necessary to take into account the fact that increasing values of $\varepsilon$ in Fig. 3.8 correspond to decreasing values of the Damköhler number $\delta$ in Fig. 4 of [6] as well as the fact that the effective Lewis number of $H_2$-$O_2$-$N_2$ mixtures decreases with increasing $Z_s$ (because the deficient reactant switches from oxygen to hydrogen as $Z_s$ increases from $Z_s \ll 1$ to $1 - Z_s \ll 1$). With that in mind, it is easy to see that the lines $\delta = \delta_q$, $\delta = \delta_o$, and $\delta = \delta_e$ in [6] correspond to the black, red, and blue boundaries in Fig. 3.8.

## 3.10 Conclusions

Near-limit $H_2$-$O_2$-$N_2$ combustion in counterflow mixing layers, studied numerically here, exhibits a noteworthy variety of different types of flame dynamics, which can be categorized in a bifurcation diagram. In a number of regimes in the diagram, the resulting flame structures and configurations are not unique; they depend very much on the initial conditions and therefore on the way in which any particular corresponding experiment would be carried out. Even though the thermo-diffusive approximation is invoked in the analysis, the flame shapes derived are in qualitative agreement with those seen in experiments [4], although further testing against future experiments certainly would be worthwhile.

In a classification based on the extent and connectivity of reaction regions, planar two-dimensional counterflows of hydrogen highly diluted by nitrogen, against oxygen highly diluted by nitrogen, possess an infinite number of different steady-state, stable, concentration-field configurations. One class involves simple non-reactive mixing. Another has a reaction plane of infinite extent, located at the stoichiometric position, oriented perpendicular to the direction of injection. A third is an edge flame occupying a half plane perpendicular to the direction of injection, at that same stoichiometric position. A fourth is a single flame tube, with its axis in the plane of the flow, oriented parallel to the outflow direction, located at a stoichiometric position. Beyond that, there are configurations with equally spaced flame arrays for sufficiently high stoichiometric mixture fractions, having a continuum of possible spacings in the array. This continuum of spacings exhibits a minimum possible spacing over a wide range of strain rates, from a minimum strain rate, below which the only stable steady flame is the planar in-tact flame sheet, to the maximum possible strain rate above which combustion cannot occur, as well as a maximum possible spacing, over a smaller strain-rate range, from the strain rate at which the infinite planar flame sheet quenches to the strain rate below which a single, isolated flame tube cannot exist. Also, for sufficiently high stoichiometric mixture fractions, there is a range at smaller strain rates, exhibiting hysteresis, over which two types of stable steady-state solutions exist, one involving a single infinite planar flame and the other multiple flame strips in arrays that need not be regular with a range of possible inter-strip spacings, these gap sizes controlling the peak flame temperature, the strip widths being irrelevant.

The flame tubes exhibit a continuum of shapes and structures. Above the strain rate at which the infinite planar flame extinguishes, as extinction conditions are approached they become practically entirely round strings, with the maximum reaction rate located at the center. Away from extinction, as conditions begin to admit more robust burning, they flatten and develop reaction-rate peaks near their ends, elongating into fairly broad flame strips with flame-free gaps between them, before reaching a boundary at which they are transformed into edge flames, where

it becomes more relevant to focus on the sizes of the gaps between the edges than on the flame sizes. The peak temperatures in the flame tubes, which exceed those in planar flames, increase as flame strips become shorter but then decrease as conditions evolve towards boundaries at which flame extinction occurs. Flame-tube structures thus can be remarkably varied, depending on the strain rate and the stoichiometric mixture fraction. The extremely broad range of steady, stable flame structures that are possible likely would not have been anticipated in advance of this study.

Future computational, experimental, and theoretical research in this area would be of interest. It could be helpful to explore the extent to which an available systematic further reduction of the present chemistry to a one-step description can be successful. Experiments designed to achieve more than one flame configuration under identical conditions with different ignition procedures also could be revealing. For example, a planar flame could be established under conditions where hysteresis is predicted, and holes could temporarily be blown into it, to see if flame tubes develop. Also, single and multiple sparks could be employed in ignition to investigate whether different numbers of stable flame tubes can be established.The wide variety of different phenomena encountered in this study points to a fertile field for future investigations.

This chapter is in preparation for publication in *Combustion and Flame*, ""Near-limit $H_2$-$O_2$-$N_2$ combustion in nonpremixed counterflow mixing layers", by J. Carpio, P. Rajamanickam, A. L. Sánchez, P. D. Ronney, F. A. Williams. The dissertation author is the primary investigator in this publication.

# Bibliography


[1] Antonio L Sánchez and Forman A Williams. Recent advances in understanding of flammability characteristics of hydrogen. *Progress in Energy and Combustion Science*, 41:1–55, 2014.

[2] Bernard Lewis and Guenther Von Elbe. *Combustion, flames and explosions of gases*. Elsevier, 2012.

[3] Eduardo Fernández-Tarrazo, Antonio L Sánchez, Amable Liñán, and Forman A Williams.

Flammability conditions for ultra-lean hydrogen premixed combustion based on flame-ball analyses. *International Journal of Hydrogen Energy*, 37(2):1813–1825, 2012.

[4] Zhenghong Zhou, Siena S Applebaum, and Paul D Ronney. Effect of stoichiometric mixture fraction on nonpremixed $h_2o_2n_2$ edge-flames. *Proceedings of the Combustion Institute*, 37(2):1989–1996, 2019.

[5] S R Lee and J S Kim. Nonlinear dynamic characteristics of flame stripes formed in strained diffusion flames by diffusional-thermal instability. *Combustion Theory and Modelling*, 4(1):29–46, 2000.

[6] R W Thatcher and J W Dold. Edges of flames that do not exist: flame-edge dynamics in a non-premixed counterflow. *Combustion Theory and Modelling*, 4(4):435–457, 2000.

[7] M Short, J D Buckmaster, and S Kochevets. Edge-flames and sublimit hydrogen combustion. *Combustion and Flame*, 125(1-2):893–905, 2001.

[8] R W Thatcher, A A Omon-Arancibia, and J W Dold. Oscillatory flame edge propagation, isolated flame tubes and stability in a non-premixed counterflow. *Combustion Theory and Modelling*, 6(3):487–502, 2002.

[9] S R Lee and J S Kim. On the sublimit solution branches of the stripe patterns formed in counterflow diffusion flames by diffusional-thermal instability. *Combustion Theory and Modelling*, 6(2):263–278, 2002.

[10] Pierre Boivin, Antonio L Sánchez, and Forman A Williams. Four-step and three-step systematically reduced chemistry for wide-range $H_2$–air combustion problems. *Combustion and Flame*, 160(1):76–82, 2013.

[11] Daniel Fernández-Galisteo, Adam Weiss, Antonio L Sánchez, and Forman A Williams. A one-step reduced mechanism for near-limit hydrogen combustion with general stoichiometry. *Combustion and Flame*, 208:1–4, 2019.

[12] Adam D Weiss, Antonio L Sánchez, and Forman A Williams. Accuracies of reduced mechanisms for predicting acoustic combustion instabilities. *Combustion and Flame*, 209:405–407, 2019.

[13] The San Diego Mechanism: Chemical-Kinetic Mechanisms for Combustion Applications. https://web.eng.ucsd.edu/mae/groups/combustion/mechanism.html. Version: 2016-12-14.

[14] Jaime Carpio, Juan Luis Prieto, and Marcos Vera. A local anisotropic adaptive algorithm for the solution of low-mach transient combustion problems. *Journal of Computational Physics*, 306:19–42, 2016.

[15] Amable Liñán. The asymptotic structure of counterflow diffusion flames for large activation energies. *Acta Astronautica*, 1(7-8):1007–1039, 1974.

# Part II

# Thermal explosion theory of hypergolic reactants

## Brief overview

When a sphere of one reactant is placed in the medium of another reactant with which it is hypergolic, a chemical reaction (modeled here as a zeroth-order one-step irreversible Arrhenius reaction) occurs at the common interface of the two reactants, and the heat generated at the interface then is transmitted away from it by thermal conduction. Depending on the nature of the problem, the system may approach an explosive mode, or it may settle into a steady-state mode. The critical condition defining the transition between these two states is determined analytically. In particular, explicit formulas for the ignition delay time for the explosive mode are provided for two limits, one in which an appropriately defined Damköhler number is large and other in which it is closer to the critical conditions. This is accomplished in chapter 4 by deriving and solving an integral equation for the time evolution of the interface temperature, employing activation-energy asymptotics.

# Chapter 4

# The Thermal-Explosion Characteristics of Hypergolic Gelled Propellants

## 4.1 Introduction

The definitive property of hypergolic reactants is that they do not require a hot ignition source to initiate the chemical reaction. Despite its hazardous nature, there is renewed interest in hypergolic propellants, as may been from recent technical reports [1, 2] and the results of many studies referenced therein, in part, due to the fact it is easier to handle these reactants once they have undergone gelation with additives. In addition, the gellant additives can also be used to vary the overall transport properties of the medium. In actual rocket propulsion, these reactants are injected as jets into the combustion chamber, where reactants mainly interact with each other through droplet-droplet collisions. From the viewpoint of theoretical modeling, however, in order to clarify the hypergolicity, a situation in which one gelled reactant is syringed or, dropped into a pool of another gelled reactant may be considered first, as in laboratory experiments.

In this connection, a relatively recent paper by Williams [3], a particular model for ignition of hypergolic gelled propellants was presented in which two hypergolic reactants of infinite extent

in contact with each other at a common planar interface was studied by Williams [3] in a relatively recent paper. It was found there that explosion occurs always at a finite time. Further attempts to improve this model [4, 5] are still found to be confined to the Cartesian geometry considered in [3]. If, however, one or both of the reactants are of finite extent, then it may be expected that the event of ignition itself may not occur in the first place owing to the fact that under certain conditions a steady state can be reached for the heat-transport process. The transition between thermal runaway and steady state, in typical combustion processes, is usually discrete, a well-known phenomenon associated with the large activation energy of the reaction. Hence, a parameter i.e., a Damköhler number, characterizing this discrete transition, has to be introduced to consider reactants of finite extent. A further point to note is that an appreciable amount of study has been developed on the subject lately, as may be seen from recent technical reports [1, 2] that contain thorough reviews.

In this study the problem in which one of the reactant is of finite extent is considered, with other simplifications and assumptions being essentially the same as in the earlier work [3]. For simplicity, the finite-sized reactant is assumed to be spherically symmetric, although predictions are expected to be valid for other similar geometries with characteristic sizes the same as that of the radius of the sphere.

A volterra-type nonlinear integral equation can be derived for problems of these kind, as can be seen from classical ignition theories of solid propellants [6–8] and from problems of heat (mass) transfer with surface radiation (reaction) [9–11]. Here, a similar integral equation governing the time evolution of the interface temperature will be derived for spherically symmetric heterogeneous systems. Given the number of approximations introduced in this elementary study directed towards the understanding of influences due to finite reactant-proportions, following [3], a complete solution to this integral equation is not attempted here, but an approximate solution, bringing out the essential features of this equation, for two extreme cases of Damköhler number, is presented. The required critical values for the Damköhler number are also derived from this

integral equation directly.

## 4.2 The governing equations and the boundary conditions of the problem

The problem can be described as follows. At time $t = 0$, a drop of fuel of radius $a$ and temperature $T'_{Fo}$ is placed in an infinitely large oxidizer environment, maintained at a temperature $T'_{Oo}$. Then with the interface reaction assumed to obey a zeroth-order one-step irreversible Arrhenius reaction, it is required to find the temperature at all locations for all further instants $t > 0$; in particular, the time history of the interface temperature is of central interest.

In view of the simplifications assumed, which are the same as those of [3], the governing equation for the temperature $T'_i$ of species $i$ is simply the heat equation,

$$\frac{\partial T'_i}{\partial t} = \frac{\alpha_i}{r^2}\frac{\partial}{\partial r}\left(r^2\frac{\partial T'_i}{\partial r}\right), \qquad i = F, O \tag{4.1}$$

where $\alpha_i$ is the thermal diffusivity of species $i$ and $r$ is the distance measured from the center of the fuel-drop. The initial and boundary conditions are given accordingly by

$$t = 0: \qquad T'_F = T'_{Fo}, (0 < r < a), \qquad T'_O = T'_{Oo}, (a < r < \infty), \tag{4.2}$$

$$t > 0: \qquad \frac{\partial T'_F}{\partial r} = 0, (r = 0), \qquad T'_O = T'_{Oo}, (r \to \infty). \tag{4.3}$$

Since the heterogeneous reaction occurs at the interface $r = a$, the conditions that need to be satisfied at the interface are

$$T'_F = T'_O = T'_I, \quad \text{and} \quad \lambda_F\frac{\partial T'_F}{\partial r} - \lambda_O\frac{\partial T'_O}{\partial r} = q_s e^{-E/\bar{R}T'_I}, \tag{4.4}$$

where $T'_I(t)$ is the interface temperature, $\lambda_i$ is the thermal conductivity of species $i$, and $q_s$ is

the rate of heat release per unit surface area. Here, $E$ is the activation energy of the one-step reaction and $\bar{R}$ is the universal gas constant. The second interface condition is obtained by integrating the time-dependent energy equation across the interface, taking the limit of vanishing interface thickness with the assumption that $q_s$ is finite. In the above model, fuel and oxidizer are distinguished purely by geometrical effects, whereas the one-step model chemistry is completely symmetric with respect to fuel and oxidizer. If the geometrical role of fuel and oxidizer are interchanged, all corresponding results and discussions should also be interchanged.

The linear problem free of interface heat-release, obtained by setting $q_s = 0$ in equation (4.4), has been solved by Brown [12] for constant initial temperatures and by Konopliv and Sparrow [13] for arbitrary initial temperature distributions.

As a matter of fact, the spatial temperature profile evolves on two different time scales, namely, the diffusion time scale that is important in most of the region and the chemical time scale that is assumed to exert an effect only at the interface. These two time scales are different from each other unless their ratio (defining a Damköhler number) is of order unity. Numerical methods that try to solve the above set of equations must be such that the fastest of the two time scales be well resolved. But, for problems of this nature, the complexity associated with the two time scales can be circumvented by separating the interface problem from the outer diffusional problem in a sense that will be clear as we proceed further.

To facilitate the outer diffusion problem first, we introduce the dimensionless variables and parameters

$$\tau = \frac{\alpha_F t}{a^2}, \quad y = \frac{r}{a}, \quad T_i = \frac{T_i'}{T_{Fo}'}, \quad \alpha = \frac{T_{Oo}'}{T_{Fo}'}, \quad L = \frac{\lambda_O}{\lambda_F}, \quad R = \frac{r_O}{r_F}, \quad Q = \frac{aq_s}{\lambda_F T_{Fo}'}, \tag{4.5}$$

where $r_i = \lambda_i/\sqrt{\alpha_i}$ is the thermal responsivity (or thermal effusivity) of species $i$. The governing

equations consequently become

$$\frac{\partial T_F}{\partial \tau} = \frac{1}{y^2}\frac{\partial}{\partial y}\left(y^2\frac{\partial T_F}{\partial y}\right), \quad \frac{\partial T_O}{\partial \tau} = \frac{L^2}{R^2 y^2}\frac{\partial}{\partial y}\left(y^2\frac{\partial T_O}{\partial y}\right) \tag{4.6}$$

while the corresponding initial and boundary conditions change to

$$\tau = 0: \qquad T_F = 1, (0 < y < 1), \qquad T_O = \alpha, (1 < y < \infty), \tag{4.7}$$

$$\tau > 0: \qquad \frac{\partial T_F}{\partial y} = 0, (y = 0), \qquad T_O = \alpha, (y \to \infty). \tag{4.8}$$

Finally, the interface conditions for $\tau > 0$ can be written as

$$y = 1: \qquad T_F = T_O = T_I, \qquad \frac{\partial T_F}{\partial y} - L\frac{\partial T_O}{\partial y} = Qe^{-E/\bar{R}T'_{Fo}T_I}. \tag{4.9}$$

The above problem possess a non-trivial steady solution unique to the spherical geometry considered here, while no such steady solutions can be found for configurations with cylindrical or planar symmetry. The discussion of such solutions will be postponed to section V, since it seems helpful to deduce results in terms of activation-energy asymptotics first.

## 4.3 A general method of solution and the derivation of an integral equation governing the interface temperature

Since the nonlinear term enters only through a boundary condition, methods for linear problems can be applied here to the extent that they do not involve the interface condition exhibiting the nonlinear behaviour. For the same reason, there are several ways to arrive at the same result, of which the technique of Laplace transforms is exploited in this work, as was done

in references [3, 6–10, 12, 13]. The Laplace transforms of the dependent variables are defined as

$$\tilde{T}_i = \mathscr{L}(T_i) = \int_0^\infty T_i\, e^{-s\tau}\, \mathrm{d}\tau, \qquad i = F, O. \tag{4.10}$$

The governing equations then reduce to ordinary differential equations,

$$\frac{\mathrm{d}^2\tilde{T}_F}{\mathrm{d}y^2} + \frac{2}{y}\frac{\mathrm{d}\tilde{T}_F}{\mathrm{d}y} = s\tilde{T}_F - 1, \quad \frac{\mathrm{d}^2\tilde{T}_O}{\mathrm{d}y^2} + \frac{2}{y}\frac{\mathrm{d}\tilde{T}_O}{\mathrm{d}y} = \frac{R^2}{L^2}(s\tilde{T}_O - \alpha), \tag{4.11}$$

whose solutions satisfying the conditions away from the interface are

$$\tilde{T}_F = \tilde{F}_F(s)\frac{\sinh\sqrt{s}y}{y} + \frac{1}{s}, \qquad \tilde{T}_O = \tilde{F}_O(s)\frac{e^{-y\sqrt{s}R/L}}{y} + \frac{\alpha}{s} \tag{4.12}$$

where $\tilde{F}_F(s)$ and $\tilde{F}_O(s)$ are constants of integration. Continuity of temperature at $y = 1$ implies

$$\tilde{F}_F \sinh\sqrt{s} + \frac{1-\alpha}{s} = \tilde{F}_O e^{-\sqrt{s}R/L}, \tag{4.13}$$

whereas the flux-jump (4.9) at the interface leads to

$$\tilde{F}_F \sinh\sqrt{s}(\sqrt{s}\coth\sqrt{s} - 1) + \tilde{F}_O e^{-\sqrt{s}R/L}(\sqrt{s}R + L) = Q\int_0^\infty e^{-E/\bar{R}T'_{Fo}T_I} e^{-s\tau}\, \mathrm{d}\tau. \tag{4.14}$$

By eliminating $\tilde{F}_O$ between the foregoing two equations we obtain an equation for $\tilde{F}_F$,

$$\sqrt{s}\tilde{F}_F \sinh\sqrt{s}\left(\coth\sqrt{s} + R + \frac{L-1}{\sqrt{s}}\right) + (1-\alpha)\left(\frac{R}{s} + \frac{L}{\sqrt{s}}\right) = Q\int_0^\infty e^{-E/\bar{R}T'_{Fo}T_I} e^{-s\tau}\, \mathrm{d}\tau. \tag{4.15}$$

This completes the solution for the outer diffusion problem since $T_F$ and $T_O$ in principle can be expressed as quadratures by inverting (4.10), with $\tilde{F}_F$ determined from an integral equation that governs the inner interface temperature.

### 4.3.1 Determination of initial interface temperature

The interface temperature, although discontinuous at $t = 0$, will become continuous instantaneously for $t > 0$ as a necessary consequence of the heat equation, such that we can speak of a unique interface temperature as $t \to 0^+$. Also, since the heat release by chemical reaction has not begun at these initial instants, the initial interface temperature can be obtained from equation (4.15) after removing its right-hand side, to result in

$$s\tilde{F}_F \sinh\sqrt{s} = -\frac{(1-\alpha)(R+L/\sqrt{s})}{\coth\sqrt{s}+R+(L-1)/\sqrt{s}}. \tag{4.16}$$

By definition, $\tilde{F}_F \sinh\sqrt{s}$ is the Laplace transform of $T_I - 1$ and to find $T_{Io} - 1$, where $T_{Io}$ is the initial interface temperature in non-dimensional form, we take the limit $s \to \infty$ and apply initial-value theorem, yielding

$$T_{Io} = \frac{1+\alpha R}{R+1}. \tag{4.17}$$

The dimensional initial interface temperature $T'_{Io}$ is simply a weighted average of initial temperatures with thermal responsivities being the weight factors. This result, the same as that of the planar problem [3], is in fact valid for arbitrary interfaces that are smooth.

### 4.3.2 The integral equation

Following Williams [3], next we study the evolution of the departure of the interface temperature from its initial value, i.e., we define $F = T_I - T_{Io}$, so its Laplace transform $\tilde{F} = (F)$ becomes $\tilde{F} = \tilde{F}_F \sinh\sqrt{s} + R(1-\alpha)/[s(R+1)]$. Equation (4.15) can be re-written in terms of $\tilde{F}$ as

$$\sqrt{s}\tilde{F}\left(\coth\sqrt{s}+R\right) + \frac{R(1-\alpha)(1-\coth\sqrt{s})}{\sqrt{s}(R+1)} + \frac{(1-\alpha)(L+R)}{s(R+1)} + (L-1)\tilde{F} = Q\int_0^\infty e^{-E/\bar{R}T'_{Fo}(F+T_{Io})} e^{-s\tau}\,\mathrm{d}\tau. \tag{4.18}$$

Taking the inverse Laplace transform using Bateman's tables [14] gives

$$\int_0^\tau \frac{\mathrm{d}F(\tau')}{\mathrm{d}\tau'}\left[\vartheta_3\left(0|i\pi(\tau-\tau')\right)+\frac{R}{\sqrt{\pi(\tau-\tau')}}\right]\mathrm{d}\tau'+\frac{R(1-\alpha)}{R+1}\left[\frac{1}{\sqrt{\pi\tau}}-\vartheta_3(0|i\pi\tau)+\frac{L}{R}+1\right]$$
$$+(L-1)F=Qe^{-E/\bar{R}T'_{Fo}[F+T_{Io}]}, \tag{4.19}$$

where $\vartheta_3(0|i\pi\tau)$ is one of the Jacobi theta functions, in which the argument $i\pi\tau$ often is called the lattice parameter. The preceding equation is the required integral equation for $F(\tau)$ subjected to the condition $F(0)=0$.

## 4.4 The application of activation-energy asymptotics

As previously discussed, evolution of the interface temperature should be scaled with the chemical time. In large-activation-energy asymptotics, the small parameter of expansion can be defined as $\varepsilon=\bar{R}T'_{Io}/E\ll 1$. From the dimensional equations (1)-(4), it is clear that the characteristic heat-conduction time and the characteristic explosion time, respectively, are given by

$$t_c=\frac{a^2}{\alpha_F}\quad\text{and}\quad t_e=\frac{a\varepsilon T'_{Io}\lambda_F}{q_s e^{-1/\varepsilon}\alpha_F}. \tag{4.20}$$

The non-dimensional parameters and variables required for activation-energy asymptotics become

$$\delta=\frac{t_c}{t_e},\quad \varpi=\frac{\pi t}{t_e}=\delta\pi\tau,\quad \psi=\frac{F}{\varepsilon T_{Io}}=\frac{F(R+1)}{\varepsilon(1+\alpha R)},\quad \gamma=\frac{1-\alpha}{\varepsilon(1+\alpha R)}, \tag{4.21}$$

where $\delta$ is the Damköhler number. The parameter $\gamma$, measuring the relative difference between the initial temperatures of the two reactants, can range from negative values of the orders of tens to positive values of the same orders, for the typical values $\alpha\sim O(1)$ and $\varepsilon=0.01-0.1$.

With the scales introduced in this section, equation (4.19) becomes

$$\int_0^{\varpi} \frac{\mathrm{d}\psi(\varpi')}{\mathrm{d}\varpi'} \left[ \vartheta_3 \left( 0 \middle| \frac{i(\varpi-\varpi')}{\delta} \right) + \frac{R\sqrt{\delta}}{\sqrt{\varpi-\varpi'}} \right] \mathrm{d}\varpi' + R\gamma \left[ \frac{\sqrt{\delta}}{\sqrt{\varpi}} - \vartheta_3 \left( 0 \middle| \frac{i\varpi}{\delta} \right) + \frac{L}{R} + 1 \right] + (L-1)\psi = \delta e^{\psi/(1+\varepsilon\psi)} \approx \delta e^{\psi}, \tag{4.22}$$

where, on the premise of activation-energy asymptotics, the Arrhenius term at the end has been linearized following Frank-Kamenetskii [15]. The explicit dependence on $\varepsilon$ has thus been removed, thereby leaving $R$, $L$, $\gamma$, and $\delta$ as the four independent parameters of the problem.

The particular theta function that appears in the integral equation can be represented by two different forms[2],

$$\vartheta_3 \left( 0 \middle| \frac{i\varpi}{\delta} \right) = 1 + 2\sum_{n=1}^{\infty} e^{-\pi n^2 \varpi/\delta} = \frac{\sqrt{\delta}}{\sqrt{\varpi}} \left[ 1 + 2\sum_{n=1}^{\infty} e^{-\pi n^2 \delta/\varpi} \right]. \tag{4.23}$$

where the second representation is obtained by taking the Jacobi imaginary transformation (cf. [16], p. 475) of the first representation. These two representations will be useful in deriving the limiting forms of the theta function in various limits.

## 4.5 The steady solution and the Frank-Kamenetskii parameter

For given values of $R$, $L$ and $\gamma$, a steady solution is expected to occur only for $\delta \leq \delta_c$, where $\delta_c$ is the critical Damköhler number, also known as the Frank-Kamenetskii parameter [15]. Taking the limit $\varpi \to \infty$ in equation (4.22), keeping other parameters fixed, the steady solution

[2]The two representations are related by the identity $\vartheta_3(0|ix^{-1}) = \sqrt{x}\vartheta_3(0|ix)$.

$\psi_s$ is found to satisfy the following equation[3]

$$\psi_s + \gamma = \frac{\delta}{L} e^{\psi_s}. \tag{4.24}$$

Except for the appearance of $\gamma$, the above equation is similar to one obtained by Semenov [17] in the thermal-explosion theory of well-mixed reactants. One may also notice that, in steady state, the heat liberated by the interface reaction is lost only to the oxidizer as in Semenov's case, where heat loss occurs only at the enclosing wall, but for a different reason, i.e. due to the assumption of large conductivity for the reactant mixture in the Semenov analysis.

An explicit solution can be written for $\psi_s$ in terms of Lambert W function [18],

$$-\psi_s = \gamma + W\left(-\frac{\delta e^{-\gamma}}{L}\right). \tag{4.25}$$

Since the Lambert W function is real only when its argument $x \geq -1/e$, we immediately determine the condition for existence of a real, steady interface temperature, written in terms of the critical Damköhler number, to be

$$\delta \leq \delta_c = L e^{\gamma - 1}. \tag{4.26}$$

For cases in which both fuel and oxidizer have the same initial temperature, the Frank-Kamenetskii parameter $\delta_c = L/e$ is an order-unity number. By way of contrast, if the fuel sphere has an initial temperature which is much hotter than the oxidizer ($\alpha \ll 1$), then $\delta_c \sim e^{1/\varepsilon}$, i.e. in the limit of vanishing $\varepsilon$, the system never goes to explosive mode, while, in the opposite case ($\alpha \gg 1$), the system never reaches a steady state, since in this limit $\delta_c \sim e^{-1/\varepsilon}$.

For obvious reasons, the argument of the Lambert W function in (4.25) is nonpositive in all possible situations, while the function $W(x)$ itself has two branches in that range $-1/e \leq x < 0$, the upper (principal) branch, $W_0(x)$ and the lower branch, $W_{-1}(x)$ (see left plot of Fig. 4.1), of

[3]The temperature distribution in steady state, outside the interface is given by $T_F = T_I$ and $T_O = (T_I - \alpha)/y + \alpha$, where $T_I = T_{Io}(1 + \varepsilon\psi_s)$.

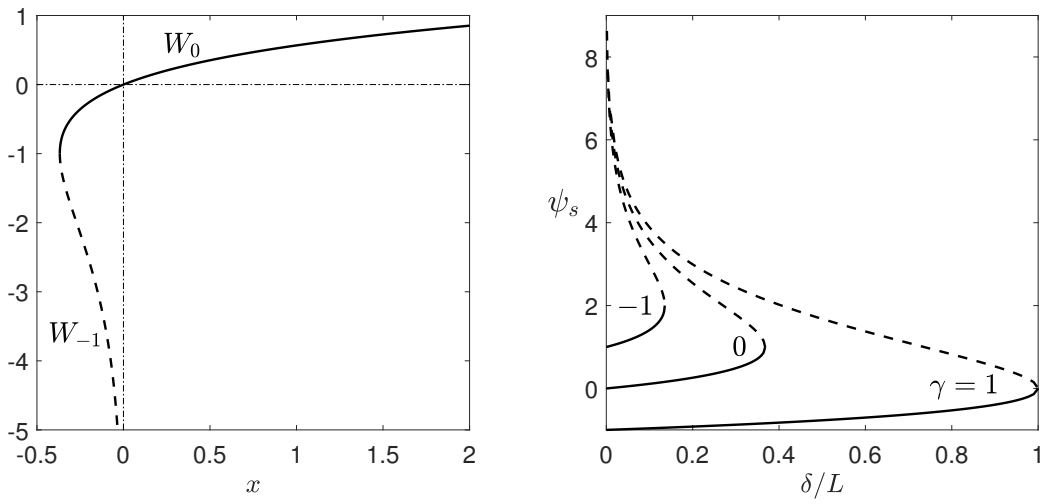


**Figure 4.1**: The left-hand side plot shows the real-valued figure of Lambert W-Function, comprising of two branches, the principal branch (solid curve) and the lower branch (dashed curve), whereas the right-hand side plot draws the curve for steady solution, evaluated using both branches of the Lambert function.

which one has to be selected based on physical grounds. It seems that the principal branch obeys the fact that a steady interface temperature, whenever it exists, should increase for increasing values of $\delta$ when other parameters are kept fixed, a typical expectation which follows directly from S-shaped ignition-extinction curve. This can be seen to be true from the right plot of Fig. 4.1, where steady solutions are plotted as functions of $\delta/L$ for different possible values of the Frank-Kamenetskii parameter via $\delta_c/L$ for both branches of $W(x)$. By comparing this figure with the typical curves of thermal-explosion theory, we can identify $W_0$ to be the stable branch and $W_{-1}$ as unstable.

## 4.6 A simplified integral equation applicable in the range $\delta \gg 1$ and its approximate solution

Now that we have a well-defined criterion for the existence of steady solutions, we can turn our attention to unsteady problems and consider the limit of large Damköhler numbers

first. As $\delta \to \infty$, a thermal runaway is expected to occur in a short interval of time from the inception, with solutions approaching the planar problem considered by Williams [3][4]. For the planar geometry, ignition occurs at times of order $\varpi \sim \delta^{-1}$. Thus, the ratio $\varpi/\delta$ can at most be of the order $\delta^{-2}$ and hence the theta function can be approximated as $\vartheta_3(0|i\varpi/\delta) \approx \sqrt{\delta/\varpi}$ with exponentially small corrections.

By defining a new time coordinate $\eta = \delta\varpi/(R+1)^2$ and by introducing two new parameters $\Lambda = \gamma(R+L)/\delta$ and $k = (L-1)/\delta$, the integral equation (4.22), in the limit of large Damköhler number, can be shown to reduce to

$$\int_0^\eta \frac{\mathrm{d}\psi}{\mathrm{d}\eta'} \frac{\mathrm{d}\eta'}{\sqrt{\eta-\eta'}} + \Lambda + k\psi = e^\psi, \tag{4.27}$$

where the function $\psi$ inside the integral should be interpreted as $\psi = \psi(\eta')$. Due to the exponentially small corrections, the above equation will not differ markedly from (4.22) even for moderately large $\delta$; for example, the error is already of order $10^{-4}$ when $\delta = 3$. For this reason, although strictly speaking, in the asymptotic sense, $\Lambda$ and $k$ should be treated as first-order corrections, we may as well treat them as order unity quantities since this may be true for large but finite values of $\delta$.

By the above arguments, we can see that the distinguished double limit $(\Lambda, k) \to (0,0)$ is planar in character, and in this limit, the simplified integral equation reduces to the Williams equation [3]. The conditions under which $\Lambda$ and $k$ vanishes can be inferred directly from their definitions.

The simplified integral equation is not soluble in terms of elementary functions, whence it will be solved locally both for small times and near the point where the solution diverges indefinitely. An approximation to a uniform solution will be constructed out of these two solutions by the method of patching. Only those values of $\Lambda$ and $k$ for which these local solutions

[4] A more precise statement would be to define $\delta - \delta_c \to \infty$ as the planar limit, rather than $\delta \to \infty$. For example, eqn. (4.27) does not always produce an explosive solution; $\delta$ can be less than $\delta_c$.

are reasonably accurate and for which $\delta > \delta_c$, will be considered.

For $\eta \ll 1$, a power-series expansion leads to

$$\psi(\eta) = \frac{2p}{\pi}\sqrt{\eta} + \frac{ps}{\pi}\eta + \frac{4p(2p+\pi s^2)}{3\pi^3}\eta^{3/2} + \frac{p[2p^2+ps(3\pi+4)+2\pi s^3]}{4\pi^3}\eta^2 + \cdots \quad (4.28)$$

where $p = 1-\Lambda$ and $s = 1-k$ have been introduced for shortness.

As far as the terminal profile is concerned, obtaining a neat perturbation series like the one for the initial profile is non-trivial; therefore an approximate solution will be derived in the following. Let $\eta = c$ be the point at which the solution diverges. Then in the neighborhood of $\eta = c$, the upper limit $\eta$ appearing in the integral in Eqn. (4.27) can be replaced by $c$ and the lower limit of integration itself can be shifted to $\eta$ since the major contribution to the integral term comes from this neighborhood. A simple consideration shows then that the integral equation (4.27) can be approximated by the differential equation $\pi\sqrt{c-\eta}\,\mathrm{d}\psi/\mathrm{d}\eta + \Lambda + k\psi = e^{\psi}$.[5] The equation has to integrated with the condition that $\psi$ becomes infinite at $\eta = c$. A straightforward integration shows then that

$$\frac{2}{\pi}\sqrt{c-\eta} = G(\psi;\Lambda,k) \equiv \int_{\psi}^{\infty} \frac{\mathrm{d}\psi'}{e^{\psi'} - \Lambda - k\psi'}. \quad (4.29)$$

The function $G$, in general, has to be calculated numerically except for the case $k = 0$, for which the above equation simplifies to $\Lambda e^{-\psi} = 1 - e^{-2\Lambda\sqrt{c-\eta}/\pi}$, which as it must, reduces to eqn.(23) of [3] for small values of $\Lambda$. Although $G$ is well-behaved since it tends to $e^{-\psi}$ as $\psi \to \infty$, it may become singular in a logarithmic fashion depending on the values of $\Lambda$ and $k$ if $\psi$ is not sufficiently large. For the values considered for $(\Lambda, k)$ in this study and for the domain where both initial and terminal solution are accurate enough, $G$ is non-singular.

The problem remains to determine the constant $c$ by matching the initial and the terminal solution. In order to do that, $\eta$ will be treated as a function of $\psi$. An intermediate point $\psi = \psi_p$

[5]The factor $\pi$ is easy to obtain if one recognises that one can always find a region near $\eta = c$ where $\Lambda$ and $k\psi$ are negligible when compared to the other two terms. With $\Lambda$ and $k$ neglected then, only $\pi$ is found to be consistent for the solution of the differential equation and the leading-order solution of the integral equation (4.27) to be the same.

is assumed to exist where both the initial profile (4.28) (after solving for $\eta = H(\psi;\Lambda,k)$) and the terminal profile (4.29) have the same value, at which point, the slope of two curves is also assumed to be continuous. This leads to two conditions for the two unknowns, $c$ and $\psi_p$. The patching point $\psi_p$ can be found from an appropriate root of $4\mathrm{d}H/\mathrm{d}\psi + \pi^2 \mathrm{d}G^2/\mathrm{d}\psi = 0$ and the value of $c(\Lambda,k)$ can be found from $c = H(\psi_p) + \pi^2 G^2(\psi_p)/4$.

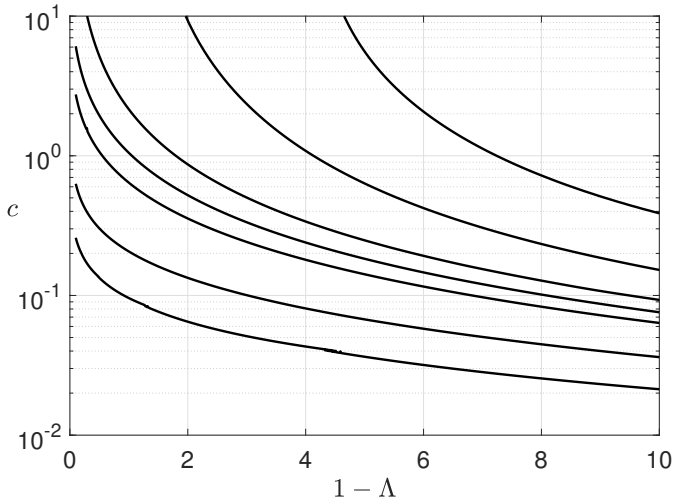


**Figure 4.2**: Plots of explosion point $c(\Lambda)$ for values of $k = -10, -5, -1, 0, 1, 3, 5$ corresponding to bottom curve to top curve, respectively .

To plot results, we keep first the four terms of (4.28) in evaluating $c$ since retaining more terms seems to have little influence on the value of $c$. The curves of $c(\Lambda)$ for fixed values of $k$ are plotted as solid curves in Fig. 4.2. The result is increasingly accurate for decreasing values of $c$. Increasing either $\Lambda$ or $k$ evidently delays ignition so that the delay time can become larger or smaller than that of the planar problem depending on values of these two parameters. For Williams [3], who had kept only the first term in (4.28), the value of $c$ is universal and equal to $c(0,0)$. This value which he found to be 1.5 seems to decrease and approach unity as we include more terms to the initial solution.

## 4.7 The solution characteristics for sub-critical and near-critical limits

For simplicity, only the case $\gamma = 0$ (equal initial temperatures) is considered in this section. Then from (4.26), the Frank-Kamenetskii parameter simply becomes $\delta_c = L/e$, while the steady-state value of $\psi$ at this critical condition is $\psi_s = 1$ according to (4.25). Also, the steady-state value of $\psi$ for $\delta < \delta_c$ is $\psi_s = -W_0(-\delta/L)$ from (4.25).

Prior to investigating the near-critical limit $|\delta - \delta_c| \ll 1$, it is helpful to first understand the solution behaviour throughout the sub-critical range $\delta < \delta_c$. In the sub-critical regime, the transient solution evolves on time scales of the order of $t_c$, eventually reaching a steady value, and therefore it is appropriate to work with $\tau$ in place of $\varpi$ as the relevant non-dimensional time variable. Here, we are interested only in the asymptotic behaviour of the transient solution for large $\tau$. In terms of $\tau$, the integral equation (4.22), as $\tau \to \infty$, after introducing $\psi(\tau) = \psi_s + \theta(\tau)$, with $\theta \ll 1$, reduces to

$$\int_0^\tau \frac{\mathrm{d}\theta}{\mathrm{d}\tau'} \frac{R\mathrm{d}\tau'}{\sqrt{\pi(\tau - \tau')}} + \mu L\theta = L(1-\mu)\left(\frac{\theta^2}{2!} + \frac{\theta^3}{3!} + \cdots\right), \tag{4.30}$$

where $\mu = 1 - \psi_s < 1$ measures the difference between the steady-state temperature for the critical condition $\delta = \delta_c$ and that for the sub-critical condition $\delta < \delta_c$; $\mu$ vanishes when $\delta = \delta_c$. The linear integral equation that is obtained by neglecting $\theta^2$ and higher-order terms can be solved by Laplace transforms [14], to give

$$\theta = \theta_o e^{L^2\mu^2\tau/R^2} \mathrm{erfc}\left(\frac{L\mu}{R}\sqrt{\tau}\right) \approx \frac{R\theta_o}{L\mu\sqrt{\pi\tau}}, \tag{4.31}$$

where $\theta_o$ is a constant that can be determined numerically. This indicates an algebraic decay to the steady solution which is qualitatively different from the exponential decay (cf. [19], eqn.14 and [20], eqn.3.1) observed for Semenov's problem.

The above asymptotic solution is valid for order-unity values of $\mu$, but in the near-critical limit $\mu \to 0$, it develops a sequence of non-uniformities as $\tau$ runs to infinity; for instance, the $\theta^2$ term in (4.30) is no longer negligible when $\theta \sim \mu$, that being the order of magnitude when $\tau \sim \mu^{-4}$ according to (4.31). A familiar example that is analogous to this situation is the difficulty in obtaining a uniform formula through activation-energy asymptotics for the laminar burning velocity of planar premixed flames, that include both near-stoichiometric and far-from-stoichiometric equivalence ratios. The origin of trouble lies in the expansion about $\psi_s$ for $\psi$, while the correct expansion should have been about unity for near-critical limits.

The failure of the preceding solution for the near-critical limit forces us to reconsider the inherent balance in (4.30) in order to identify the correct leading-order terms. In trying to reformulate the problem for the near-critical case $\delta_c - \delta \ll 1$, we can also incorporate the super-critical case $\delta - \delta_c \ll 1$ in the same formulation, but it is not meaningful to use $\mu$ for super-critical conditions because $\psi_s$ does not exist. Thus we introduce $\nu \ll 1$ such that $\delta = \delta_c(1 \pm \nu)$, with plus and minus signs, respectively, corresponding to super- and sub-critical regimes. A correspondence between $\nu \ll 1$ and $\mu \ll 1$ can be made from (4.24) for the sub-critical case, $2\nu = \mu^2 + O(\mu^3)$.

The analysis of the near-critical limit, originally due to Frank-Kamenetskii [21], has been employed recently for premixed reactants flowing inside a pipe [22]. The required rescalings for the current problem are found to be $\xi = \pi\nu\tau L^2/(2R^2)$ and $\psi = 1 + \sqrt{2\nu}\chi - \nu$ (cf. [23], p. 406 and [24], p. 68). Substituting these new variables into (4.22) and neglecting terms of order $\nu^2$ leads to

$$\int_0^{\xi} \frac{\mathrm{d}\chi}{\mathrm{d}\xi'} \frac{\mathrm{d}\xi'}{\sqrt{\xi - \xi'}} = \chi^2 \pm 1, \qquad \chi(0) \to -\frac{1 - \psi_o}{\sqrt{2\nu}} \tag{4.32}$$

where $\psi_o < 1$ is an order-unity constant that contains information from the initial periods. In the sub-critical case, solution for $\chi$ exists at all times approaching $\chi + 1 \sim 1/\sqrt{\xi}$ as $\xi \to \infty$. On the contrary, for $\delta > \delta_c$, $\chi$ diverges at a finite value $\xi_c$ of $\xi$ according to $\chi \sim 1/\sqrt{\xi_c - \xi}$. The value of $\xi_c$ depends on $\nu$, and preliminary numerical integrations suggested that $\xi_c \sim (2\nu)^{-1}$.

Had we considered the case $\gamma \neq 0$, an additional term $\gamma(2\nu\xi)^{-1/2}$ would appear on the left-hand side of equation (4.32), suggesting two possible modifications for the super-critical case. For $\gamma > 0$, a balance of this new term with the Arrhenius term leads to $\chi(\xi) \to -[\gamma^2/(2\nu\xi)]^{1/4} \gg \chi(0)$ (only the negative root is allowed since only then will the quadratic approximation in (4.32) be a representative of the full Arrhenius expression) indicating that the solution has not yet approached the steady solution at this time scale. On the other hand, for $\gamma < 0$, we cannot find any real solution, meaning that the blowup of $\chi$ has already taken place at a time scale smaller than $\xi$. Different scalings therefore would be needed for $\gamma^2 \gtrapprox 2\nu$.

## 4.8 General discussions

From (4.26), in view of (4.5) and (4.21), explicit expressions are available for the critical Damköhler numbers above which ignition occurs, written in dimensional variables as

$$\frac{aq_sE}{\bar{R}T_{Io}'^2}e^{-E/\bar{R}T_{Io}'} \geq \frac{\lambda_O}{e}\exp\left[\frac{Er_F(T_{Fo}'-T_{Oo}')}{\bar{R}T_{Io}'^2(r_F+r_O)}\right], \tag{4.33}$$

where $T_{Io}' = (r_F T_{Fo}' + r_O T_{Oo}')/(r_F + r_O)$. For fixed initial temperatures, the phenomenon of ignition is favoured by a larger fuel radius $a$ or a larger reaction parameter $q_s e^{-E/\bar{R}T_{Io}'}E/(\bar{R}T_{Io}')$. Decreasing $a$ delays ignition and makes it less likely to occur because it enhances (geometrically) rates of heat conduction away from the interface where the heat is being liberated. This is in qualitative agreement with the droplet-droplet collision experiments [1, 25], where it was observed that the ignition delay time increases with increasing droplet size ratio, defined such that this ratio is greater than unity. The augmented heat-conduction rates for small fuel-droplets undermine the effects of thermal conductivity of the fuel $\lambda_F$ (as if $\lambda_F$ is infinite), leaving heat-loss to the oxidizer as the principal way of taking heat away from the interface; this explains the presence of $\lambda_O$, but not $\lambda_F$ in the critical condition. Next keeping fuel radius and reaction parameter fixed, ignition is favoured more for the case $T_{Fo}' < T_{Oo}'$ since now there is an adverse temperature

gradient (additional to the gradient-jump induced by the interface reaction) at the interface that opposes heat-conduction to the oxidizer. The opposite case $T'_{Fo} > T'_{Oo}$ increases heat-loss to the oxidizer making it harder for the interface temperature to blow-up. The thermal responsivity is closely associated with the fact that the initial temperatures of the two reactants are different from each other and it disappears in the critical condition whenever $T'_{Fo} = T'_{Oo} = T'_{Io}$. Interestingly enough, when $T'_{Fo} \neq T'_{Oo}$, only the ratio $r_O/r_F$ appears explicitly in the critical condition as well as affects the initial interface temperature. If the effect on $T'_{Io}$ is ignored, then increasing this ratio promotes the ignition whenever $T'_{Fo} > T'_{Oo}$.

The ignition delay time in dimensional form that is appropriate for large Damköhler number defined in section VI is

$$t_{\text{ign}} = \frac{c}{\pi}\left[\frac{(r_F + r_O)\bar{R}T'^2_{Io}}{q_s E e^{-E/\bar{R}T'_{Io}}}\right]^2, \tag{4.34}$$

where the value of $c(\Lambda, k)$ can be obtained from Figure 4.2 for given values of

$$\Lambda = \frac{(T'_{Fo} - T'_{Oo})(r_F\lambda_O + r_O\lambda_F)}{aq_s(r_F + r_O)e^{-E/\bar{R}T'_{Io}}} \quad \text{and} \quad k = \frac{(\lambda_O - \lambda_F)\bar{R}T'^2_{Io}}{aq_s E e^{-E/\bar{R}T'_{Io}}}. \tag{4.35}$$

This ignition formula is same as that for the planar problem. As expected, the dependence of the ignition delay time on the fuel radius $a$ entering implicitly via $\Lambda$ and $k$, disappears in the planar limit $a \to \infty$. In the planar limit, the ignition formula is independent of the thermal conductivities because the heat-conduction is driven by huge temperature gradients induced by the fast chemical reaction, on both sides of the interface and not by the values of the thermal conductivities; the difference $\lambda_O - \lambda_F$ emerges in the first-order correction to the planar problem. Similarly, the temperature gradients associated with the initial-temperature differences also arise only in the first-order correction. The ignition formula, however, does depend on the sum of the responsivities since although the interface temperature is continuous at the interface, the temperature on either sides suffer rapid variations (quite independent of all parameters except the reaction parameter)

that necessitate the symmetric presence of the thermal responsivities in the formula.

In the near-critical limit, the ignition delay time can be written as

$$t_{\text{ign}} = \frac{b}{\pi}\left[\frac{ar_O\bar{R}T_{Io}'^2}{aeq_sEe^{-E/\bar{R}T_{Io}'} - \lambda_O\bar{R}T_{Io}'^2}\right]^2, \tag{4.36}$$

where $b$ is an order-unity constant that is not determined here. Since the preceding formula reduces to (4.34) as $a \to \infty$, the formula can be anticipated to be of general validity, although $b$ may no longer be a universal constant except for the two extreme cases considered in this work. The ignition delay time is inversely proportional to the measure of the inequality in equation (4.33) (after setting $T_{Fo}' = T_{Oo}'$) and consequently discussions pertaining to (4.33) are also valid here. For example, while the leading-order large Damköhler-number ignition formula (4.34) is symmetric with respect to both fuel and oxidizer, the above near-critical ignition formula depends only on the thermal properties of the oxidizer and not on that of the fuel.

## 4.9 Conclusions

The principal result of the study is the determination of critical conditions that separate steady solutions from thermal runaway. It is observed that ignition is promoted by increasing the fuel radius, or the reaction parameter or the initial temperature of the oxidizer or by decreasing the oxidizer thermal conductivity. Whenever the initial temperatures of the two reactants are not the same, the thermal responsivity ratio, in part, determines whether the chance of igniting the reactants is enhanced or worsened. In addition, the ignition delay times for large and near-critical Daköhler numbers are also estimated, where in the former case, the delay time is symmetric about the two reactants, while for the near-critical conditions, the delay time is dependent only on the properties of the oxidizer. In general, the ignition delay time is inversely proportional to the reaction parameter and directly proportional to the thermal responsivities, starting from the

case where the dependence is only on the oxidizer thermal responsivity to the case where the dependence is on both the fuel and the oxidizer thermal responsivities in a symmetric fashion. Knowledge of these dependances on various parameters are critical in having a better control on hypergolic ignition.

However the work mainly addresses the influences of finite proportions of the reactants and clearly more work is required for further understanding of hypergolic ignition and to make concrete predictions; in particular, to name a few of the factors that are neglected here, there may be interest in the effects of reactant depletion, the effects of detailed chemical kinetics, the effects of gel additives etc. An ignition study employing a reduced chemistry for the hypergolic reactants, but more complex than the one-step chemistry considered here could be the next step for future investigations.

This chapter, in part, has been published in *Journal of Propulsion and Power*, "Thermal explosion characteristics of a gelled hypergolic propellants", by P. Rajamanickam. The dissertation author is the primary investigator in this publication.

# Bibliography

[1] S T Thynell, J H Adair, W A Goddard III, R K Hanson, C K Law, J Lee, H A Rabitz, G A Risha, F A Williams, and V Yang. Spray and combustion of gelled hypergolic propellants for future rocket and missile engines. Technical report, Pennsylvania State University, State College, 2014.

[2] Stephen D Heister, William E Anderson, Carlos M Corvalan, Osvaldo H Campanella, Robert P Lucht, Timothee L Pourpoint, Paul E Sojka, Steven F Son, David P Schmidt, and Terrence R Meyer. Spray and combustion of gelled hypergolic propellants. Technical report, Purdue University, Lafayette, Indiana, 2014.

[3] Forman A Williams. Simplified theory for ignition times of hypergolic gelled propellants. *Journal of Propulsion and Power*, 25(6):1354–1357, 2009.

[4] Samuel Hassid and Benveniste Natan. Thermal diffusion controlled ignition of hypergolic gel propellants. *Journal of Propulsion and Power*, 29(6):1337–1342, 2013.

[5] David Andres Castaneda, Samuel Hassid, and Benveniste Natan. Modeling the hyper-

golic ignition of hydrogen peroxide with polyethylene. *Journal of Propulsion and Power*, 35(1):239–242, 2018.

[6] Forman Arthur Williams. Theory of propellant ignition by heterogeneous reaction. *AIAA Journal*, 4(8):1354–1357, 1966.

[7] Forman Arthur Williams, Marcel Barrère, and N C Huang. Fundamental aspects of solid propellant rockets. Technical report, Advisory Group for Aerospace Research and Development Neuilly-Sur-Seine, France, 1969.

[8] H H Bradley Jr. and F A Williams. Theory of radiant and hypergolic ignition of solid propellants. *Combustion Science and Technology*, 2(1):41–52, 1970.

[9] W Robert Mann and František Wolf. Heat transfer between solids and gases under nonlinear boundary conditions. *Quarterly of Applied Mathematics*, 9(2):163–184, 1951.

[10] Paul L Chambré. Nonlinear heat transfer problem. *Journal of Applied Physics*, 30(11):1683–1688, 1959.

[11] Andreas Acrivos and Paul L Chambré. Laminar boundary layer flows with surface reactions. *Industrial & Engineering Chemistry*, 49(6):1025–1029, 1957.

[12] A Brown. Diffusion of heat from a sphere to a surrounding medium. *Australian Journal of Physics*, 18(5):483–490, 1965.

[13] N Konopliv and E M Sparrow. Transient heat conduction in non-homogeneous spherical systems. *Wärme-und Stoffübertragung*, 3(4):197–210, 1970.

[14] Harry Bateman. *Tables of Integral Transforms, Vol. I*. McGraw-Hill, New York, 1954.

[15] David A Frank-Kamenetskii. Towards temperature distributions in a reaction vessel and the stationary theory of thermal explosion. In *Doklady Akademii Nauk SSSR*, volume 18, pages 411–412, 1938.

[16] Edmund Taylor Whittaker and George Neville Watson. *A Course of Modern Analysis*. Cambridge University Press, London, 1927.

[17] N N Semenov. The calculation of critical temperatures of thermal explosion. *Zeitschrift fur Physikalische Chemie*, 48:571–582, 1928.

[18] Robert M Corless, Gaston H Gonnet, David E G Hare, David J Jeffrey, and Donald E Knuth. On the lambert w function. *Advances in Computational Mathematics*, 5(1):329–359, 1996.

[19] D R Kassoy and J Poland. The subcritical spatially homogeneous explosion; initiation to completion. *Combustion Science and Technology*, 11(3-4):147–152, 1975.

[20] D R Kassoy and A Liñán. The influence of reactant consumption on the critical conditions

for homogeneous thermal explosions. *The Quarterly Journal of Mechanics and Applied Mathematics*, 31(1):99–112, 1978.

[21] D A Frank-Kamenetskii. The nonstationary theory of thermal explosion. *Zhurnal fizicheskoi khimii*, 20:139, 1946.

[22] Daniel Moreno-Boza, Immaculada Iglesias, and Antonio L Sánchez. Large-activation-energy analysis of gaseous reacting flow in pipes. *Combustion and Flame*, 178:217–224, 2017.

[23] David Al'bertovich Frank-Kamenetskii. *Diffusion and Heat Transfer in Chemical Kinetics*. Plenum Press, New York, 1969.

[24] Ya B Zeldovich, G I Barenblatt, V B Librovich, and G M Makhviladze. *The Mathematical Theory of Combustion and Explosions*. Consultants Bureau, New York, 1985.

[25] Dawei Zhang, Peng Zhang, Yueming Yuan, and Taichang Zhang. Hypergolic ignition by head-on collision of n, n, n', n'- tetramethylethylenediamine and white fuming nitric acid droplets. *Combustion and Flame*, 173:276–287, 2016.

# Part III

# Stability of convection flows on inclined surfaces

# Brief overview

The buoyancy-driven boundary-layer flow that develops over a semi-infinite inclined hot plate is known to become unstable at a finite distance from the leading edge, characterized by a critical value of the Grashof number *Gr* based on the local boundary-layer thickness. The nature of the resulting instability depends on the inclination angle $\phi$, measured from the vertical direction. For values of $\phi$ below a critical value $\phi_c$ the instability is characterized by the appearance of spanwise traveling waves, whereas for $\phi > \phi_c$ the bifurcated flow displays Görtler-like streamwise vortices. The Boussinesq approximation, employed in previous linear stability analyses, ceases to be valid for gaseous flow when the wall-to-ambient temperature ratio $\Theta_w$ is not close to unity. The corresponding non-Boussinesq analysis is presented in chapter 5, accounting also for the variation with temperature of the different transport properties. A temporal stability analysis including nonparallel effects of the base flow is used to determine curves of neutral stability, which are then employed to delineate the dependences of the critical Grashof number and of its associated wave length on the inclination angle $\phi$ and on the temperature ratio $\Theta_w$ for the two instability modes, giving quantitative information of interest for configurations with $\Theta_w - 1 \sim 1$. The analysis provides in particular the predicted dependence of the crossover inclination angle $\phi_c$ on $\Theta_w$, indicating that for gaseous flow with $\Theta_w - 1 \sim 1$ spanwise traveling waves are predominant over a range of inclination angles $0 \leq \phi \leq \phi_c$ that is significantly wider than that predicted in the Boussinesq approximation.

# Chapter 5

# Non-Boussinesq stability analysis of natural-convection gaseous flow on inclined hot plates

## 5.1 Introduction

A semi-infinite inclined hot plate placed in a quiescent air atmosphere is known to induce near its surface a free-convection flow as a result of the action of buoyancy forces on the heated gas. The structure of the resulting boundary layer away from the plate edge exhibits at leading order a self-similar structure, as first noted in the experimental study of Schmidt and Beckmann [1]. This boundary layer is known to become unstable to small disturbances at a certain distance measured from the leading edge of the plate [2]. The character of the observed instability depends on the inclination angle $\phi$, measured from the vertical direction. Thus, for values of $\phi$ above a critical value $\phi_c$, including in particular horizontal and nearly horizontal plates, the instability develops in the form of stationary counter-rotating vortex rolls that are oriented in the streamwise direction. These are similar to those characterizing the Görtler instability of boundary-layer

flow along a concave wall, driven by centrifugal forces, with the wall-normal component of the buoyancy force being the driving mechanism for free-convection flow. As the inclination angle $\phi$ is decreased, this wall-normal buoyancy component loses importance and, below a certain crossover angle $\phi_c$, the character of the observed instabilities changes to Tollmien-Schlichting-like traveling waves driven by shear. Following existing terminology [3, 4], in the following the stability mode involving streamwise stationary vortices will be termed *vortex instability*, whereas that involving traveling waves will be termed *wave instability*.

Sparrow & Husar [2] were the first to identify both modes experimentally, and to show that their prevalence depends on the inclination of the heated surface. The crossover angle was determined by Lloyd & Sparrow [5] to lie between $14^\circ < \phi_c < 17^\circ$. Other experiments carried out later agree generally with these findings [6–11].

Apart from the inclination angle $\phi$, the buoyancy-induced flow over a semi-infinite flat plate at constant temperature depends on the Prandtl number $Pr$ of the fluid and on the ratio $\Theta_w = T_w^*/T_\infty^*$ of the wall temperature to the ambient temperature. All previous theoretical efforts aimed at quantifying the critical conditions at the onset of the vortex and wave instabilities were performed in the Boussinesq approximation [3, 4, 12–20], which is only justified in gaseous flow when the wall-to-ambient relative temperature difference $(\Theta_w - 1)$ is small. Most of these studies employ linear local stability theory—a normal mode analysis—to determine, for fixed values of $Pr$ and $\phi$, the critical boundary-layer thickness $\delta_o^*$, measured in dimensionless form through a local Grashof number, above which small perturbations, either of vortex type with associated spanwise wave number $l^*$, or of wave type with streamwise wave number $k^*$, are amplified. In this manner, a unique neutral curve in the Grashof – wave number plane can be delineated for each mode. The mode with the lowest corresponding critical Grashof number for all wave numbers would be the one that prevails in an experiment, and the value of that Grashof number would give the local boundary-layer thickness—and therefore the distance $x^*$ to the plate edge—at which the instability first develops.

Conventionally, in a local stability analysis the base flow is assumed to be strictly parallel. That assumption must be reconsidered in the analysis of slowly varying slender flows, such as the present boundary layer, for which the order of magnitude of some of the terms in the stability equations, involving the transverse velocity component and the streamwise variation of the flow, is comparable to that of the viscous terms, and must be correspondingly taken into account. This so-called locally nonparallel approach was already adopted by Haaland & Sparrow in their temporal stability analyses of the vortex [3] and wave [4] instability modes. The resulting critical Grashof numbers were seen to differ by several orders of magnitude from those obtained with a strictly parallel analysis, thereby underlining the importance of the nonparallel terms. The problem was re-examined by a series of authors, adopting small variations of this approach, either in a temporal [12, 13, 15–19] or a spatial [14] linear–stability framework. The analysis can be extended to describe finite-amplitude vortex rolls and secondary bifurcations by retaining selected nonlinear terms in the description, as done by Chen *et al.* [19]. Recently, instabilities in transient cooling of inclined surfaces and cavities have been studied numerically [21, 22].

The accuracy of the computations mentioned above deteriorates in the presence of order–unity deviations of the wall temperature from the ambient temperature, when the use of the Boussinesq approximation is no longer justified. Although non-Boussinesq effects have been taken into account in analyses of the boundary-layer structure for flow over a heated plate [23–25], these effects have never been considered in connection with the associated stability problem. The objective of the present work is to revisit the classical work of Haaland & Sparrow [3, 4], including the influence of the wall-to-ambient temperature ratio $\Theta_w$ for cases with $\Theta_w - 1 \sim 1$. In particular, a linear temporal modal stability analysis will be performed to investigate both the vortex and the wave modes, with account taken of nonparallel effects associated with the slow downstream evolution of the base flow. The effect of $\Theta_w$ on the neutral stability curves will be assessed, along with the dependence of the crossover angle defining the transition between the two types of instability.

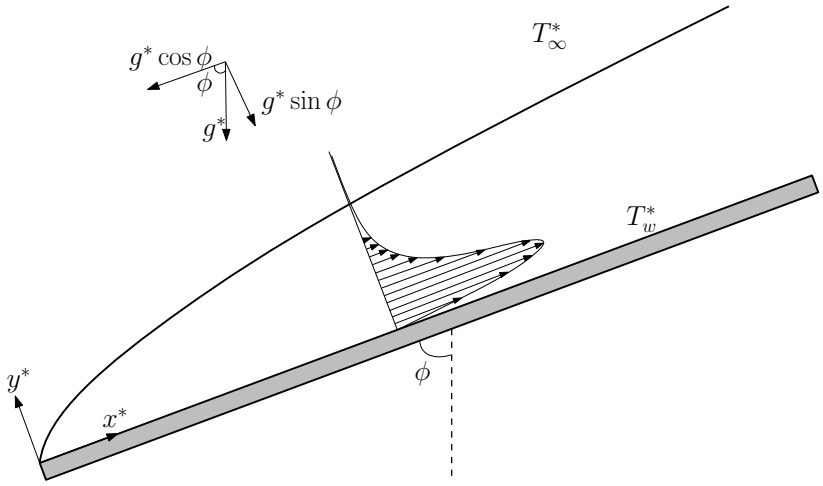


**Figure 5.1**: Schematic diagram of the boundary-layer flow over a heated inclined surface.

The study is structured as follows. The governing equations and boundary conditions for the base flow and for the linear stability analysis are given in § 2. The vortex mode is studied in § 3, followed in § 4 by the analysis of the wave instability. The predictions of the critical conditions for the two modes are compared in § 5 to delineate the boundary that defines the regions of prevalence of each mode on the parametric plane $\phi - \Theta_w$. Finally, concluding remarks are offered in § 6.

## 5.2 Problem formulation

The problem considered here, shown schematically in figure 5.1, involves the flow induced by buoyancy near the surface of a semi-infinite inclined plate whose temperature is held at a constant value, $T^*_w$, higher than the ambient temperature $T^*_\infty$ found in the surrounding quiescent air atmosphere. The associated velocities are negligibly small compared to the sound speed, so

that the conservation equations can be written in the low-Mach number approximation

$$\frac{\partial \rho^*}{\partial t^*} + \nabla^* \cdot (\rho^{**}) = 0, \tag{5.1}$$

$$\rho^* \frac{\partial^*}{\partial t^*} + \rho^{**} \cdot \nabla^{**} = -\nabla^* p^* + (\rho^* - \rho_\infty^*) g^* + \nabla^* \cdot \left[ \mu^* (\nabla^{**} + \nabla^{**T}) \right], \tag{5.2}$$

$$\rho^* \frac{\partial T^*}{\partial t^*} + \rho^{**} \cdot \nabla^* T^* = \frac{1}{Pr} \nabla^* \cdot (\mu^* \nabla^* T^*), \tag{5.3}$$

where $\rho^*$, $^*$, and $T^*$ represent the density, velocity, and temperature of the gas; dimensional quantities are indicated everywhere in the text with an asterisk $(^*)$. In the momentum equation (5.2), $p^*$ represents the sum of the pressure difference from the ambient hydrostatic distribution and the isotropic component of the stress tensor. Cartesian coordinates are used in the description, including the streamwise distance measured along the plate from the leading edge $x^*$, the transverse distance from the surface of the plate $y^*$, and the spanwise coordinate $z^*$, with corresponding velocity components $^* = (u^*, v^*, w^*)$. The inclination angle $\phi$ is measured from the vertical, so that the gravity vector is $g^* = -g^* \cos\phi \, e_x - g^* \sin\phi \, e_y$.

The above equations must be supplemented with the equation of state

$$\frac{\rho^*}{\rho_\infty^*} = \frac{T_\infty^*}{T^*} \tag{5.4}$$

and with the presumed power law

$$\frac{\mu^*}{\mu_\infty^*} = \frac{\kappa^*}{\kappa_\infty^*} = \left( \frac{T^*}{T_\infty^*} \right)^\sigma \tag{5.5}$$

for the temperature dependence of the viscosity and thermal conductivity, with the subscript $\infty$ denoting properties in the unperturbed ambient air. The constant values $Pr = 0.7$ and $\sigma = 2/3$, corresponding to air, will be used below for the Prandtl number $Pr = c_p^* \mu_\infty^* / \kappa_\infty^*$ in (5.3) and for

the exponent $\sigma$ in (5.5). Equations (5.1)–(5.3) must be integrated with the boundary conditions

$$\begin{cases} u^* = v^* = w^* = T^* - T_w^* = 0 & \text{at} \quad y^* = 0 \quad \text{for} \quad x^* > 0 \\ u^* = v^* = w^* = T^* - T_\infty^* = p^* = 0 & \text{as} \quad (x^{*2} + y^{*2}) \to \infty \quad \text{for} \quad y^* \neq 0, x^* > 0. \end{cases} \tag{5.6}$$

For plates that are not nearly horizontal, such that $\pi/2 - \phi$ is not small, the flow is driven by the direct acceleration associated with the gravity component parallel to the plate $g^* \cos\phi$. Near the leading edge of the plate there exists a nonslender Navier–Stokes region of characteristic size $[\nu_\infty^{*2}/(g^* \cos\phi)]^{1/3}$ where the velocity components are of order $(\nu_\infty^* g^* \cos\phi)^{1/3}$, with $\nu_\infty^* = \mu_\infty^*/\rho_\infty^*$ denoting the ambient kinematic viscosity, such that the local Reynolds number there is of order unity. Outside this Navier–Stokes region the flow–field structure includes a boundary-layer region of characteristic thickness $[(\nu_\infty^{*2} x^*)/(g^* \cos\phi)]^{1/4}$ and characteristic streamwise velocity $(g^* \cos\phi\, x^*)^{1/2}$, surrounded by an outer region of slow irrotational motion driven by the boundary-layer entrainment.

The stability of the boundary layer at a given location $x^* = x_o^*$ depends on the value of the associated Grashof number

$$Gr = \frac{x_o^*}{\delta_o^*} = \frac{\delta_o^{*3} g^* \cos\phi}{\nu_\infty^{*2}} = \left( \frac{x_o^{*3} g^* \cos\phi}{\nu_\infty^{*2}} \right)^{1/4}, \tag{5.7}$$

which is the Reynolds number based on the local values of the thickness and streamwise velocity

$$\delta_o^* = \left( \frac{\nu_\infty^{*2} x_o^*}{g^* \cos\phi} \right)^{1/4} \quad \text{and} \quad u_o^* = (g^* \cos\phi\, x_o^*)^{1/2}. \tag{5.8}$$

The following analysis assumes implicitly that the critical value of $Gr$ associated with the onset of the instability is moderately large, as corresponds to a location $x_o^*/\delta_o^* \gg 1$ far downstream from the Navier–Stokes region, where the flow near the plate surface is slender, enabling the stability analysis to be developed on the basis of the nearly parallel approximation, with the self-similar

boundary-layer solution used to evaluate the base flow, as indicated below.

### 5.2.1 Base flow

The near-plate solution that develops outside the Navier–Stokes region can be described with small relative errors of order $Gr^{-2}$ by using the boundary-layer form of the conservation equations. We shall neglect the pressure differences across the boundary layer, of order $\rho^*_\infty g^* \sin\phi\, \delta^*_o$, associated with the transverse component of the gravitational acceleration $g^* \sin\phi$, because they are small compared with the streamwise hydrostatic pressure differences $\rho^*_\infty g^* \cos\phi\, x^*_o$ at distances $x^*_o \gg \delta^*_o \tan\phi$, corresponding to local values of the Grashof number

$$Gr \gg \tan\phi, \tag{5.9}$$

a condition readily satisfied outside the Navier–Stokes region for the inclined plates with $\pi/2 - \phi \sim 1$ considered here. The resulting solution is self-similar when expressed in terms of the dimensionless coordinate

$$\eta = \frac{y^*}{[(\nu^{*2}_\infty x^*)/(g^* \cos\phi)]^{1/4}} \tag{5.10}$$

with use made of the nondimensional temperature and stream function

$$\Theta(\eta) = \frac{T^*}{T^*_\infty} \quad \text{and} \quad F(\eta) = \frac{\psi^*}{\left(x^{*3} \nu^{*2}_\infty g^* \cos\phi\right)^{1/4}}, \tag{5.11}$$

with associated self-similar velocity components

$$U = \frac{u^*}{(g^* \cos\phi\, x^*)^{1/2}} = \Theta F' \quad \text{and} \quad V = \frac{v^*}{(\nu^{*2}_\infty g^* \cos\phi / x^*)^{1/4}} = \frac{\Theta}{4}\left(\eta F' - 3F\right). \tag{5.12}$$

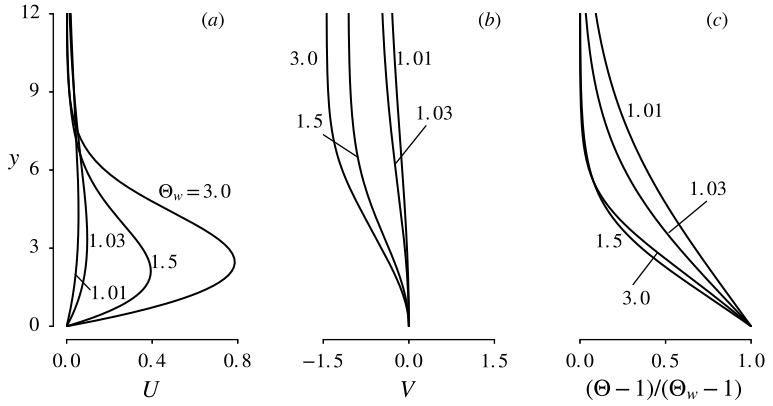


**Figure 5.2**: The self-similar base-flow solution obtained by integration of (5.13)–(5.14) with $Pr = 0.7$ and $\sigma = 2/3$ for different values of $\Theta_w$.

Here the prime is used to denote differentiation with respect to $\eta$. Introducing these variables reduces the problem to that of integrating

$$(\Theta^\sigma(\Theta F')')' + \frac{3}{4}F(\Theta F')' - \frac{1}{2}\Theta F'^2 + 1 - \frac{1}{\Theta} = 0, \tag{5.13}$$

$$(\Theta^\sigma \Theta')' + \frac{3}{4}PrF\Theta' = 0, \tag{5.14}$$

with boundary conditions $F(0) = F'(0) = F'(\infty) = \Theta(0) - \Theta_w = \Theta(\infty) - 1 = 0$, where $\Theta_w = T_w^*/T_\infty^*$ is the wall-to-ambient temperature ratio.

The numerical integration was performed using a spectral collocation method with a fractional transformation defined by $y = a(1+\xi)/(b-\xi)$ [26], where $a = y_c y_{\max}/(y_{\max} - 2y_c)$ and $b = 1 + 2a/y_{\max}$, that maps $N$ Chebyshev collocation points $\xi \in [-1,1]$ to the physical domain $y \in [0, y_{\max}]$ allocating $N/2$ collocation points to the near-wall region $0 < y < y_c$. Values $y_{\max} = 200$, $y_c = 15$ and $N = 128$ are found to be adequate, slightly higher than the values used in [20] for spatial analysis. Resulting temperature and velocity profiles are shown in figure 5.2 for different values of $\Theta_w$, giving results similar to those presented elsewhere [25].

### 5.2.2 Linear stability analysis

Using standard practice, the linear stability of the flow at $x^* = x_o^*$ is investigated by introducing into (5.1)–(5.5) the perturbed nondimensional variables

$$\begin{aligned}
\frac{\overset{*}{}}{u_o^*} &= (x/Gr, y) + (x, y, z, t) = (\bar{u}, \bar{v}, 0) + (u, v, w) \\
\frac{T^*}{T_\infty^*} &= \overline{T}(x/Gr, y) + \theta(x, y, z, t) \\
\frac{\rho^*}{\rho_\infty^*} &= \bar{\rho}(x/Gr, y) + \rho(x, y, z, t) \\
\frac{\mu^*}{\mu_\infty^*} &= \bar{\mu}(x/Gr, y) + \mu(x, y, z, t) \\
\frac{p^*}{\rho_\infty^* u_o^{*2}} &= p(x, y, z, t)
\end{aligned} \tag{5.15}$$

where

$$x = \frac{x^* - x_o^*}{\delta_o^*},\ y = \frac{y^*}{\delta_o^*},\ z = \frac{z^*}{\delta_o^*}, \quad \text{and} \quad t = \frac{t^*}{\delta_o^*/u_o^*}, \tag{5.16}$$

leading to the linearized equations

$$\frac{\partial \rho}{\partial t} = -\bar{\rho}\,\nabla\cdot - \rho\,\nabla\cdot - \cdot\nabla\bar{\rho} - \cdot\nabla\rho, \tag{5.17}$$

$$\begin{aligned}
\bar{\rho}\,\frac{\partial}{\partial t} &= -\bar{\rho}\cdot\nabla - \bar{\rho}\cdot\nabla - \rho\cdot\nabla - \nabla p - \frac{1}{Gr}\rho(e_x + \tan\phi\, e_y) \\
&\quad + \frac{1}{Gr}\nabla\cdot\left[\bar{\mu}(\nabla + \nabla^T) + \mu(\nabla + \nabla^T)\right],
\end{aligned} \tag{5.18}$$

$$\begin{aligned}
\bar{\rho}\,\frac{\partial \theta}{\partial t} &= -\bar{\rho}\cdot\nabla\theta - \bar{\rho}\cdot\nabla\overline{T} - \rho\cdot\nabla\overline{T} \\
&\quad + \frac{1}{Gr\,Pr}\nabla\cdot\left[\bar{\mu}\nabla\theta + \mu\nabla\overline{T}\right],
\end{aligned} \tag{5.19}$$

and

$$\rho = -\overline{T}^{-2}\theta \qquad \text{and} \qquad \mu = \sigma\overline{T}^{\sigma-1}\theta. \tag{5.20}$$

The base profiles , $\overline{T}$, $\bar{\rho}$, and $\bar{\mu}$ can be evaluated from the self-similar velocity and temperature profiles $U(\eta)$, $V(\eta)$, and $\Theta(\eta)$ according to

$$\begin{aligned}
\bar{u} &= (1+x/Gr)^{1/2}\,U(y/[1+x/Gr]^{1/4}),\\
\bar{v} &= Gr^{-1}(1+x/Gr)^{-1/4}\,V(y/[1+x/Gr]^{1/4}),\\
\overline{T} &= \frac{1}{\bar{\rho}} = \bar{\mu}^{1/\sigma} = \Theta(y/[1+x/Gr]^{1/4}),
\end{aligned} \tag{5.21}$$

written in terms of the local coordinates $x = (x^* - x_o^*)/\delta_o^*$ and $y = y^*/\delta_o^*$ by using $\eta = y/(1+x/Gr)^{1/4}$ and $Gr = x_o^*/\delta_o^*$. As can be seen, the base flow displays a slow streamwise variation through the rescaled coordinate $x/Gr$. The expressions given above can be used to evaluate the factors that appear in the linearized equations (5.17)–(5.19). In the first approximation for $Gr \gg 1$ one obtains the order-unity factors

$$\begin{aligned}
&\bar{u} = U(y), \frac{\bar{u}}{y} = U'(y), \frac{^2\bar{u}}{y^2} = U''(y),\\
&\overline{T} = \frac{1}{\bar{\rho}} = \bar{\mu}^{1/\sigma} = \Theta(y), \frac{\overline{T}}{y} = \Theta'(y), \frac{^2\overline{T}}{y^2} = \Theta''(y),
\end{aligned} \tag{5.22}$$

which pertain to the strictly parallel flow, along with the factors of order $Gr^{-1}$

$$\begin{aligned}
&\bar{v} = Gr^{-1}V(y),\ \frac{\bar{v}}{y} = Gr^{-1}V'(y), \frac{\bar{u}}{x} = Gr^{-1}\left[\frac{1}{2}U(y) - \frac{y}{4}U'(y)\right],\\
&\frac{\overline{T}}{x} = -Gr^{-1}\frac{y}{4}\Theta'(y), \quad \text{and} \quad \frac{\bar{\rho}}{x} = Gr^{-1}\frac{y}{4}\frac{\Theta'(y)}{\Theta^2(y)},
\end{aligned} \tag{5.23}$$

arising from nonparallel effects.

The nearly parallel stability analysis performed here assumes implicitly a moderately small value of $Gr^{-1}$, a condition needed to ensure the slenderness of the flow. The small parameter $Gr^{-1}$ appears in (5.17)–(5.19) directly as a factor in the molecular transport terms in (5.18) and (5.19) and also through the factors (5.23) associated with the slow streamwise variation of the base flow.

If only terms of order unity are retained in (5.17)–(5.19), then the resulting equations describe the inviscid instability of strictly parallel flow. By retaining also terms of order $Gr^{-1}$ one accounts simultaneously for viscous and nonparallel effects, that being the approach pursued herein. Thus, following Haaland & Sparrow [3, 4], the equations (5.17)–(5.19) were systematically simplified by retaining terms up to $O(Gr^{-1})$, while neglecting terms of order $Gr^{-2}$ and higher. The resulting simplified equations are written in 5.6 for the normal-mode perturbations

$$[u,v,w,p,\theta,\rho,\mu](x,y,z,t) = \mathrm{e}^{\mathrm{i}(kx+lz-\omega t)}[\hat{u},\hat{v},\hat{w},\hat{p},\hat{\theta},\hat{\rho},\hat{\mu}](y), \tag{5.24}$$

where $k$ and $l$ are the dimensionless streamwise and spanwise wave numbers, and $\omega = \omega_\mathrm{r} + \mathrm{i}\,\omega_\mathrm{i}$ contains both the frequency $\omega_\mathrm{r}$ and the growth rate $\omega_\mathrm{i}$ of the perturbations. The vortex instability is associated with modes with $k = 0$ and $\omega_\mathrm{r} = 0$, whereas the wave instability corresponds to $l = 0$ and $\omega_\mathrm{r} > 0$. The two types of instabilities will be studied separately in the following two sections.

## 5.3 Vortex instability

### 5.3.1 The simplified eigenvalue problem

We start by considering instabilities characterized by the appearance of Görtler-like vortex rolls aligned with the streamwise direction, known to dominate the boundary-layer dynamics for values of $\phi$ above a critical value $\phi_c$. These can be investigated by setting $k = 0$ in the normal-mode ansatz (5.24). Chen *et al.* [19] showed that the principle of exchange of instabilities holds for this type of instabilities, in the sense that in the full eigenvalue spectrum the eigenvalue with the largest growth rate $\omega_i$ has zero frequency $\omega_\mathrm{r} = 0$. Hence, the critical conditions for vortex instability can be computed by setting both $k$ and $\omega$ equal to zero in (5.34)–(5.38). Eliminating

then $\hat{p}$ and $\hat{w}$ by combining equations (5.34), (5.36) and (5.37), and introducing the transformation

$$\tilde{u} = \hat{u}\tan\phi, \quad \tilde{v} = \hat{v}, \quad \tilde{\theta} = \hat{\theta}\tan\phi, \quad = Gr\tan\phi \tag{5.25}$$

to remove the explicit dependence on the inclination angle $\phi$ [3], leads to the three equations

$$\begin{aligned}
&\left[\mathrm{D}(\Theta^{\sigma}\mathrm{D}) - (V/\Theta)\mathrm{D} - (2U - yU')/(4\Theta)\right]\tilde{u} \\
&+ \left\{\left[1 + VU' + U(2U - yU')/4\right]/\Theta^2 + \sigma\Theta^{\sigma-1}(U'\mathrm{D} + U'')\right\}\tilde{\theta} = \frac{U'}{\Theta}\tilde{v}, \qquad (5.26)\\
&\mathrm{D}\left[\frac{1}{l^2}\left(\mathrm{D}\Theta^{\sigma} - \frac{V}{\Theta}\right)\mathrm{D}\left(\mathrm{D} - \frac{\Theta'}{\Theta}\right) + \mathrm{D}\Theta^{\sigma} - 2\Theta^{\sigma}\left(2\mathrm{D} - \frac{\Theta'}{\Theta}\right)\right]\tilde{v} \\
&+ \left[\Theta^{\sigma}\mathrm{D}\left(\mathrm{D} - \frac{\Theta'}{\Theta}\right) + \frac{1}{\Theta}(\mathrm{D}V) + \Theta^{\sigma}l^2\right]\tilde{v} - \Theta^{-2}\tilde{\theta} = 0, \qquad (5.27)\\
&\left[\mathrm{D}(\Theta^{\sigma}\mathrm{D}) + \sigma(\mathrm{D}\Theta^{\sigma-1}\Theta') - Pr\frac{V}{\Theta}\mathrm{D} - \Theta^{\sigma}l^2 - Pr\left(\frac{y}{4}U - V\right)\frac{\Theta'}{\Theta^2}\right]\tilde{\theta} \\
&+ Pr\frac{y\Theta'}{4\Theta}\tilde{u} = Pr\frac{\Theta'}{\Theta}\tilde{v}, \qquad (5.28)
\end{aligned}$$

with boundary conditions

$$\tilde{u} = \tilde{v} = \mathrm{D}\tilde{v} = \tilde{\theta} = 0 \quad \text{at } y = 0 \text{ and as } y \to \infty. \tag{5.29}$$

In the operators acting on the eigenfunctions the symbol D denotes differentiation with respect to $y$. A function of $y$ placed immediately after D indicates that multiplication by that function should be performed prior to differentiation, so that, for instance, $(\mathrm{D}\Theta^{\sigma})\tilde{v} = \mathrm{d}(\Theta^{\sigma}\tilde{v})/\mathrm{d}y$, while $(\Theta^{\sigma}\mathrm{D})\tilde{v} = \Theta^{\sigma}\mathrm{d}\tilde{v}/\mathrm{d}y$ instead. The eigenfunction $\tilde{u}$ is coupled to $\tilde{v}$ and $\tilde{\theta}$ through the last term on the left-hand side in (5.28), associated with the slow streamwise variation of the base temperature $\overline{T}$. Also of interest is that for strictly parallel flow (i.e., when the factors listed in (5.23) are set equal to zero), the problem becomes independent of the base velocity field, and the resulting equations reduce to those corresponding to Rayleigh-Bénard convection.

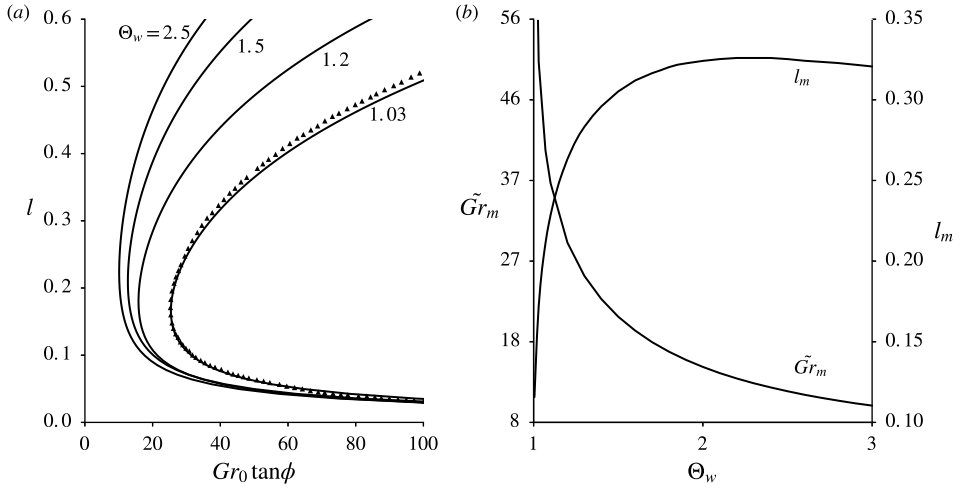


**Figure 5.3**: Results of the non-Boussinesq analysis of the vortex instability, including curves of neutral stability (a) along with the variation with $\Theta_w$ of $_m$ and of the associated spanwise wave number $l_m$ $(b)$; the triangles in $(a)$ corresponds to evaluations of (5.30) with the values of $Gr_{\mathrm{B}}$ reported in [3].

### 5.3.2 Numerical results

For a given wall-to-ambient temperature ratio $\Theta_w$, which defines the base flow, and a given spanwise wave number $l$, the above eigenvalue problem (5.26)–(5.29) was solved numerically to determine the critical value $_0$ of  identifying the conditions of neutral stability. The variation of $_0 = \tan\phi\, Gr_0$ with $l$ is shown in figure $5.3(a)$ for different $\Theta_w$. As can be seen, each neutral curve $_0(l)$ reaches a minimum value $_0 =_m$ at $l = l_m$. This minimum determines the wave length $2\pi/l_m$ of the most unstable mode along with the downstream location $x^*_m = (_m/\tan\phi)^{4/3}[\nu^{*2}_\infty/(g^*\cos\phi)]$ at which the vortices begin to develop. To complete the description, the variation of $_m$ and $l_m$ for the most unstable mode is plotted as a function of $\Theta_w$ in figure $5.3(b)$. It is evident from the plots that increasing the wall-to-ambient temperature ratio $\Theta_w$ as well as increasing $\phi$ towards a more horizontal position tends to destabilize the flow. Also noteworthy is the rapid variation of $_m$ and $l_m$ with $\Theta_w$ for $\Theta_w - 1 \ll 1$.

### 5.3.3 Departures from the Boussinesq approximation

The results can be compared to the Boussinesq analysis of Haaland & Sparrow [3] by taking a wall-to-ambient temperature ratio $\Theta_w$ close to unity. The Boussinesq Grashof number employed in [3], $Gr_{\rm B} = [\beta^*(T_w^* - T_\infty^*)x^{*3}g^*\cos\phi/\nu_\infty^{*2}]^{1/4}$, is related to that defined in (5.7) by $Gr_{\rm B} = Gr[\beta^*(T_w^* - T_\infty^*)]^{1/4}$. The result depends on the temperature used to evaluate the coefficient of thermal expansion $\beta^*$, given for an ideal gas by $\beta^* = 1/T^*$. Thus, using the ambient temperature to evaluate $\beta_\infty^* = 1/T_\infty^*$ yields

$$Gr_w = Gr_{\rm B}(\Theta_w - 1)^{-1/4} \tag{5.30}$$

whereas the expression

$$Gr_\infty = Gr_{\rm B}(1 - \Theta_w^{-1})^{-1/4} \tag{5.31}$$

is obtained by using the wall temperature to evaluate $\beta_w^* = 1/T_w^*$. Clearly, the temperature selected to define $\beta^*$ becomes irrelevant for $\Theta_w - 1 \ll 1$, when the relative differences between both expressions are of order $(\Theta_w - 1)/4$. Equation (5.30) is selected in the comparison of figure 5.3$(a)$ to evaluate the neutral curve for $\Theta_w = 1.03$ using the values of $Gr_{\rm B}$ reported in Haaland & Sparrow [3], giving the results represented by the triangles.

As can be seen in figure 5.3$(a)$, the differences between the predictions obtained with the Boussinesq approximation and those accounting for non-Boussinesq effects are very small for $\Theta_w = 1.03$, with departures in resulting values of $_m$ and $l_m$ of the order of 1%. The departures are expected to become larger for increasing values of $\Theta_w - 1$, with the two expressions (5.30) and (5.31) leading to increasingly different values of $Gr$. This is tested in figure 5.4 by comparing the curve $_m - \Theta_w$ obtained from the numerical integrations of (5.26)–(5.29), given previously in figure 5.3$(b)$, with the predictions derived by extending the Boussinesq approximation with use made of (5.30) and (5.31) evaluated with $Gr_{\rm B} = 10.5$, the latter obtained by dividing the value 29.6 reported in [3] by $2\sqrt{2}$, as is needed to account for the factor 4 used in their definition of

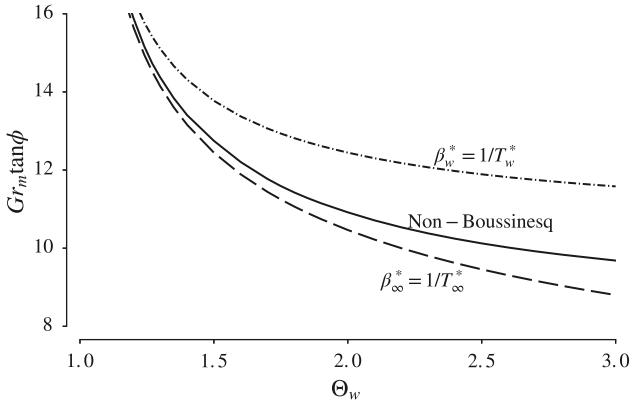


**Figure 5.4**: The variation of $Gr_m \tan\phi$ with $\Theta_w$ obtained from integrations of the non-Boussinesq eigenvalue problem (5.26)–(5.29) (solid curve) and from the Boussinesq predictions (5.30) and (5.30) evaluated with $Gr_{\mathrm{B}} = 10.5$, obtained by scaling the value given in [3], as indicated in the text.

the boundary-layer thickness $\delta^*$. As can be seen, our results lie between the two Boussinesq predictions, with the thermal expansion based on the ambient temperature $\beta_\infty^* = 1/T_\infty^*$ giving better agreement. For the vortex mode, it is apparent from the curves in the figure that straightforward extension of the stability results computed in the Boussinesq approximation by use of (5.31) provides sufficiently accurate predictions for the critical Grashof number even for configurations with $\Theta_w - 1 \sim 1$. As seen below, the wave mode analyzed next is different in this connection, in that the sharp decrease in $_m$ found for increasing $\Theta_w$ cannot be predicted by simply extending the results of the Boussinesq approximation, regardless of the temperature used in evaluating the thermal–expansion coefficient.

## 5.4 Wave instability

The wave instability on hot inclined plates has received significantly less attention [4, 14, 16, 20] than the related vortex instability problem, possibly because for Boussinesq flow its occurrence its restricted to a moderately small angle range $0^\circ < \phi \lesssim 20^\circ$ about the vertical position. In this connection, it is worth anticipating that the present analysis will show that this

range widens significantly for non-Boussinesq gaseous flow with $\Theta_w - 1 \sim 1$.

### 5.4.1 The simplified eigenvalue problem

In accordance with Squire's theorem, only two-dimensional disturbances need to be considered below, so that $l = 0$ in (5.24). Although a spatial stability analysis is needed to accurately determine the downstream growth rate of the disturbance [14, 20], the present work focuses on the determination of the curves of neutral stability, associated with real values of both the wave number $k$ and the frequency $\omega$, which can be obtained with a simpler temporal stability analysis.

With $l = 0$ the problem simplifies, in that the solution for $\hat{u}$, $\hat{v}$, $\hat{p}$, and $\hat{\theta}$ becomes independent of $\hat{w}$, so that the eigenvalue problem reduces to the solution of (5.34)–(5.36) and (5.38) with the homogeneous boundary conditions

$$\hat{u} = \hat{v} = \hat{\theta} = 0 \text{ at } y = 0, \quad \text{and} \quad \hat{u}, \hat{v}, \hat{\theta}, \hat{p} \to 0 \text{ as } y \to \infty. \tag{5.32}$$

The eigenvalue nature of this problem becomes more apparent by casting the equations in the standard form $Af = \omega Bf$, with $A$ and $B$ being linear differential operators acting on $f = (\hat{u}, \hat{v}, \hat{p}, \hat{\theta})$. As a result of the non-Boussinesq character of the continuity equation, elimination of $\hat{p}$ and $\hat{u}$ by linear combinations leads to a quadratic eigenvalue problem for the eigenvalue $\omega$, which is not further considered here because of the additional complications involved in its numerical solution.

### 5.4.2 Critical curves of neutral stability

Results obtained by integrating numerically the eigenvalue problem for the wave instability are shown in figure 5.5. Unlike the vortex instability, for which the dependence on the inclination angle can be scaled out of the equations by the transformation (5.25), thereby reducing the parametric dependence of the results, the eigenvalue problem for the wave instability depends

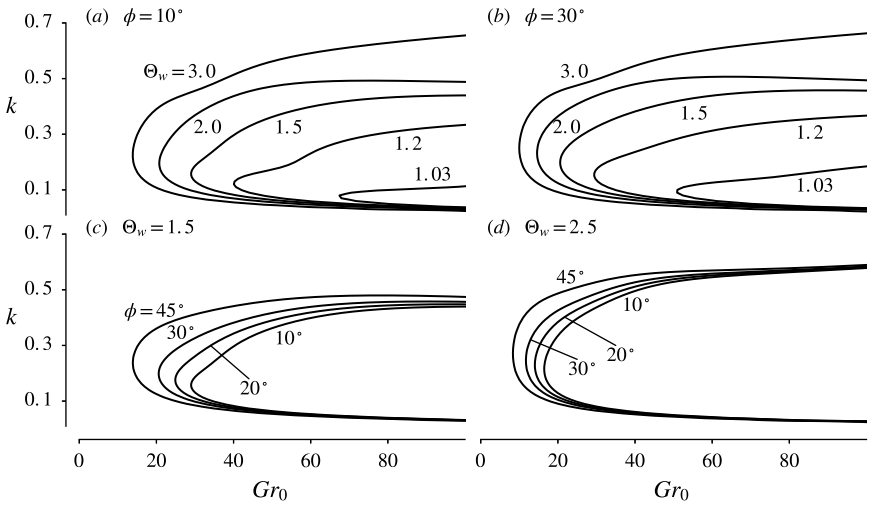


**Figure 5.5**: Curves of neutral stability for the wave mode with different wall-to-ambient temperature ratios $\Theta_w$ and different inclination angles $\phi$.

on both $\phi$ and $\Theta_w$. Curves of neutral stability are plotted in figures $5.5(a)$ and $5.5(b)$ for a fixed inclination angle $\phi$ and different values of the wall temperature ratio $\Theta_w$, with corresponding curves for fixed $\Theta_w$ and different values of $\phi$ given in figures $5.5(c)$ and $5.5(d)$. Just as for the vortex instability, increasing the wall-to-ambient temperature ratio, as well as increasing the inclination angle (a more horizontal plate) has a destabilizing effect on the flow. The rapid change in the neutral curves shown in the upper plots of the figure as the wall temperature increases from $\Theta_w = 1.03$ to $\Theta_w = 1.2$ is indicative of the importance of non-Boussinesq effects for wave instability.

### 5.4.3 Stability predictions based on vorticity–stream function formulation

Before continuing the discussion of results, it is worth commenting on the differences arising from the use of different starting conservation equations in the presence of a slowly varying base flow. Unlike many previous analyses, which were derived on the basis of a vorticity–stream function formulation, the present analysis employs as a starting point the conservation equations written in primitive variables. Although the logical expectation is that both approaches yield the

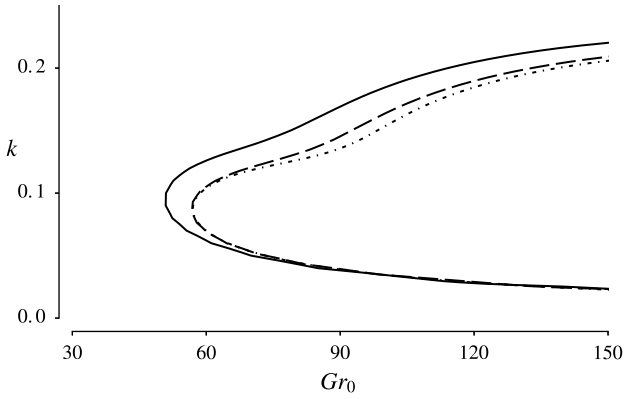


**Figure 5.6**: Curves of neutral stability for the wave instability with $\Theta_w = 1.03$ and $\phi = 30^\circ$ obtained from (5.34), (5.38) and (5.33) (solid curve) and by repeating the computations with the underlined term removed in (5.33) (dashed curve); the dotted curve corresponds to evaluations of (5.30) reported in [4].

same results, that being the case for strictly parallel base flow, small but noticeable discrepancies were found between both computational approaches when the nonparallel terms are retained for the base flow. This is so because when the pressure is eliminated from the equations written in primitive variables *after* the normal mode decomposition is introduced, i.e. from equations (5.34)–(5.38), to obtain a normal-mode vorticity form, the resulting set of equations is not identical to that obtained by writing the momentum equation in terms of the vorticity *before* introducing the normal mode decomposition. This discrepancy does not happen when analyzing the vortex mode, because the direction of the vorticity differs between the base flow and the perturbations, i.e. the base-flow vorticity is oriented along the spanwise direction while the perturbed vorticity is oriented along the streamwise direction.

These differences can be illustrated by comparing the results of our formulation for $\Theta_w \ll 1$ with those obtained earlier by Haaland & Sparrow [4] using the linearized vorticity–stream function Boussinesq formalism presented earlier in [27]. The comparison can be readily established by writing our equations (5.35) and (5.36) for $\Theta_w - 1 \ll 1$ followed by elimination of

the pressure to yield

$$[\mathrm{D}^3 - V\mathrm{D}^2 - Gr\,\mathrm{i}(Uk-\omega)\mathrm{D} - k^2\mathrm{D} + V'']\hat{u}$$
$$[-\mathrm{i}k\mathrm{D}^2 + \mathrm{i}kV\mathrm{D} - Grk(Uk-\omega) - GrU'' + \mathrm{i}k^3 + \underline{\mathrm{i}kV'}]\hat{v} + [\mathrm{D} - \mathrm{i}k\tan\phi]\hat{\theta} = 0 \qquad (5.33)$$

after the continuity equation is used to simplify the result. Comparing the above equation with equation (15) in [27] reveals that both are identical, except for the underlined term in (5.33), which is absent in [27], that being a consequence of the different derivation procedure. As previously mentioned, the missing term, proportional to the transverse gradient of the transverse base velocity, would be absent for strictly parallel flow. Its quantitative importance is assessed in figure 5.6, where the neutral curve obtained using (5.34) and (5.38) together with (5.33) (solid curve) is compared with that obtained after selectively removing the term $\mathrm{i}kV'$ in (5.33) (dashed curve). The additional term is seen to destabilize the flow, resulting in critical Grashof numbers that are about 10% smaller than those obtained on the basis of the vorticity–stream function formulation. As expected, the dashed curve is seen to agree with that obtained by evaluating (5.30) with the values of $Gr_{\mathrm{B}}$ reported in Haaland & Sparrow [4] for $\phi = 30^{\mathrm{o}}$, represented by a dotted line in figure 5.6.

### 5.4.4 Quantitative assessment of non-Boussinesq effects

To complete the description, the Boussinesq predictions (5.30) and (5.31) are compared in figure 5.7 with the results of the non-Boussinesq eigenvalue problem for $\phi = 30^{\mathrm{o}}$. The value $Gr_{\mathrm{B}} = 21.11$ used in the evaluations of (5.30) and (5.31) is extracted from our numerical results for $\Theta_w - 1 \ll 1$. Because of the discrepancies illustrated in figure 5.6, this value is somewhat smaller than the value reported in [4], which gives $Gr_{\mathrm{B}} = 23.63$ once corrected to account for differences in their definition of $\delta^*$. As can be seen in figure 5.7, the extrapolations of the Boussinesq results consistently overpredict the critical Grashof number. This is so because

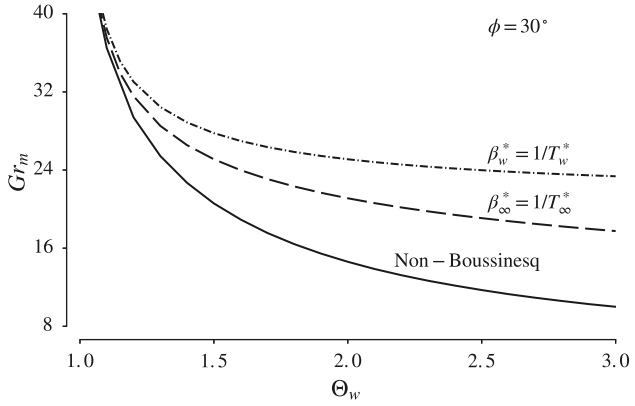


**Figure 5.7**: The variation of $Gr_m$ with $\Theta_w$ for $\phi = 30^\circ$ obtained for the wave instability from integrations of the non-Boussinesq eigenvalue problem (solid curve) and from the Boussinesq predictions (5.30) and (5.31) evaluated with $Gr_B = 17.96$, the latter computed by extrapolating the numerical results as $\Theta_w \to 1$.

the Boussinesq approximation does not describe accurately the acceleration of the light gas for increasing $\Theta_w$, which is apparent in the velocity profiles in figure 5.2, resulting in augmented shear stresses that trigger the wave–mode instability.

## 5.5 Variation of the crossover angle

It is apparent from the comparison of the curves in figures 5.4 and 5.7 that non-Boussinesq effects have a larger influence on the wave mode than they have on the vortex mode. For both modes, increasing the plate temperature promotes instability by decreasing the associated critical Grashof number, but the decrease of $Gr_m$ is much more pronounced for the wave mode, thereby suggesting that the character of the instability that develops over a plate at a given inclination angle may switch from a vortex mode to a wave mode as the plate temperature increases.

To investigate this aspect of the problem we compare in figure 5.8$(a)$ the curves $Gr_m = {}_m / \tan\phi$ corresponding to the vortex mode, with ${}_m(\Theta_w)$ given in figure 5.3$(b)$, with the values of $Gr_m$ obtained from the turning points of the neutral curves computed for the wave mode for a fixed value of $\Theta_w$, given for instance in figure 5.5$(c)$ for the particular case $\Theta_w = 1.5$. The

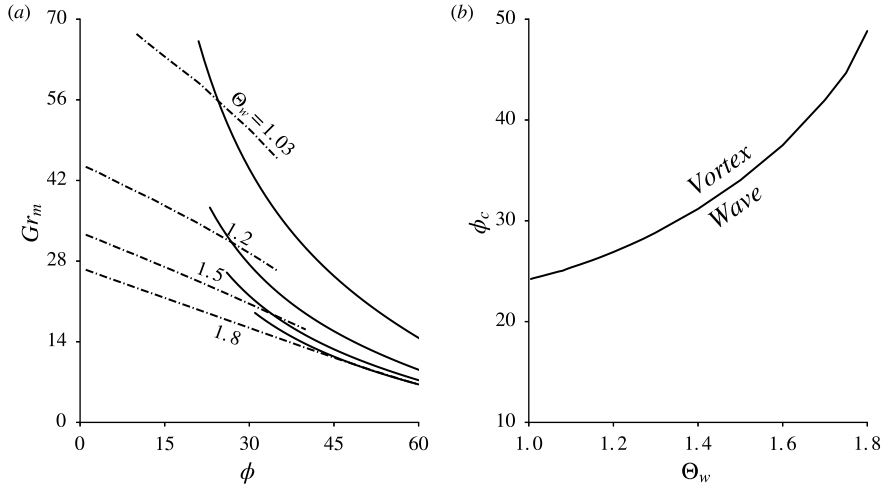


**Figure 5.8**: The left-hand-side plot represents the variation of $Gr_m$ with $\phi$ for the wave mode (dashed curves) and for the vortex mode (solid curves) for different values of $\Theta_w$, while the right-hand-side plot gives the variation with $\Theta_w$ of the crossover angle $\phi_c$ at which each pair of curves crosses.

crossing point of each pair of curves determines the angle $\phi_c$ at which the character of the most unstable mode changes from a traveling wave (for $\phi < \phi_c$) to stationary streamwise vortices (for $\phi > \phi_c$). The resulting crossover angle increases for increasing $\Theta_w$, as shown in figure 5.8$(b)$, which delineates the parametric regions where each one of the modes prevails.

Our linear stability analysis predicts a crossover angle $\phi_c = 23.8^\circ$ for $\Theta_w - 1 \ll 1$, in agreement with the value $\phi_c = 22^\circ$ reported in previous linear stability analyses [15, 16] using instead the scalings of the horizontal boundary layer for the self-similar base flow. A somewhat smaller value was estimated in the work of Kahawita and Meloney [13] by evaluating approximately the critical Grashof number of the wave mode from the results of the vertical plate through simple multiplication by $\cos\phi$. It is worth noting that the values observed in experiments are typically somewhat smaller than the theoretical predictions (e.g., values in the range $14^\circ < \phi_c < 17^\circ$ are reported in the early work [5]). The deviations are attributable to the limitations of the linear analysis performed here, although more work is needed to clarify this issue.

As the value of $\Theta_w$ increases the crossing points of the curves in figure 5.8$(a)$ moves to the right, corresponding a wider range $0 \leq \phi < \phi_c$ where the wave mode prevails. Unexpectedly, the

two curves $Gr_m - \phi$ become tangent at $\Theta_w \simeq 1.8$ and exhibit no crossing point for larger values of $\Theta_w > 1.8$, for which our analysis predicts the wave mode to be dominant for all angles. Clearly, however, this prediction would need to be reconsidered for near-horizontal plates with values of $\phi$ approaching $\pi/2$, for which the condition (5.9), used in deriving the governing equations for the inclined plate, would no longer hold. A revised stability analysis, accounting for transverse pressure differences across the boundary layer in deriving the governing equations for both the base flow and its perturbations, would be needed to assess the transition between both instability modes for very hot plates with $\Theta_w > 1.8$.

## 5.6 Concluding remarks

Although the existing experimental evidence and the previous theoretical predictions based on the Boussinesq approximation indicate that at higher wall temperatures the flow tends to become unstable at lower values of the Grashof number, corresponding to smaller downstream distances from the plate edge, quantitative results for relative wall-to-ambient temperature differences of order unity are not currently available. This study provides the needed quantification on the basis of a non-Boussinesq temporal stability analysis accounting for the slow variation of the base flow. The results provide predictions of critical Grashof numbers for both modes of instability and their associated wave numbers. While non-Boussinesq effects are found to have only a moderate quantitative effect on the instability mode involving streamwise vortices, it is found that the augmented shear resulting from the flow acceleration in the presence of large density differences promotes wave instabilities significantly. As a result, the range of angles about the vertical position where the wave mode is dominant is predicted to increase substantially with increasing wall temperatures, a finding of our linear stability analysis that warrants future experimental investigation.

The characteristics of the analysis presented, both linear and local, limit the accuracy of

some of the predictions. For instance, the nonlinear growth of the perturbations, not described herein, may explain the discrepancies between the predicted value of $\phi_c = 23.8^\circ$ for $\Theta_w - 1 \ll 1$ and previous experimental observations. Also, although the analysis accounts for the slow streamwise variation of the base flow in (5.15), the shape functions of the accompanying perturbations, as well as the wave numbers $k$ and $l$ are not allowed to depend on the rescaled coordinate $x/Gr$, as would be needed to account for their downstream evolution. Incorporating the latter, while still taking advantage of the slenderness of the boundary-layer flow associated with moderately large values of the Grashof number—thus retaining only terms up to $\mathcal{O}(Gr^{-1})$—would turn the *local* stability problem into a *nonlocal* parabolic stability problem that has to be integrated in the downstream direction. In this type of treatment a unique neutral curve cannot be defined since the streamwise development depends strongly on the initial conditions that are imposed at a certain location, as pointed out for the first time by Hall [28] for the related problem of Görtler instability over a curved wall. Subsequent studies [29] have found that, although different initial conditions result in different growth rates during the transient stage, at very large downstream distances the local growth rate is found to be independent of the initially imposed disturbance. Although an attempt to apply these concepts to the present problem was made by Tumin [20], more work is clearly needed to further clarify the instability characteristics of natural-convection flows.

A global stability analysis of the natural-convection flow under consideration, in which the instabilities are considered as two-dimensional temporal Fourier modes, is also worth pursuing in future work. Since this alternative approach does not invoke the slenderness condition of the basic flow, it might prove useful to study cases with very large wall-to-ambient temperature ratios, for which, as shown in the present work, the instability sets in at smaller Grashof numbers, and thus at shorter distances from the leading edge. The highly nonparallel Navier-Stokes region close the edge of the plate then may play an important role in these early transition events.

This chapter, in part, has been published in *International Journal of Heat and Mass*

*Transfer*, "Non-Boussinesq stability analysis of natural-convection gaseous flow in inclined hot plates", by P. Rajamanickam, W. Coenen and A. L. Sánchez (2017) **109**, 914-917. The dissertation author is the primary investigator in this publication.

# Appendix

Introducing the normal-mode decomposition (5.24) into (5.17)–(5.20) with $\hat{\rho} = -\Theta^{-2}\hat{\theta}$ and $\hat{\mu} = \sigma\Theta^{\sigma-1}\hat{\theta}$ and discarding terms of order $Gr^{-2}$ yields

$$\begin{aligned}
&\left[Gr\,\mathrm{i}k\Theta^{-1} + (y/4)\Theta^{-2}\Theta'\right]\hat{u} + Gr(\mathrm{D}\Theta^{-1})\hat{v} + Gr\,\mathrm{i}l\Theta^{-1}\hat{w} \\
&- \left[\mathrm{D}V + Gr\,\mathrm{i}\,(Uk-\omega) + (2U - yU')/4\right]\Theta^{-2}\hat{\theta} = 0, \qquad (5.34)\\
&[\mathrm{D}(\Theta^{\sigma}\mathrm{D}) - \Theta^{-1}V\mathrm{D} - Gr\,\mathrm{i}\,\Theta^{-1}(Uk-\omega) - \Theta^{-1}(2U - yU')/4 \\
&- \Theta^{\sigma}(2k^2 + l^2)]\hat{u} + \left[\mathrm{i}k(\mathrm{D}\Theta^{\sigma}) - Gr\Theta^{-1}U'\right]\hat{v} - kl\Theta^{\sigma}\hat{w} - Gr\,\mathrm{i}k\hat{p} \\
&+ [\sigma(\mathrm{D}U'\Theta^{\sigma+1}) + U(2U - yU')/4 + VU' + 1]\Theta^{-2}\hat{\theta} = 0, \qquad (5.35)\\
&(\mathrm{i}k\Theta^{\sigma}\mathrm{D})\hat{u} + \left[2\mathrm{D}(\Theta^{\sigma}\mathrm{D}) - \Theta^{-1}(\mathrm{D}V) - Gr\,\mathrm{i}\,\Theta^{-1}(Uk-\omega) - \Theta^{\sigma}(k^2 + l^2)\right]\hat{v} \\
&+ (\mathrm{i}l\,\Theta^{\sigma}\mathrm{D})\hat{w} - Gr\,\mathrm{D}\hat{p} + (\tan\phi\,\Theta^{-2} + \sigma\,\mathrm{i}kU'\Theta^{\sigma-1})\hat{\theta} = 0, \qquad (5.36)\\
&- \Theta^{\sigma}kl\,\hat{u} + \mathrm{i}l(\mathrm{D}\Theta^{\sigma})\hat{v} + [\mathrm{D}(\Theta^{\sigma}\mathrm{D}) - \Theta^{-1}V\mathrm{D} \\
&- Gr\,\mathrm{i}\Theta^{-1}(Uk-\omega) - \Theta^{\sigma}(k^2 + 2l^2)]\hat{w} - Gr\,il\hat{p} = 0, \qquad (5.37)\\
&(Pr\Theta^{-1}\Theta' y/4)\hat{u} - GrPr\Theta^{-1}\Theta'\hat{v} + [\mathrm{D}(\Theta^{\sigma}\mathrm{D} + \sigma\Theta'\Theta^{\sigma-1}) - Pr\Theta^{-1}V\mathrm{D} \\
&- GrPr\,\mathrm{i}\Theta^{-1}(Uk-\omega) - \Theta^{\sigma}(k^2 + l^2) + Pr(V - Uy/4)\Theta^{-2}\Theta']\hat{\theta} = 0, \qquad (5.38)
\end{aligned}$$

to be integrated with boundary conditions

$$\hat{u} = \hat{v} = \hat{w} = \hat{\theta} = 0 \text{ at } y = 0, \quad \text{and} \quad \hat{u} = \hat{v} = \hat{w} = \hat{\theta} = \hat{p} = 0 \text{ as } y \to \infty. \qquad (5.39)$$

As in the main text, the symbol D denotes differentiation with respect to $y$. In the convention adopted a function of $y$ placed after D indicates that multiplication by that function should be performed prior to differentiation.

# Bibliography


[1] E. Schmidt and N. Beckmann. Das temperature and geschwindigkeitsfeld von einer warme-abgebenden senkrechten platte bei naturlicher konvecktion. *Tech. Mech. Thermodynamic*, 1:341–349, 391–406, 1930.

[2] E. M. Sparrow and R. B. Husar. Longitudinal vortices in natural convection flow on inclined plates. *Journal of Fluid Mechanics*, 37(02):251–255, 1969.

[3] S. E. Haaland and E. M. Sparrow. Vortex instability of natural convection flow on inclined surfaces. *International Journal Heat and Mass Transfer*, 16(12):2355–2367, 1973.

[4] S. E. Haaland and E. M. Sparrow. Wave instability of natural convection on inclined surfaces accounting for nonparallelism of the basic flow. *Journal of Heat Transfer*, 95(3):405–407, 1973.

[5] J. R. Lloyd and E. M. Sparrow. On the instability of natural convection flow on inclined plates. *Journal of Fluid Mechanics*, 42(03):465–470, 1970.

[6] H. Shaukatullah and B. Gebhart. An experimental investigation of natural convection flow on an inclined surface. *International Journal of Heat and Mass Transfer*, 21(12):1481–1490, 1978.

[7] K. C. Cheng and Y. W. Kim. Flow visualization studies on vortex instability of natural convection flow over horizontal and slightly inclined constant-temperature plates. *Journal of Heat Transfer*, 110(3):608–615, 1988.

[8] E. J. Zuercher, J. W. Jacobs, and C. F. Chen. Experimental study of the stability of boundary-layer flow along a heated, inclined plate. *Journal of Fluid Mechanics*, 367:1–25, 1998.

[9] P. Jeschke and H. Beer. Longitudinal vortices in a laminar natural convection boundary layer flow on an inclined flat plate and their influence on heat transfer. *Journal of Fluid Mechanics*, 432:313–339, 2001.

[10] M. A. Trautman and A. Glezer. The manipulation of the streamwise vortex instability in a natural convection boundary layer along a heated inclined flat plate. *Journal of Fluid Mechanics*, 470:31–61, 2002.

[11] F. Kimura, K. Kitamura, M. Yamaguchi, and T. Asami. Fluid flow and heat transfer of

natural convection adjacent to upward-facing, inclined, heated plates. *Heat Transfer - Asian Research.*, 32(3):278–291, 2003.

[12] G. J. Hwang and K. C. Cheng. Thermal instability of laminar natural convection flow on inclined isothermal plates. *The Canadian Journal of Chemical Engineering*, 51(6):659–666, 1973.

[13] R. A. Kahawita and R. N. Meroney. The vortex mode of instability in natural convection flow along inclined plates. *International Journal Heat and Mass Transfer*, 17(5):541–548, 1974.

[14] P. A. Iyer and R. E. Kelly. The stability of the laminar free convection flow induced by a heated inclined plate. *International Journal of Heat and Mass Transfer*, 17(4):517–525, 1974.

[15] T. S. Chen and K. L. Tzuoo. Vortex instability of free convection flow over horizontal and inclined surfaces. *Journal of Heat Transfer*, 104(4):637–643, 1982.

[16] K. L. Tzuoo, T. S. Chen, and B. F. Armaly. Wave instability of natural convection flow on inclined surfaces. *Jounral of Heat Transfer*, 107(1):107–111, 1985.

[17] M. H. Lin. Numerical study of formation of longitudinal vortices in natural convection flow over horizontal and inclined surfaces. *International Journal of Heat and Mass Transfer*, 44(9):1759–1766, 2001.

[18] H. C. Tien, T. S. Chen, and B. F. Armaly. Vortex instability of natural convection flow over horizontal and inclined plates with uniform surface heat flux. *Numerical Heat Transfer*, 9(6):697–713, 1986.

[19] C. C. Chen, A. Labhabi, H. C. Chang, and R. E. Kelly. Spanwise pairing of finite-amplitude longitudinal vortex rolls in inclined free-convection boundary layers. *Journal of Fluid Mechanics*, 231:73–111, 1991.

[20] A. Tumin. The spatial stability of natural convection flow on inclined plates. *Journal of Fluids Engineering*, 125(3):428–437, 2003.

[21] S. C. Saha, J. C. Patterson, and C. Lei. Scaling of natural convection of an inclined flat plate: sudden cooling condition. *Journal of Heat Transfer*, 133:041503, 2011.

[22] H.-S. Dou, G. Jiang, and C. Lei. Numerical simulation and stability study of natural convection in an inclined rectangular cavity. *Mathematical Problems in Engineering*, 2013:1–12, 2013.

[23] J. F. Clarke and N. Riley. Natural convection induced in a gas by the presence of a hot porous horizontal surface. *The Quarterly Journal of Mechanics and Applied Mathematics*, 28(4):373–396, 1975.

[24] J. A. D. Ackroyd. Laminar natural convection boundary layers on near-horizontal plates. *Proceedings of the Royal Society of London*, 352(1669):249–274, 1976.

[25] M. J. Gollner, A. L. Sánchez, and F. A. Williams. On the heat transferred to the air surrounding a semi-infinite inclined hot plate. *Journal of Fluid Mechanics*, 732:304–315, 2013.

[26] P. J. Schmid and D. S. Henningson. *Stability and transition in shear flows*, volume 142. Springer Science & Business Media, 2012.

[27] S. E Haaland and E. M. Sparrow. Stability of buoyant boundary layers and plumes, taking account of nonparallelism of the basic flows. *Journal of Heat Transfer*, 95(3):295–301, 1973.

[28] P. Hall. The linear development of görtler vortices in growing boundary layers. *Journal of Fluid Mechanics*, 130:41–58, 1983.

[29] A. Bottaro and P. Luchini. Görtler vortices: Are they amenable to local eigenvalue analysis? *European Journal of Mechanics - B/Fluids*, 18(1):47–65, 1999.